

Electronic Thesis and Dissertation Repository

12-18-2014 12:00 AM

Power Management Strategies for Islanded Microgrids

Hisham Mahmood

The University of Western Ontario

Supervisor

Jin Jiang

The University of Western Ontario

Graduate Program in Electrical and Computer Engineering

A thesis submitted in partial fulfillment of the requirements for the degree in Doctor of Philosophy

© Hisham Mahmood 2014

Follow this and additional works at: <https://ir.lib.uwo.ca/etd>



Part of the [Power and Energy Commons](#)

Recommended Citation

Mahmood, Hisham, "Power Management Strategies for Islanded Microgrids" (2014). *Electronic Thesis and Dissertation Repository*. 2596.

<https://ir.lib.uwo.ca/etd/2596>

This Dissertation/Thesis is brought to you for free and open access by Scholarship@Western. It has been accepted for inclusion in Electronic Thesis and Dissertation Repository by an authorized administrator of Scholarship@Western. For more information, please contact wlsadmin@uwo.ca.

POWER MANAGEMENT STRATEGIES FOR ISLANDED
MICROGRIDS

(Thesis format: Monograph)

by

Hisham Mahmood

Graduate Program in Electrical and Computer Engineering

A thesis submitted in partial fulfillment
of the requirements for the degree of
Doctor of Philosophy

The School of Graduate and Postdoctoral Studies
The University of Western Ontario
London, Ontario, Canada

© Hisham Mahmood 2014

Abstract

The focus of this thesis is on developing power management strategies for islanded microgrids. The main objectives of the developed control strategies and the considered sources that define the scope of this work are classified based on the microgrid hierarchical control structure. This control structure subdivides the microgrid control into a primary and a secondary control layer.

At the Primary Control Layer, the main objective of the proposed strategies is to achieve decentralized power management of renewable energy sources and battery storage in droop controlled microgrids. More specifically, the strategies are developed for Photovoltaic (PV) as an example for one of the common renewable energy sources. Two structural configurations for the PV and the battery storage are considered. In the first configuration, the PV and the battery storage are deployed as a single PV/battery hybrid unit in a droop controlled microgrid. Two decentralized power management strategies are proposed for this configuration. In the second configuration, the PV and the battery storage are deployed independently as separate units in the droop controlled microgrid. In contrast to the common approach of controlling the PV unit as a current source, in the proposed strategies, the PV unit is controlled as a voltage source that follows a multi-segment adaptive power/frequency characteristic curve. The strategies are implemented locally at the units using multi-loop controllers without relying on a central management system and communications, as most of the existing algorithms do. Small-signal models of the proposed control loops are developed to investigate system stability. The proposed strategies are validated experimentally results on a 4 kVA prototype microgrid.

At the Secondary Control Layer, strategies are developed to improve reactive power sharing in islanded microgrids. Two control strategies are proposed to achieve accurate reactive power sharing. In the proposed strategies, communication is utilized to facilitate the tuning of the proposed adaptive controllers in order to compensate for the mismatch in voltage drops across feeders. If the communication channel is disrupted, the controllers will operate with the last tuned parameters, which are shown to still outperform the conventional voltage droop control. In addition, the reactive power sharing accuracy based on the proposed strategy is immune to the time delay in the communication channel. The sensitivity of the tuned controller parameters to changes in the system operating point is also explored. The net control action of the proposed controllers is demonstrated to have a negligible effect on the microgrid bus voltage. The feasibility and effectiveness of the proposed strategies are validated using simulation and experimental results.

Keywords: Islanded microgrid, power management, droop control, PV, battery storage, decentralized control, reactive power sharing.

Co-Authorship Statement

All the work presented in this thesis, including the development of the proposed concepts, the mathematical analysis, the design and modeling of the proposed control strategies, the experimental evaluation, and the writing of the thesis and the corresponding papers, is the original work of the candidate Hisham Mahmood. Mr. Dennis Michaelson has contributed to the experimental evaluation in Chapter 2-4 by writing a program to facilitate collecting the experimental data through an Ethernet network. The collected experimental results are included in the following papers:

- [1] **Hisham Mahmood**, D. Michaelson, J. Jiang, “A power management strategy for PV/battery hybrid systems in islanded microgrids,” *IEEE Journal of Emerging and Selected Topics in Power Electronics*, vol. 2, no. 4, pp. 870–882, Dec. 2014.
- [2] **Hisham Mahmood**, D. Michaelson, J. Jiang, “Decentralized Power Management of a PV/Battery Hybrid Unit in a Droop Controlled Islanded Microgrid,” *IEEE Transactions on Power Electronics*, Submitted Sept. 2014, Preliminary Decision: Recommend publication with minor revisions.
- [3] **Hisham Mahmood**, D. Michaelson, J. Jiang, “Strategies for Independent Deployment and Autonomous Control of PV and Battery Units in Islanded Microgrids,” *IEEE Journal of Emerging and Selected Topics in Power Electronics*, Under review, 2014.

Also, Mr. Michaelson contributed to the experimental evaluation of the strategies proposed in Chapter 5 and 6 by writing the program required to establish the Ethernet network. This experimental evaluation is included in the following papers:

- [1] **Hisham Mahmood**, D. Michaelson, J. Jiang, “Accurate reactive power sharing in an islanded microgrid using adaptive virtual impedances,” *IEEE Transactions on Power Electronics*, vol. 30, no. 3, pp. 1605–1617, Mar. 2015.
- [2] **Hisham Mahmood**, D. Michaelson, J. Jiang, “Reactive power sharing in islanded microgrids using adaptive voltage droop control,” *IEEE Transactions on Smart Grid*, Passed the first review round, 2014

To my parents, my wife and sons, Ali and Yousif.

Acknowledgments

I would like to thank my supervisor Dr. Jin Jiang for his valuable help and continuous support over the course of this research. I sincerely appreciate his trust, encouragement and guidance. Also, I would like thank my fellow PhD candidate Dennis Michaelson for his help in the network programming.

Contents

Abstract	ii
Co-Authorship Statement	iii
Dedication	iv
Acknowledgments	v
List of Figures	x
List of Tables	xvi
List of Appendices	xvii
Nomenclature	xviii
1 Microgrid Control	1
1.1 Introduction	1
1.2 Primary Control	3
1.2.1 Voltage Controlled Source (Voltage Regulation Strategy):	4
1.2.2 Power Controlled Source (PQ Control Strategy):	5
1.3 Secondary Control	5
1.4 Centralized vs. Decentralized Power Management Strategies	6
1.5 General Scope	7
1.6 Power Management Strategies for PV and Battery Storage	7
1.6.1 Literature Review	7
1.6.2 Proposed Strategies and Contributions	9
1.7 Enhanced Reactive Power Sharing in Islanded Microgrids	9
1.7.1 Literature Review	9
1.7.2 Proposed Strategies and Contributions	11
1.8 Thesis Outline	12
2 Control Strategy for PV/Battery Hybrid Units – Part I	13
2.1 Introduction	13
2.2 Problem Statement	14
2.3 System Description and Power Management Structure	15
2.4 Internal Power Management System	16

2.5	VSC Control System	17
2.5.1	Power Sharing Scenario	18
2.5.2	Power Balancing Scenario	20
2.5.3	<i>SOC</i> Upper Limit Control Scenario	20
2.5.4	Battery Charging Priority Scenario	21
2.6	Implementation of the Adaptive Droop	22
2.7	Control Design and Stability Analysis	23
2.7.1	Small-Signal Modeling of the <i>SOC</i> Control Loops	24
2.7.2	Small-Signal Modeling of the PV Curtailment Control Loop	28
2.8	Experimental Evaluation	30
2.8.1	Experimental Setup	30
2.8.2	Experimental Results	30
	Power Sharing Scenario	30
	Power Balancing Scenario	32
	<i>SOC</i> Upper Limit Control Scenario	32
	PV Curtailment Control Scenario	33
	Battery Charging Priority Scenario	35
2.9	Summery and Conclusion	36
3	Control Strategy for PV/Battery Hybrid Units – Part II	38
3.1	Introduction	38
3.2	Problem Statement	39
3.3	VSC Control Strategy	40
3.3.1	Nominal Operating Scenario	43
	1) $P_{pv-mppt} \leq P_L \leq (P_{pv-mppt} + P_{D-max})$	44
	2) $P_L > (P_{pv-mppt} + P_{D-max})$	44
	3) $P_L < P_{pv-mppt}$	45
3.3.2	Battery Charging Scenario	46
	1) $P_{pv-mppt} \geq P_{B-max}$	46
	2) $P_{pv-mppt} < P_{B-max}$	48
3.4	DC-DC Converters Control System	48
3.5	Small-Signal Model of the Proposed Control Loops	50
3.5.1	Real/Reactive Control Loops	51
3.5.2	Charging Control Loop	53
3.6	Experimental Evaluation	56
3.6.1	Experimental Setup	56
3.6.2	Experimental Results	57
	Nominal Scenario	57
	Charging Scenario	59
	Transition between Operating Scenarios	60
	Performance of the Charging Control Loop	61
3.7	Summery and Conclusion	63
4	Strategies for Independent Deployment of PV and Battery Units	64
4.1	Introduction	64

4.2	Problem Statement and Objectives	65
	1) PV Unit	65
	2) Battery Unit	66
4.3	Control Strategy of the PV Unit	66
	1) $P_{pv-mppt} \leq P_L \leq (P_{pv-mppt} + P_{D-max})$	69
	2) $P_{pv-mppt} > P_L$	69
	3) $P_{pv-mppt}$ Variations	70
4.4	Control Strategy of the Battery Unit	70
4.5	Decentralized Coordination of the PV, the Battery, and the Droop Controlled Units	74
4.6	Small-Signal Modeling of the Proposed Control Loops	75
	4.6.1 Power Control Loops	75
	4.6.2 DC-Link Voltage Regulation Loop	77
	4.6.3 PV Curtailment Control Loop	79
4.7	Simulation Studies	80
	4.7.1 Simulated Performance of the PV Control Strategy	80
	4.7.2 Simulated Performance of the Battery Control Strategy	83
4.8	Experimental Evaluation	84
	4.8.1 Experimental Performance of the PV Control Strategy	84
	4.8.2 Experimental Performance of the Battery Control Strategy	85
4.9	Summery and Conclusion	87
5	Enhanced Reactive Power Sharing – Part II	88
5.1	Introduction	88
5.2	Islanded Microgrid Structure and Control	89
	5.2.1 Islanded Microgrid Structure	89
	5.2.2 Reactive Power Sharing Analysis	90
5.3	Proposed Control Strategy	93
	5.3.1 Proposed Controller	93
	5.3.2 Tuned Controller Sensitivity to Operating Points	95
	5.3.3 Information Management Structure	97
5.4	Small-Signal Model of the Virtual Impedance Tuning Loop	98
5.5	Simulation Results	101
	Performance of Conventional Controller	101
	Performance of the Proposed Controller	102
	The Effect of the Communication and Information Update Delays	103
	Controller Performance During a Communication Disruption	104
5.6	Experimental Evaluation	105
	5.6.1 Experimental Setup	105
	5.6.2 Experimental Results	106
	Performance of the Conventional Controller	107
	Performance of the Proposed Controller	107
	Performance during a Communication Failure	108
	Performance in the presence of Delays in Communication	110
5.7	Summery and Conclusion	110

6	Enhanced Reactive Power Sharing – Part II	112
6.1	Introduction	112
6.2	Proposed Control Strategy	112
6.3	Small Signal Stability Analysis	116
6.4	Experimental Evaluation	118
6.4.1	Case 1: Units with the Same Power Rating and Different Feeder Impedances	119
	Conventional vs. Adaptive Droop	119
	Performance during a Communication Interruption	119
	Effect of Communication Time Delay	120
	Proposed Controller Effect on the Voltage of the Microgrid Bus .	120
6.4.2	Case 2: Units with Different Power Ratings and Different Feeder Impedances	121
6.5	Summary and Conclusion	122
7	Summary, Contributions, and Future Work	124
7.1	Summary and Contribution	124
7.2	Future Work	127
	Bibliography	128
A	Control Structures and Parameters	137
A.1	Internal Controllers of the DC-DC Converters	137
A.2	Voltage Control System of the VSC	140
B	Parameters Definitions for Chapter 4	142
B.1	142
B.2	143
	Curriculum Vitae	144

List of Figures

1.1	Simplified microgrid control structure.	3
1.2	Simplified diagram of a voltage regulation strategy for a 3-phase Grid-Forming DG unit (voltage controlled source).	4
1.3	PQ control strategy implemented using current-mode control in dq-frame.	6
2.1	Schematic diagram of the PV/battery hybrid system.	15
2.2	Internal Power Flow Management System.	16
2.3	VSC Control System, which shows the frequency and voltage droop control.	17
2.4	Brief description of the proposed operating scenarios objectives.	18
2.5	Multi-segment adaptive droop characteristics illustrating the power sharing operating scenario.	19
2.6	Adaptive droop slope limits based on the available power.	19
2.7	Adaptive droop actions to regulate the <i>SOC</i> at its limit. Case I: Power sharing scenario – operating points A_1 and A_2 . Case II: <i>SOC</i> upper limit control – operating points B_1 and B_2 . Case III: <i>SOC</i> upper limit control – operating points C_1 and C_2	21
2.8	Adaptive droop control behavior during battery charging priority scenario considering two loading cases	22
2.9	Proposed adaptive droop implementation.	23
2.10	Approximated model of the <i>SOC</i> upper limit control loop.	24
2.11	Block diagram illustrating the <i>SOC</i> calculation based on the coulomb counting principle.	24
2.12	Validation of the approximated model of the <i>SOC</i> upper limit control loop for two different gain sets. (a) <i>SOC</i> transient response. (b) Output power (P_H) transient response.	26
2.13	Linearized model of the <i>SOC</i> upper limit control loop.	26
2.14	Transient response of the linearized model vs. the approximated and the detailed model of the <i>SOC</i> upper limit control loop.	27
2.15	Dominant root trajectories of the <i>SOC</i> control loop.	27
2.16	Approximated model of the PV curtailment control loop.	28
2.17	PV power characteristic (Irradiance= $1000 \text{ W}/m^2$, $T=25 \text{ C}^\circ$) where a straight line is used to approximate the characteristic between the points of $P_{pv}=1000 \text{ W}$ and 800 W	28
2.18	Linearized model of the PV curtailment control loop.	28

2.19	Transient response of the linearized model vs. the detailed switching model of the PV curtailment control loop, for load disturbances of -200 W at t=16 s and +200 W at t=26 s.	29
2.20	Dominant root trajectories of the PV curtailment control loop.	29
2.21	Schematic diagram of the two-unit microgrid prototype.	31
2.22	The experimental apparatus.	31
2.23	Experimental performance of the proposed strategy during the power sharing scenario.	32
2.24	Experimental results showing the power balancing operating scenario. . .	33
2.25	Experimental results showing the performance of the proposed strategy during the <i>SOC</i> upper limit control scenario. (a) Control strategy response to PV power changes (solar irradiance changes). (b) Control strategy response to load changes.	34
2.26	Experimental results showing the performance of the proposed strategy when the <i>SOC</i> exceeds the maximum limits and both the <i>SOC</i> upper limit control loop and the PV curtailment control loops start operating. .	35
2.27	Experimental performance during the battery charging priority scenario. .	36
3.1	Schematic diagram of the PV/battery hybrid system and the microgrid structure.	40
3.2	Power/frequency characteristics of the droop controlled units, and the equivalent characteristic that represents the combined behavior of the units. .	41
3.3	Hybrid unit VSC controller and the proposed <i>P/f</i> characteristics of the hybrid unit. (a) Hybrid unit VSC controller. (b) Equivalent power/frequency characteristics of the hybrid unit.	42
3.4	Equivalent <i>P/f</i> characteristics of the microgrid, along with the increasing load trajectory	42
3.5	<i>P/f</i> characteristics of the microgrid in the Nominal Operating Scenario when the PV power decreases from $P_{pv-mppt-I}$ to $P_{pv-mppt-II}$	44
3.6	<i>P/f</i> operating point trajectory when the load changes from P_{L-I} to P_{L-II} , where $P_{L-II} < P_{pv-mppt}$	45
3.7	<i>SOC/P_{B-ref}</i> characteristic curve of the <i>Priority Controller</i>	47
3.8	<i>P/f</i> characteristic illustrating the <i>Battery Charging Scenario</i> when $P_{pv-mppt} \geq P_{B-max}$, and when the load increases.	47
3.9	<i>P/f</i> characteristic during the Battery Charging Scenario when $P_{pv-mppt} < P_{B-max}$. .	48
3.10	Control system for the DC-DC converters.	49
3.11	PV power characteristics (Irradiance=1000 W/m ² , T=25C ^o) showing the MPP and the PI _B control region.	50
3.12	Root trajectories of the real/reactive control loops when the gain K_{i-p} changes from 0.01 to 0.07 with a step of 0.005 rad/(W·s ²). (a) All the roots trajectories. (b) Zoomed in view of the least sensitive trajectory. . .	53
3.13	Approximated model of the P_B Control Loop. (a) Nonlinear model. (b) Linearized model.	55
3.14	Approximated model of the charging control loop.	55

3.15	Experimental results illustrating the battery voltage excursion beyond $V_{B-limit}$ during unconstrained constant power charging.	56
3.16	Dominant root trajectories of the charging control loop when the gain K_{i-ch} is varied from 2 to 100 with a step of 0.25.	56
3.17	Experimental performance of the proposed strategy during the nominal operating scenario in response to load changes.	57
3.18	Experimental results of the proposed strategy during the nominal operating scenario in response to PV power changes.	58
3.19	Experimental results of the proposed strategy during the charging operating scenario.	60
3.20	Experimental results of the proposed strategy during a transition from the charging scenario to the nominal operating scenario.	61
3.21	Experimental results showing the action of the proposed charging controller.	62
4.1	Structure of the islanded microgrid.	65
4.2	P/f characteristics of the droop controlled units.	67
4.3	Control system of the PV unit. (a) VSC power controller. (b) PV DC-DC converter controller.	67
4.4	Multi-segment P/f characteristics of the PV unit and the microgrid. (a) P/f characteristics of the PV unit. (b) Equivalent P/f characteristics of the microgrid when combining the characteristics of the PV unit and the droop controlled units.	68
4.5	Power characteristic curve of a PV array showing the curtailment operating region.	70
4.6	Shift in the microgrid P/f characteristic due to a change in the PV power from $P_{pv-mppt-A}$ to $P_{pv-mppt-B}$	71
4.7	Multi-segment P/f characteristics of the Battery unit.	72
4.8	P_{ch-ref}/SOC charging curve.	72
4.9	Equivalent P/f characteristics of the battery unit and the droop controlled units, for different values of P_{ch-ref}	72
4.10	Equivalent P/f characteristics of the microgrid showing the increasing load trajectory - Supplying the peak load from the battery.	73
4.11	Control strategy of the battery unit that produces the proposed P/f characteristic curve	74
4.12	P/f characteristics of the PV, the battery, and the droop units combined in a single multi-segment curve for the microgrid (a) when $P_{ch-ref} > 0$ (battery charging); (b) when $P_{ch-ref} = 0$ (battery floating).	75
4.13	Linearized model of the power control loop.	77
4.14	Root trajectories of the power control loops when the gain K_{i-p} is varied from 0.01 to 0.07 with a step of 0.005 rad/(W·s ²). (a) All the root trajectories. (b) Zoomed in view of the encircled root trajectory.	77
4.15	Linearized model of the DC-link voltage regulation loop.	79
4.16	Root trajectories of the DC-link regulation loop when the integral gain K_{idc} is changed from 10 to 100 with a step of 1 W/(V·s), while K_{pdc} is set to 10 W/V.	79

4.17	Approximated model of the PV curtailment control loop.	80
4.18	Linear model of the PV curtailment control loop.	80
4.19	Root trajectories of the PV curtailment control loop when the gain K_{i-c} is changed between 10 and 60 with a step of 0.5/s, and K_{p-c} is set to 20.	80
4.20	Simulated performance of the PV control strategy in response to variations in load demand.	81
4.21	Simulated behavior of the PV control strategy in response to variations in the available PV power.	82
4.22	Simulated performance of the battery unit using the proposed controller.	83
4.23	Experimental performance of the PV unit in response to variations in load demand.	85
4.24	Experimental performance of the PV unit in response to variations in the available PV power.	86
4.25	Experimental performance of the battery unit controller.	86
5.1	Islanded microgrid with communication links to an Energy Management System (EMS).	89
5.2	Simplified model of the microgrid with two inverters.	91
5.3	The detailed network model as seen from <i>DG 1</i>	91
5.4	The proposed adaptive virtual impedance controller.	94
5.5	\tilde{K}_v sensitivity based on the parameters of DG units 1 and 2 from Table 5.1 ($\Delta X = 0.94\Omega$, $\Delta R = 0.5\Omega$). (a) \tilde{K}_v as a function of the load operating point. (b) S_v in the considered operating range.	96
5.6	Sensitivity of \tilde{K}_v for different values of ΔR ($\Delta X = 0.94\Omega$).	97
5.7	Reactive power setpoint enable logic in each local controller.	98
5.8	Linearized model.	99
5.9	Simplified block diagram of the linearized model.	100
5.10	Dominant root trajectory when	100
5.11	Simulated performance of conventional droop control. (a) Real power. (b) Reactive power.	101
5.12	Simulated performance of the proposed controller (activated at $t = 1$ s). (a) Real Power. (b) Reactive Power. (c) Real-time tuning of the virtual impedance variables.	102
5.13	The behavior of the microgrid bus voltage (V_{pcc}) when the controller is enabled at $t = 1$ s.	103
5.14	Simulated feeder currents. (a) Under conventional control (before enabling the controller). (b) Under the proposed control strategy.	103
5.15	Simulated performance of the controller considering the effects time delay mismatches among the communication channels and the information update delay. (a) Real power. (b) Reactive Power.	104
5.16	Simulated performance of the tuned controller in response to a load change after a communication failure. (a) Reactive Power. (b) Phase-a feeder currents.	105
5.17	Simulated system performance during communication restoration.	105
5.18	The experimental apparatus.	106

5.19	Power and current sharing under conventional droop control. (a) Real and reactive power from each inverter for step changes in the load. P_1, P_2 start at 584 W and drop to 568 W; Q_1 starts at 498 var and drops to 298 var; Q_2 starts at 825 var and drops to 522 var. (Vert: 150 VA/div; Horiz: 1 s/div) (b) Phase-a currents from each inverter for two different load operating points. (Vert: 2 A/div; Horiz: 20 ms/div)	107
5.20	Real and reactive power sharing. (Vert: 150 VA/div) (a) As the proposed control loop is enabled. P_1, P_2 are each 584 W. Q_1 and Q_2 are initially 498 var and 825 var, respectively, and each converge to 665 var when the controller is enabled. (b) A step change in the load operating point with the controller enabled. The steady-state reactive power for each inverter steps from 665 var to 445 var and back.	108
5.21	Improvement in current sharing accuracy (phase a). (a) Conventional controller (before enabling the proposed controller). (b) Proposed controller enabled. (Vert: 2 A/div; Horiz : upper 500 ms/div, lower 20 ms/div) . .	108
5.22	Performance of the tuned controller in response to a load change after a communication failure. The lower trace shows the controller enable signal. Q_1, Q_2 are even at 665 var each and continue at this level after communication is lost. When the reactive load is changed Q_1 drops to 439 var and Q_2 drops to 405 var. (Vert: 150 var/div; Horiz: 1 s/div) . .	109
5.23	Phase-a current sharing during a communication failure with a change in reactive power load. (Vert: 2 A/div; Horiz : upper 1 s/div, lower 20 ms/div)	109
5.24	Reactive power from each inverter when communication is lost and restored (upper traces). The lower trace shows the controller enable signal. (Vert: 150 var/div; Horiz: 1 s/div)	109
5.25	Real and reactive power sharing with a time delay mismatch in the communication channels. (a) As the proposed control loop is enabled. (Vert: 150 var/div; Horiz: 500 ms/div) (b) A step change in the load with the controller enabled. (Vert: 150 var/div; Horiz: 1 s/div)	110
6.1	Simplified model of the microgrid with two inverters.	113
6.2	Proposed adaptive droop control for a single unit.	114
6.3	Small-signal model of the droop tuning controller.	117
6.4	Root trajectories when K_i is varied from 0.00001 to 0.00025.	118
6.5	Performance of the proposed controller vs. the conventional voltage droop control - <i>Case 1</i> (Q : 72.4 var/div, P : 181 W/div, Time: 1 s/div). (a) The conventional control. (b) The proposed control strategy.	119
6.6	Performance of the proposed controller during a communication interruption - <i>Case 1</i> (Q : 72.4 var/div, P : 181 W/div, Time: 2 s/div). (a) During a reactive power change. (b) During a real power change.	120
6.7	Performance of the proposed controller with a communication delay - <i>Case 1</i> (Q : 72.4 var/div, P : 181 W/div).	121
6.8	The effect of the proposed controller on the voltage of the microgrid bus (load voltage) (Q : 72.4 var/div, V_{pcc} : 5 V/div, Time: 0.5 s/div).	121

6.9	Performance of the conventional voltage droop control - <i>Case 2</i> (Q : 72.4 var/div, P : 181 W/div, Time: 1 s/div).	122
6.10	Performance of the proposed controller before and after losing communications - <i>Case 2</i> (Q : 72.4 var/div, P : 181 W/div, Time: 1 s/div).	122
A.1	Schematic diagram of the PV and the battery DC-DC converters.	138
A.2	Controllers of the PV and the battery DC-DC converters.	139
A.3	Experimental performance of the DC-DC converters in response to a load disturbance. (a) Step-up load disturbance. (b) Step-down load disturbance.	139
A.4	Simplified diagram of a voltage regulation strategy for a 3-phase Grid-Forming DG unit (voltage controlled source).	140
A.5	Voltage tracking loops of the of the VSC.	141

List of Tables

2.1	System Parameters	25
3.1	System Parameters	53
4.1	System Parameters	78
5.1	System Parameters	97
6.1	System Parameters	118
6.2	Reactive Power Sharing Error for Selected Operating Points	122
A.1	Key Parameters of the DC-DC Converters	138

List of Appendices

Appendix A Control Structures and Parameters of the Power Electronic Converters	137
Appendix B Parameters Definitions for Chapter 4	142

Nomenclature

v_{pv}	PV array voltage
i_{pv}	Output current of the PV array
P_{pvo}	PV power injected into the DC-link
$P_{pv-mppt}$	Available maximum PV power
v_{mppt}	PV voltage reference generated by the MPPT algorithm
v_{pv-ref}	PV voltage reference
v_{dc}	DC-link voltage
v_{dc-ref}	DC-link voltage reference
$v_{dc-limit}$	Maximum limit of the DC-link voltage
C_{dc}	Capacitance of the DC-link
i_B	Battery current
v_B	Battery terminal voltage
P_B	Battery output power
P_{B-max}	Power rating of the battery system
C_{bat}	Capacity of the battery in Ah
P_{Bo}	Battery power measured at the DC-link
P_H	Output power of the PV/battery hybrid unit
P_{pv}	Output power of the PV unit (Chapter 4)
P_{pvi}	PV power injected into the DC-link (Chapter 4)
P_L	Load real power demand
Q_L	Load reactive power demand
P_D	Sum of the droop controlled output powers
P_{D-max}	Sum of the droop controlled output power ratings
N	Total number of the DG units in the microgrid
L_i	Inductance of Unit i feeder (feeder i)
R_i	Resistance of Unit i feeder (feeder i)
X_i	Reactance of Unit i feeder (feeder i)
C_f	Capacitance of the VSC LC filter
L_f	Inductance of the VSC LC filter
f_{ref}	Frequency reference of the VSC controller
Δf_{max}	Maximum frequency deviation limit of the frequency droop control
V_{ref}	Voltage reference of the VSC controller
m	Frequency droop coefficient
n	Voltage droop coefficient
\tilde{K}_v	Adaptive virtual impedance parameter
R_v	Resistive component of the virtual impedance
X_v	Inductive component of the virtual impedance
V^*	Voltage reference of the VSC controller (Chapters 5 and 6)
ω^*	Frequency reference of the VSC controller (Chapters 5 and 6)
ΔV_i	Voltage drop across feeder i
\tilde{n}	Adaptive component of the voltage droop coefficient

Microgrid Control

The concept of microgrids is introduced in this chapter. Microgrid control issues, hierarchical control layers, and power management strategies are discussed briefly. Thereafter, the structure of the thesis is divided based on the defined microgrid control layers. Consequently, the considered control problem at each layer is introduced along with the literature review, followed by the thesis outline.

1.1 Introduction

Distributed generation (DG) has recently received a great deal of attention as a potential solution to meet the increased demand for electricity, to reduce stress on the existing transmission system, and to incorporate more renewable and alternative energy sources. Subsequently, the microgrid concept has emerged as a promising approach to coordinate different types of distributed energy resources effectively by using local power management systems. A microgrid is defined by Microgrid Exchange Group (MEG) of the U.S. Department of Energy (DOE) [1] as “a group of interconnected loads and distributed energy resources within clearly defined electrical boundaries that acts as a single controllable entity with respect to the grid. A microgrid can connect and disconnect from the grid to enable it to operate in both grid-connected or islanded mode.”

Distributed energy resources (DER) considered in the literature are typically non conventional and renewable resources, such as fuel cells, biomass, geothermal, photovoltaic (PV), wind, and microturbines [2–4]. This is mainly due to the modular nature of these resources, and the negligible or low greenhouse gas emissions. In addition to the distributed generation (DG) resources, fast acting energy storage, such as batteries, flywheels, or supercapacitors, is considered crucial to the operating of the microgrid as it facilitates voltage and frequency regulation during the islanded mode. The output voltage in most of these resources is either in DC or in unregulated AC form. Due to the unregulated output voltage, and the inherent intermittent nature of the renewable energy sources, power electronic converters are employed to control the generated power, and interface these energy sources [5, 6].

In the grid-connected mode, the operating voltage and frequency regulation is pro-

vided by the grid [7]. The utility grid ensures a relatively stiff frequency regulation due to the rotating mass inertia of the large synchronous generators in the power system [8]. Moreover, the amount of power exchanged between the microgrid and the grid is determined by the difference between the generation and the load demand in the microgrid. In other words, the grid is responsible for maintaining the power balance in the microgrid. Therefore, the absence of the grid in the islanded mode makes microgrid control more challenging. In islanded mode, any microgrid control strategy must be able to perform the following main tasks:

1. **Frequency and Voltage Regulation:** Due to the rotating mass inertia of large generators in conventional power systems, the grid offers a stiff and robust regulation of the operating frequency in grid-connected mode. The grid achieves this by supplying/absorbing the transient power difference during generation/load disturbances, with a negligible decrease/increase in the frequency during transients. On the other hand, the Automatic Generation Control (AGC) is responsible for maintaining the power balance in the system by adjusting the generated power to match the load demand at steady state. Once the microgrid is islanded the frequency and voltage regulation provided by the grid will no longer be available. Therefore, at least one DG unit must be responsible for the task of regulating the microgrid voltage and frequency.

However, the power electronic converters used to interface the DER units have negligible inertia; and most microsources, e.g. fuel cells and microturbines, have a sluggish response and cannot provide stiff frequency regulation. In this case, fast acting energy storage devices, such as batteries, supercapacitors or flywheels, are used to duplicate the effect of the rotating mass inertia in the conventional grid [9,10]. These energy storage device can be connected to the microgrid bus, through power electronic converters, as a separate distributed storage (DS) unit, or can be connected to the DC link of the DG units. The fast response of the energy storage enables the DG unit to react to any transient imbalance in the generation/load demand, while regulating the operating frequency and voltage [9]. Battery storage is commonly employed as the energy storage in microgrid applications due to its high energy density in comparison to the supercapacitors and flywheels. Therefore, battery storage is chosen as the energy storage element in this thesis.

2. **Power Balance¹:** Ideally, DG units must be controlled to cooperatively match the load demand (including power losses) at steady state. Accordingly, the battery storage in the microgrid neither supplies nor absorbs power at steady state to avoid depleting or over-charging the battery. Nevertheless, the battery storage can be controlled to supply power during peak load periods, when the load demand increases beyond the total generation, or to absorb the surplus power from the renewable energy resources, to maintain the power balance in the islanded microgrid.

¹Power balance refers here to the balance between the total generated power and the load demand (including power losses) in the microgrid at steady state, while the systems is operating within the specified voltage and frequency limits.

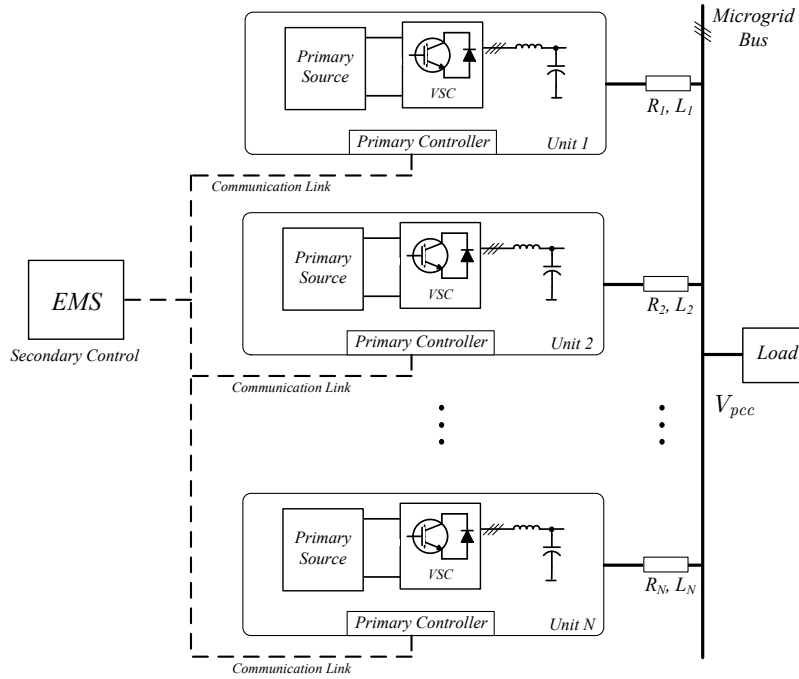


Figure 1.1: Simplified microgrid control structure.

The local control strategy at each unit must be designed based on the characteristics of the primary energy source, and the control role assigned to the unit in the microgrid to achieve the aforementioned global control tasks. Moreover, communications and central energy management system (EMS) might be used, as shown in Fig. 1.1 to coordinate the operation of the DG units and/or enhance the performance of the local controllers. Accordingly, the microgrid control structure can be divided into two hierarchical layers, primary and secondary. Note that, primary and secondary control layers have been defined in [11, 12] for a special case of droop controlled microgrids. A more general definition that applies to microgrid control is presented in this work. Based on the control objectives of each layer, power management strategies of islanded microgrids will be categorized into centralized and decentralized (autonomous) control strategies. The control layers and power management strategies of islanded microgrids are discussed in the following sections.

1.2 Primary Control

The primary control refers, in this thesis, to the control strategies that are implemented locally at each DG unit, and are responsible for regulating the output voltage or power at the desired references. These references are either internal, i.e. generated internally based on local measurements, or external references received from a higher control layer [9]. The output of the DG unit refers to the output of the interfacing DC/AC Voltage Sourced Converter (VSC). Based on the control strategy chosen for the VSC, the DG unit can

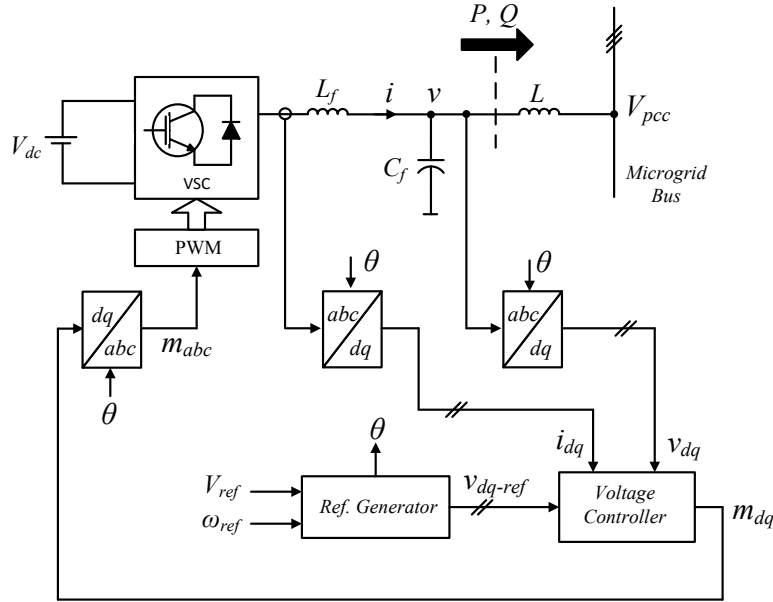


Figure 1.2: Simplified diagram of a voltage regulation strategy for a 3-phase Grid-Forming DG unit (voltage controlled source).

operate either as a voltage controlled source or as a power controlled source, as briefly discussed below.

1.2.1 Voltage Controlled Source (Voltage Regulation Strategy):

In this DG unit, the VSC is controlled to regulate the output voltage magnitude and frequency, i.e. the DG unit acts as a voltage controlled source. This unit is responsible for forming the microgrid bus voltage, therefore it is called the Grid-Forming unit [6, 7] or the Master unit [8].

A typical voltage regulation strategy of a three-phase VSC, in the synchronous frame (dq-frame) [6, 13–16], is shown in Fig. 1.2. When a single DG unit is responsible for regulating voltage/frequency, the microgrid is called a Single-Master microgrid [8]. In this case, the voltage reference (V_{ref}) and the frequency reference (ω_{ref}) are set to the nominal voltage (V_o) and nominal frequency (ω_o), respectively.

On the other hand, when two or more units share the responsibility of forming the microgrid, the microgrid is called a Multi-Master microgrid. In this case, frequency and voltage droop control techniques that mimic the steady state behavior of synchronous machine based generators in conventional power systems are used [8, 17–24]. In other words, the references at each Grid-Forming unit are calculated using the droop control equations as follows

$$\omega_{ref} = \omega_o - mP_m \quad (1.1)$$

$$V_{ref} = V_o - nQ_m \quad (1.2)$$

where P_m and Q_m are the real and reactive powers measured at the output of the DG unit, respectively, and are filtered to extract the fundamental power components. The constant m is the frequency droop coefficient, whereas n is the voltage droop coefficient.

Two types of primary sources can be controlled using the considered strategy. First, fast acting energy storage devices as discussed in Section 1.1. Second, a hybrid combination of energy storage and a dispatchable (controllable) energy source such as a fuel cell. The energy storage is crucial in this case to compensate for the slow response of the energy sources. The energy storage device is commonly connected to the DC-link of the hybrid unit to supply/absorb power during transients, while the energy source is controlled to ramp up/down the output power to match the supplied power at steady state [25–35].

1.2.2 Power Controlled Source (PQ Control Strategy):

The ultimate objective of the primary controller in this case is to regulate the output active/reactive power of the VSC at certain references. This strategy assumes the microgrid is formed by another unit or units, i.e. the voltage and frequency at the Point of Common Coupling (PCC) are regulated. In the case of dispatchable (controllable) energy sources, such as fuel cells and microturbines, the power set points are provided in general by a supervisory control. On the other hand, in the non-dispatchable DER units, such as renewable energy based DER, the power set point is implicitly generated based on the amount of power available at the DC-link of the VSC.

The PQ control strategy is commonly implemented using current-mode control [6], as shown in Fig. 1.3, due to the advantages of its inherent fault/overload current protection and superior dynamic performance [13]. Nevertheless, voltage-mode control is used as well in grid connected applications [13, 36].

In conclusion, the above two strategies are the main control approaches to form an islanded microgrid and manage the power flow. The choice of a suitable control strategy is mainly based on the characteristics of the primary source and the desired role of that source in the islanded microgrid.

1.3 Secondary Control

The secondary control is defined, in this thesis, as the control layer that utilizes communications to achieve global performance objectives in the microgrid, such as power management, voltage restoration, frequency restoration, operating cost reduction, or improving reactive power sharing [9, 11, 12, 37–43]. Note that, the secondary control layer still utilizes the local primary controllers as actuators to achieve the desired global objectives. The bandwidth of the secondary control strategies is limited by the bandwidth of the employed communication technology. Therefore, the secondary control layer is

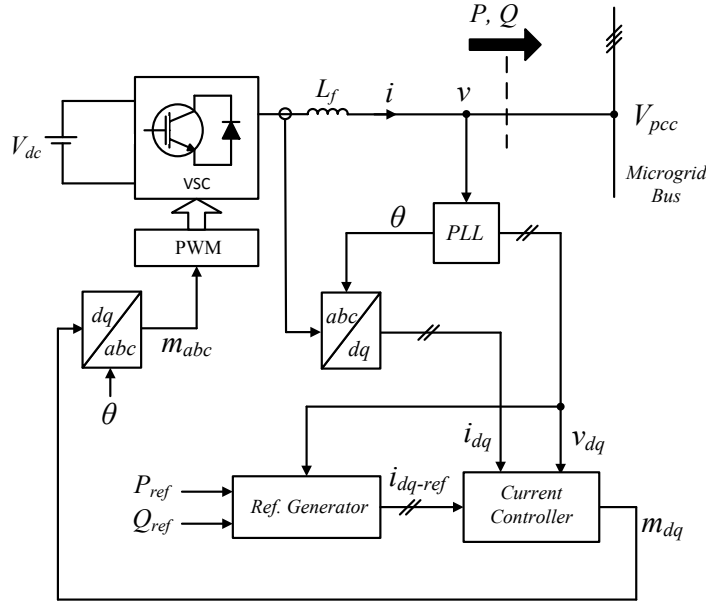


Figure 1.3: PQ control strategy implemented using current-mode control in dq-frame.

in general slower than the primary layer, which is characterized by the fast voltage and current control loops of the switching power converters.

1.4 Centralized vs. Decentralized Power Management Strategies

As mentioned previously, based on the objectives of each control layer, the power management strategies of an islanded microgrid can be categorized into centralized (supervisory) and decentralized (autonomous) strategies. In centralized power management strategies, the secondary control layer is directly responsible for coordinating the DG units to maintain the power balance in the islanded microgrid at steady state [44–46]. Accordingly, a supervisory power management algorithm and communications are crucial to coordinate the operation of the DG units. The power management algorithm is usually implemented in a control unit called a microgrid central controller (MGCC) or an energy management system (EMS) [9]. The primary controllers receive external references, or information to calculate the references, from the secondary layer to cooperatively maintain the power balance in the system at steady state. Note that, even though the secondary control layer is directly responsible for coordinating the DG units at steady state, at least a single Master unit must be responsible for regulating the voltage and frequency to provide the necessary inertia during load/generation transients.

In decentralized power management strategies, the primary controllers are responsible for maintaining the power balance in the islanded microgrid autonomously, without requiring external references, external communications, or a central management algo-

rithm. Nevertheless, the secondary layer can still be used to enhance the performance of the microgrid by providing voltage/frequency restoration, improving the reactive power sharing accuracy, or reducing operating cost [11, 12, 39–41]. Conventional droop control is the typical decentralized power management strategy used in the literature [6, 9, 11, 12].

1.5 General Scope

The focus in this thesis is on developing power management strategies for islanded microgrids. The main objectives of the developed control strategies and the considered distributed sources that broadly define the scope of this work are introduced based on the hierarchical control layer, as follows:

1. **Primary Control Layer:** The main objective of the strategies developed in this layer is to achieve decentralized power management of intermittent energy sources and battery storage in droop controlled microgrids. More specifically, the strategies are developed for Photovoltaic (PV) as an example of one of the common renewable energy sources. The problem of PV and battery power management in islanded microgrids, along with the literature review and the features of the proposed strategies, is introduced in Section 1.6.
2. **Secondary Control Layer:** At this layer, strategies are developed in this work to improve the accuracy of reactive power sharing in islanded microgrids. The problem of reactive power sharing in an islanded microgrid is introduced in Section 1.7, along with the literature review, and the features of the proposed strategies.

1.6 Power Management Strategies for PV Systems and Battery Storage in Islanded Microgrids

1.6.1 Literature Review

From a control point of view, photovoltaic (PV) generation units can be classified into standalone and grid connected configurations. Due to the intermittent nature of PV power, battery storage is employed as a critical element in PV standalone applications, to maintain the power balance in the system and to enable regulation of the load voltage [47–50]. Islanded microgrids share the same issue with standalone systems, since the battery storage is needed to maintain the generation/load balance, and to regulate the microgrid voltage and frequency. In both cases, the power management strategy should consider the state-of-charge (*SOC*) limits and the power rating of the battery. However, the problem of maintaining the power balance in the presence of PV is more challenging in islanded microgrids for several reasons. First, the storage unit can be installed as a separate unit in a different location in the microgrid, with no direct control interconnection with the PV unit. Second, the PV units are commonly controlled as current controlled sources to inject all the available power into the microgrid (the PQ control strategy [8]). This strategy was originally developed for grid connected applications, where the generation/load balance

is maintained through the grid. In other words, applying this strategy directly in an islanded microgrid could result in power imbalance when the available PV power is higher than the load demand, and the battery is fully charged. Finally, in addition to the PV and battery units, the microgrid can accommodate other units that use different control strategies, which must be considered when designing the power management strategy of the microgrid.

Therefore, the operation of the PV system and the battery storage must be coordinated with the other units in the islanded microgrid to maintain the power balance, while respecting the battery storage limits. This coordination problem has been dealt with in the literature using centralized control strategies that employ communications among units [51–58].

The EMS in [51–58] requires access to the power measurements at each distributed generation (DG) unit and load node, through communication, in order to be able to maintain the power balance in the microgrid. Accordingly, power measurement and communication modules must be installed at each generation and load node, which adds to the system complexity, and increases the potential failure modes. In all of the aforementioned strategies, communication is a critical part of the strategy. If the communication with any generation or load node is lost, the EMS may generate an undesirable control command. Therefore, dependence on communication for power management may reduce the reliability of the control strategy [18, 20].

Moreover, the power management strategy proposed in [53] is designed so that both the fuel cell and the battery use the droop control approach to share the peak load, when the power available from the PV unit and the microturbine is inadequate to match the load. This might deplete the battery storage prematurely. Instead, it is recommended that the battery only be used during transients [56], and to supply the deficit power only after the load increases beyond the total capacity of the other generating units. The EMS in [56] employs communication to ensure that the battery neither supplies nor absorbs any power at steady state. This is achieved through coordinating the power dispatched by the controllable (dispatchable) units in the microgrid.

To avoid utilizing communications, a control strategy is proposed in [59] for a microgrid composed of a PV unit and a battery storage unit. When the battery voltage exceeds its pre-set limit during charging, the battery inverter reduces the line frequency below the anti-islanding frequency limit of the PV inverter. Accordingly, the PV unit responds by disconnecting from the microgrid. Similarly in [60], a single battery unit is used to regulate the microgrid frequency. This unit starts increasing the microgrid frequency when the battery approaches its *SOC* limit. Consequently, the PV unit employs the increasing microgrid frequency as a signal to curtail the PV power in order to avoid overcharging the battery. The applicability of the techniques in [59] and [60] is limited to microgrids where only one DG unit (battery storage) is in charge of regulating the voltage and the frequency. Hence, the technique cannot be applied directly to microgrids with droop controlled units sharing the task of regulating the operating frequency.

The PV system in [61–64] is combined with battery storage and other energy sources as a single hybrid unit in the microgrid. This approach is more effective since the PV controller has access to the battery *SOC* without any external communications. However, the strategy proposed in [64] requires a central controller to coordinate the operation of

the hybrid unit with a diesel generator, in order to maintain the power balance in the islanded microgrid. On the other hand, the microgrids considered in [61–63] are composed of one hybrid source and loads, which makes the system more like a standalone power supply, rather than an islanded microgrid, from a control point of view. Therefore, these control strategies cannot be applied directly to an islanded microgrid containing multiple units, such as droop controlled units.

On the other hand, the droop control technique is widely adopted in the literature of islanded microgrids due to its inherent decentralized control nature [8, 18–22, 41]. However, despite the popularity of the droop control, decentralized control strategies for coordinating PV and battery units in droop controlled microgrids are not thoroughly explored in the literature. Avoiding reliance on communications makes designing an effective coordination strategy a challenging task, since there is neither a central EMS nor a direct control interconnection between units.

1.6.2 Proposed Strategies and Contributions

In this work, decentralized power management strategies are developed for PV and battery storage in droop controlled microgrids. Two structural configurations are considered for the PV system and the battery storage. In the first configuration, the PV and the battery storage are deployed as a single PV/battery hybrid unit in a droop controlled microgrid. Two decentralized power management strategies are proposed for this configuration. In the second configuration, the PV and the battery storage are deployed as separate units in the droop controlled microgrid.

In contrast to the common approach of controlling the PV unit as a current source, in the proposed strategies, the PV unit is controlled as a voltage source that follows a multi-segment adaptive power/frequency characteristic curve. The strategies are implemented locally at the units using multi-loop controllers without relying on a central management system and communications, as most of the existing algorithms do. It is demonstrated experimentally that the proposed power/frequency characteristics can adapt autonomously to the microgrid operating conditions so that the hybrid unit may supply the maximum PV power, match the load, and/or charge the battery, while maintaining the power balance in the microgrid and respecting the battery SOC limits. Small-signal models of the proposed control loops are developed to investigate system stability. The performance of the proposed strategies is validated using experimental results from a 4 KVA prototype microgrid. The developed control strategies are discussed in depth in Chapters 2-4.

1.7 Enhanced Reactive Power Sharing in Islanded Microgrids

1.7.1 Literature Review

When islanded, distributed generation (DG) units must be able to cooperatively regulate the voltage and frequency, and maintain the generation/load power balance within the

microgrid. Accordingly, droop control concepts have been widely adopted in the literature [8, 18–22, 41] to provide decentralized power sharing control without relying on communications — this enables “plug-and-play” interfacing [18] and improves the reliability of the system. Communication can, however, be used in addition to the droop control method to enhance the system performance without reducing reliability [9, 11, 12, 37–42].

Although the frequency droop technique can achieve accurate real power sharing, the voltage droop technique typically results in poor reactive power sharing due to the mismatch in the impedances of the DG unit feeders and, also, due to the different ratings of the DG units [65]. Consequently, the problem of reactive power sharing in islanded microgrids has received considerable attention in the literature and many control techniques have been developed to address this issue [66–79].

A comprehensive treatment of the virtual impedance concept to mitigate errors in reactive power sharing is presented in [66–68]. The focus has been on the mismatch in the output impedances of the closed-loop controlled inverters that are used to interface the DG units. With proper design of the voltage controller, the closed-loop output impedances must be negligible at steady state around the nominal operating frequency. Therefore, the virtual impedance is dominant, which results in accurate reactive power sharing. However, the analysis in [66–68] did not consider the mismatch in the physical impedance of the feeders, including transformers, cables, and the interface inductors associated with each unit.

A unique approach is proposed in [69] to achieve accurate reactive power sharing. The proposed strategy requires injection of a small AC voltage signal in the system. Overlaying such an AC voltage signal may reduce the quality of the output voltage and line current [70, 74]. Also, extracting and processing this signal may result in a complicated implementation, particularly in a noisy environment.

A control strategy employing an inductive virtual impedance is developed in [70] to ensure accurate reactive power sharing. The proposed analysis and design is based on the assumption that the feeder impedance is small and dominated by the virtual impedance, which is a known parameter. Moreover, the feeder physical impedance is estimated to improve the accuracy, and to include the effect of the impedance resistive component. The estimation technique requires the system to operate in grid connected mode first, before islanding. The technique is validated for a system with different virtual impedances, but with identical feeder physical impedances. On the other hand, the analysis and the control strategy introduced in [71] requires that the feeder impedances are resistive. The analysis and the control strategy results in accurate power sharing if this condition is satisfied. In practice, however, the feeders may have both non-negligible inductive and resistive components [66].

Control strategies are proposed in [72, 73] to achieve accurate power sharing among inverters in an islanded microgrid. When the inverters are in close proximity an instantaneous control interconnection becomes feasible and can be used as an essential component to achieve accurate sharing. In practice, the DG units might be located in different geographic locations making this approach ineffective.

An interesting control strategy is proposed in [74]. The control strategy is composed of two stages: an initial conventional droop based control stage and a synchronized compensation stage. During the synchronized compensation stage, the frequency droop

is used to control the reactive power sharing. Since this action will also disturb the real power sharing, an integral control term is added to the voltage droop to maintain real power sharing accuracy. However, load changes during the compensation period or between compensation periods may result in poor power sharing.

Communication is used in [75] to facilitate the estimation of the feeder impedances which are then used to set the virtual impedances to ensure accurate reactive power sharing. The feeder impedance is estimated at the local DG controller by utilizing the point of common coupling (PCC) voltage harmonic data transferred via a communication link. This is based on the assumption that the phase angle difference between the voltages at the PCC and at the inverter output is negligible. This assumption may not hold for long feeders or for higher power levels. The same technique is used in [76] under the same assumption.

Communication links are also used in [77] to enhance the performance of conventional droop control. The proposed technique can reduce the sharing error but cannot eliminate it completely. For example, it reduces the maximum sharing error from 5.02% to 3.05%. Also, the performance of the technique is sensitive to delays in communication; e.g. a delay of 16 ms degrades the sharing accuracy significantly. A new droop control is proposed in [78] to reduce the power sharing error. As in [77], the sharing error can be reduced but not completely eliminated and the improvement in performance is not significant if local loads are connected at the output of each unit.

A distributed secondary control technique is proposed in [79–81] to restore the frequency and the voltage, and also to ensure accurate reactive power sharing. In this technique, the controller is implemented in each DG unit instead of implementing it in the microgrid central energy management unit. Communication data drop-outs / packet losses and their effect frequency/voltage restoration are briefly discussed in these papers. However, the same effect on the reactive power sharing is not shown, and the scenario of a complete communication failure is not investigated.

1.7.2 Proposed Strategies and Contributions

In this thesis, two control strategies are proposed to achieve accurate reactive power sharing. In the proposed strategies, communication is utilized to facilitate the tuning of the proposed adaptive controllers in order to compensate for the mismatch in voltage drops across feeders. The contributions of these techniques are summarized below.

- If the communication channel is disrupted, the controllers will operate with the last tuned parameters, which are shown to still outperform the conventional voltage droop control.
- The reactive power sharing accuracy based on the proposed strategy is immune to the time delay in the communication channel.
- The net control action of the proposed controllers is demonstrated to have a negligible effect on the microgrid bus voltage.
- The control strategy is straightforward to implement, and does not require knowledge of the feeder parameters. Therefore, no estimation algorithm is required.

The sensitivity of the tuned controller parameters to changes in the system operating point is also explored. The feasibility and effectiveness of the proposed strategies are validated using simulation and experimental studies. These strategies and contributions are explained in depth in Chapter 5 and 6.

1.8 Thesis Outline

This thesis is structured as follows:

Chapter 2: In this chapter, a power management strategy for PV/battery hybrid systems in islanded microgrids is proposed. The system structure, problem statement, and the proposed strategy are introduced in this chapter. Small-signal models of the proposed control loops are developed to investigate system stability. The system performance is validated using experimental results from a prototype microgrid.

Chapter 3: An alternative control strategy is proposed, in this chapter, to achieve decentralized power management of a PV/Battery hybrid unit in a droop controlled microgrid. This strategy provides more operational features, and achieves superior performance in comparison to the strategy developed in Chapter 2. Small-signal stability of the proposed control loops is investigated and the system performance is experimentally validated on a prototype microgrid.

Chapter 4: In this chapter, decentralized control strategies are proposed for the PV system and the battery storage when they are deployed as separate units in the droop controlled microgrid. Small signal models of the proposed control loops are presented, and the performance of the proposed strategy is validated using simulation results, and also using experimental results from a prototype microgrid.

Chapter 5: The problem of reactive power sharing is introduced in this chapter. The considered system structure, and the problem mathematical analysis are presented in detail. A secondary control strategy is proposed to enhance the accuracy of reactive power sharing using adaptive virtual impedances. The feasibility and effectiveness of the proposed strategy are validated using simulation and experimental results from a prototype microgrid.

Chapter 6: An alternative technique is proposed in this chapter to improve reactive power sharing using adaptive voltage droop control. A small-signal model of the adaptive voltage droop controller is presented, and the strategy is validated using experimental results from a prototype microgrid.

Chapter 7: This chapter presents the thesis summary, the concluding remarks, and the potential future work.

Decentralized Control Strategy for PV/Battery Hybrid Unit in Islanded Microgrids – Part I: Multi-Segment Adaptive Droop Approach

2.1 Introduction

A power management strategy for PV/battery hybrid systems in islanded microgrids is proposed in this chapter. The control strategy enables the PV/battery unit to operate as a voltage controlled source that employs an adaptive droop control to share the load with other sources while charging the battery. Also, the PV/battery unit can track and supply the maximum PV power to the microgrid as long as there is sufficient load. Otherwise, the hybrid unit will autonomously match the varying load demand while storing the excess energy in the battery. The control strategy is designed to adjust the PV operating point to match the load autonomously whenever the available PV power is higher than the load and the battery is fully charged. Moreover, the battery can provide the operational functions that a separate storage unit may provide in an islanded microgrid, such as regulating the frequency, and supplying deficit power in the microgrid. This is achieved by utilizing multi-loop control and multi-segment adaptive droop control without relying on any central management algorithm, communications, or switching logic. Small-signal models of the proposed control loops are developed to investigate system stability. The system performance is validated using experimental results from a 4 kVA prototype microgrid.

The objectives of the proposed control strategy and the problem statement are discussed in Section 2.2. In Section 2.3, the description of the islanded microgrid and the PV/battery hybrid unit is briefly presented along with the structure of the power management strategy. The internal power management strategy, which is responsible for managing the power flow among the PV array, the battery, and the DC-link, is discussed in Section 2.4. The concept of the proposed adaptive droop control and its behavior dur-

ing different operating scenarios is introduced in Section 2.5. The implementation of the controller is presented in Section 2.6. Small-signal models of the proposed control loops are developed and stability is analyzed in Section 2.7. The experimental results that validate the proposed control strategy are presented in Section 2.8, followed by concluding remarks in Section 2.9.

2.2 Problem Statement

In contrast to PV control strategies in the literature where the PV units are controlled as current sources (PQ control), the proposed control strategy enables the PV/battery unit to operate as a voltage source that employs an adaptive droop control. Accordingly, the proposed strategy is designed to provide the following functional features:

1. The hybrid unit can share the load with other droop controlled units while charging the battery. The amount of the shared power is determined by the maximum PV power extracted at the moment, the battery *SOC*, and the microgrid load demand.
2. The hybrid system can track and supply the maximum PV power to the microgrid as long as there is sufficient load. Otherwise, the hybrid unit will autonomously match the available load while storing the excess energy in the battery as in standalone strategies.
3. The control strategy is designed to cease MPPT operation, and curtail the PV power to follow the changing load, whenever the available PV power is greater than the load demand and the battery is fully charged.
4. The battery can provide the operational functions that a separate storage unit may provide in an islanded microgrid, such as regulating voltage and frequency, enabling black start capability, and supplying the deficit power in the microgrid.

Achieving all the above features autonomously through utilizing the proposed multi-segment adaptive droop control and a multi-loop control strategy, without relying on communications and/or a central management algorithm to switch among operation modes, represents the main objective of the proposed strategy.

The key idea of the proposed strategy is to employ the droop control technique. However, due to the intermittent nature of the PV, a fixed droop slope will result in improper power sharing. For example, if the droop slope is set based on the capacity of the PV array, or based on the PV array capacity plus the battery power rating, the hybrid unit will share power based on droop characteristics that do not reflect the actual PV power available at a given time. In this case, the battery will also be supplying power most of the time, even when the other units have not yet reached their full power ratings. This could deplete the battery storage prematurely. This problem is solved by using the proposed multi-segment adaptive droop control.

Since the main focus of the proposed strategy is on the management of the real power flow as in [51–55], reactive power sharing is managed in this work using conventional voltage droop control. Another choice would be to regulate the output reactive power at a certain reference, which can be predefined or received from a higher control layer.

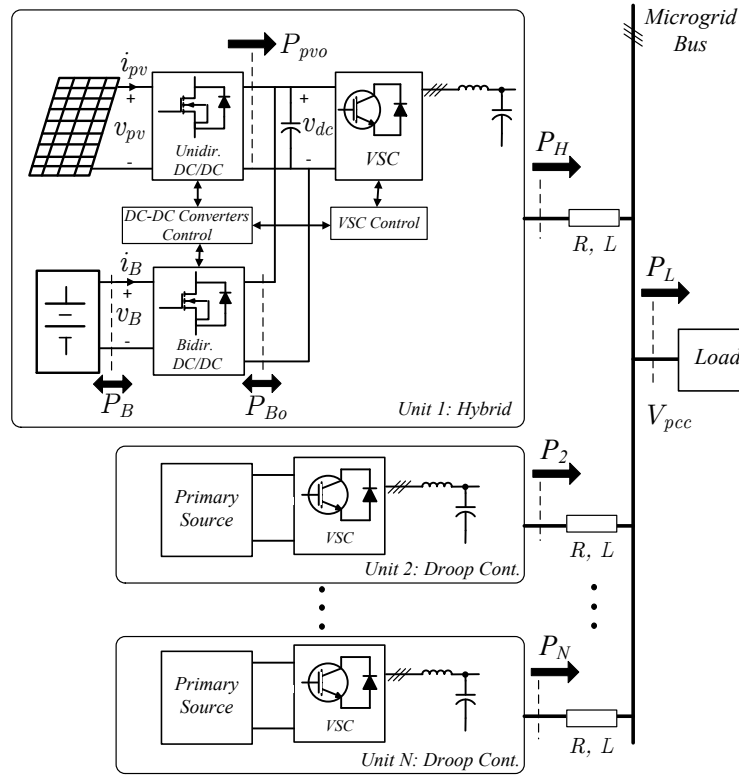


Figure 2.1: Schematic diagram of the PV/battery hybrid system.

2.3 System Description and Power Management Structure

A simplified schematic diagram of a two-unit islanded microgrid is shown in Fig. 2.1. Unit 1 is the PV/battery hybrid unit under consideration, whereas Unit 2 to Unit N are the droop controlled units. The PV array is connected to the DC-link through a unidirectional boost converter. P_{pvo} refers to the PV power injected into the DC-link. P_B and P_{Bo} represent the battery powers supplied/absorbed at the battery terminals and at the DC-link, respectively. The battery is interfaced with the DC-link using a bidirectional converter to ensure fully controlled charging and discharging of the battery. Also, connecting the battery through a DC-DC converter provides flexibility in choosing the DC-link voltage level, and the battery voltage and configuration [25]. In each unit, a three-phase voltage sourced converter (VSC) is used to interface the DC-link to the microgrid through an LC filter, an interface inductor and a transformer.

The power management strategy can be divided into two parts. The first is the Internal Power Flow Management System. This part manages the power flow among the PV array, the battery, and the DC-link in order to maintain the power balance within the hybrid system. This is done by controlling the DC-DC converters and the PV array voltage reference. The operation of this sub-system is discussed in Section 2.4.

The second part is the VSC Control System which is responsible for managing the

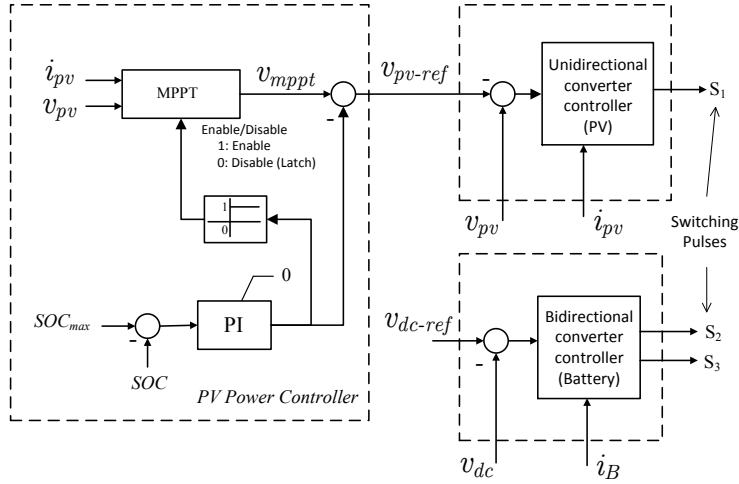


Figure 2.2: Internal Power Flow Management System.

power flow between the hybrid system and the microgrid. It also indirectly manages the power flow between the PV and the battery to maintain the power balance in the hybrid system.

2.4 Internal Power Management System

As can be seen from Fig. 2.2, the voltage at the DC-link is regulated by the battery bidirectional boost converter while the PV boost converter is controlled to regulate the voltage at the PV array terminal. The PV array voltage reference v_{pv-ref} is generated by the PV power controller based on the battery SOC , the PV maximum power, and the load power [50]. Based on these variables, the power flow within the system can be categorized into two operating scenarios: the MPPT scenario, and the PV curtailment scenario. During the MPPT scenario, the voltage v_{pv-ref} is generated by the MPPT algorithm, which assumes that the SOC of the battery is less than the maximum limit SOC_{max} .

When the SOC increases beyond the specified SOC_{max} , the PV curtailment control loop (the PI loop in Fig. 2.2) starts to control the PV power by moving the PV operating point away from the maximum power point (MPP) towards the voltage source operating region of the PV characteristic curve. Therefore, this loop will keep reducing the power extracted from the PV array until the battery current i_B drops to zero and the SOC settles at SOC_{max} . Under this condition, the PI output will be used to disable the MPPT algorithm and force it to stay at the current v_{mpppt} ; otherwise it will keep searching for the maximum power causing v_{mpppt} to drift away from the MPP region.

In the PV curtailment scenario, the PI controller continuously adjusts the PV operating point to follow the load as long as the power available from the PV array can match the load demand. If the load demand becomes larger than the PV power, the battery will supply the deficit power and the PV curtailment control loop becomes idle again.

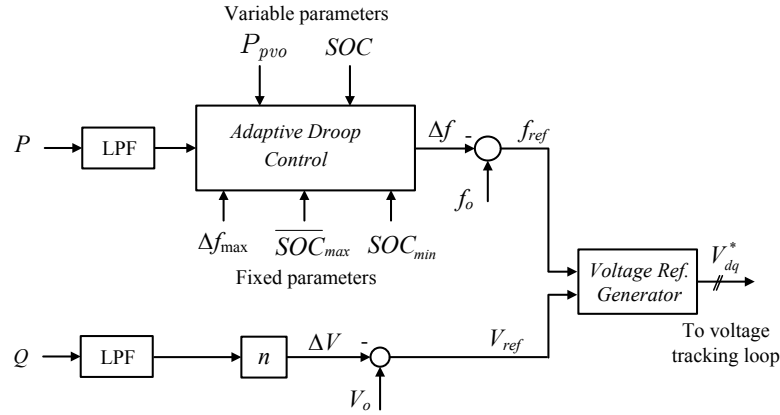


Figure 2.3: VSC Control System, which shows the frequency and voltage droop control.

2.5 VSC Control System

The VSC is controlled as a voltage source, where the frequency and voltage references for the voltage tracking loop are generated as shown in Fig. 2.3. The adaptive droop control uses the real power P to generate the deviation in the frequency reference Δf . The LPF blocks are first order low-pass filters used to remove the effect of any harmonics in the output powers on the voltage and frequency references. The frequency droop characteristic is determined in real time based on two variables, P_{pvo} and SOC , and three fixed parameters: the frequency droop limit (Δf_{max}), and the predefined upper and lower SOC limits of the battery. The voltage magnitude reference is generated using the conventional voltage/reactive power droop control as shown in Fig. 2.3, where n is the voltage droop coefficient.

The proposed strategy is explained by considering the possible operating conditions which form a set of scenarios as summarized in Fig. 2.4. When the SOC is less than a predefined minimum limit called SOC_{min} , the control strategy places higher priority on charging the battery and lower priority on sharing power. On the other hand, when the SOC is higher than SOC_{min} and less than a certain predefined limit called \overline{SOC}_{max} the hybrid unit shares power with the microgrid based on the available PV power and stores the excess energy in the battery. When the SOC exceeds \overline{SOC}_{max} , the hybrid unit starts to supply the maximum available power to the microgrid as long as there is sufficient load demand; otherwise, it will autonomously match the available load and continue store the surplus power. If the SOC reaches SOC_{max} , it means that the available power is higher than the load and the SOC is exceeding the permitted limit. In this scenario, the PV curtailment control loop ceases MPPT operation and reduces the PV power to follow the varying load.

Some conditions from the different scenarios can occur simultaneously. For example, during any operation scenario, the load may exceed the available generation and the system will start operating in the power balancing scenario where the battery will supply the deficit power. The operating scenarios along with the proposed droop concept are

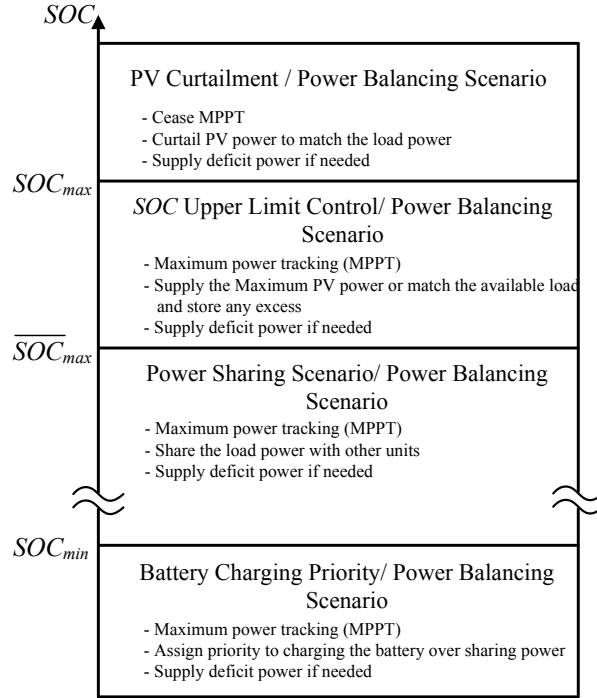


Figure 2.4: Brief description of the proposed operating scenarios objectives.

discussed in the following subsections.

2.5.1 Power Sharing Scenario

The multi-segment adaptive droop approach is illustrated in Fig. 2.5. In this operating scenario, the slope \tilde{m}_{pv} is adaptively determined based on the maximum PV power available at the DC-link ($P_{pvo-MPPT}$) as $\tilde{m}_{pv} = \Delta f_{max} / P_{pvo-MPPT}$. Therefore, the PV/battery unit shares the load with the droop controlled units, and supplies its maximum PV power ($P_{pvo-MPPT}$) only when all other units reach their rated powers at $f = f_{min}$. Consequently, the battery will not supply any power to the microgrid unless all units reach their ratings, as will be explained in the following subsection.

The droop slope limits and the change in the droop characteristic based on the PV power are shown in Fig. 2.6. The minimum slope limit m_{pv-min} is set by the PV array power rating while the maximum slope m_{pv-max} is set based on two factors. The first is the small-signal stability limit of the droop slope [82]. The second is the chosen power sharing capability of this unit when PV power is unavailable. For example, in this work m_{pv-max} is calculated based on 25% of the PV array rating. In other words, the hybrid unit will behave as a droop controlled unit with a power capacity of 25% of the nominal PV array rating. Therefore, the battery will supply only a quarter of the PV rating when all the other units reach their rated limits. Any load increase beyond that point will be

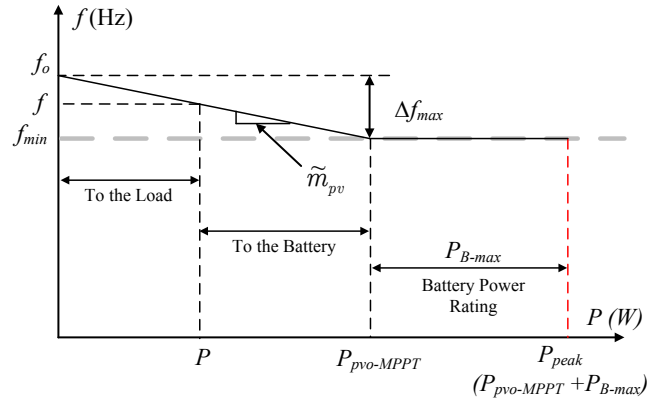


Figure 2.5: Multi-segment adaptive droop characteristics illustrating the power sharing operating scenario.

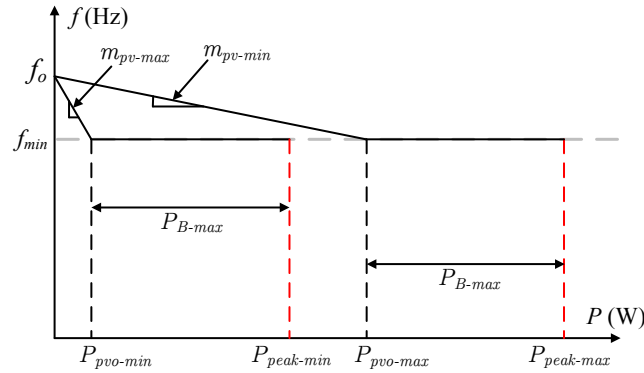


Figure 2.6: Adaptive droop slope limits based on the available power.

supplied solely by the battery.

Due to the fact that $P_{pvo-MPPT}$ changes with solar irradiance and temperature, the value of $P_{pvo-MPPT}$ is passed through a transition rate limiter before it is used to calculate the droop slope, in order to mitigate fluctuations in the power supplied to the microgrid.

Since the power share of the hybrid unit can be less than $P_{pvo-MPPT}$ for most of the time during this operating scenario, the excess energy at the DC-link is transferred to the battery by the bidirectional DC-DC converter. This is done by the bidirectional converter through regulating the DC-link voltage, and hence it ensures the power balance at the DC-link. The battery continues being charged through the bidirectional DC-DC converter until the SOC reaches \overline{SOC}_{max} or the load demand becomes larger than $P_{pvo-MPPT}$. The complete implementation of the multi-segment adaptive droop control will be detailed in Section 2.6.

2.5.2 Power Balancing Scenario

According to the droop control principle, the microgrid frequency is reduced cooperatively by all the droop controlled units in response to any load increase. The frequency f reaches f_{min} when all units supply their rated power regardless of the different ratings and droop slopes of these units. At this point, the hybrid unit will be delivering all the available PV power to the microgrid. If the load increases beyond this point, all other units attempt to reduce the frequency further, while the hybrid unit starts regulating the microgrid frequency at f_{min} according to the flat segment in the proposed droop characteristics (Fig. 2.5). This results in the hybrid PV/battery unit supplying the deficit power while the other units are holding at their respective power rating limits. This is an application of the droop control principle which is commonly used in grid connected DG units that rely on voltage-mode control [36, 65].

Since the power supplied to the microgrid is larger than $P_{pvo-MPPT}$, the DC-link voltage tends to drop due to the energy imbalance at the DC-link capacitor. Therefore, the battery bidirectional converter supplies the power necessary to regulate the voltage at the DC-link and to ensure the internal power balance.

2.5.3 SOC Upper Limit Control Scenario

Once the SOC increases beyond the predefined limit \overline{SOC}_{max} (Fig. 2.4), the adaptive droop control starts to regulate the SOC at \overline{SOC}_{max} . A PI control loop is used to regulate the SOC by reducing the slope of the adaptive droop until the unit supplies all the PV power ($P_{pvo-MPPT}$) to the microgrid, while reducing the battery charging power to zero. The change in the slope generated by the PI control loop to regulate the SOC is represented by the variable $\tilde{m}_{soc-max}$ as will be illustrated in Section 2.6.

The operation of the proposed adaptive droop using two DG units and three operational cases is illustrated in Fig. 2.7, where P_H refers to the output power of the hybrid unit (Unit 1), while P_D refers to that of the conventional droop controlled unit (Unit 2). In Case I, the PV/battery unit shares the load with the other unit, and the surplus PV energy is stored in the battery. In this case the operating points for both units are identified in Fig. 2.7 as A_1 and A_2 , respectively.

As the SOC increases and reaches the limit \overline{SOC}_{max} the controller starts to reduce the slope of the adaptive droop until all the PV power $P_{pvo-MPPT}$ is supplied to the microgrid ($P_H = P_{pvo-MPPT-1}$) while the power delivered by the other unit (P_D) decreases accordingly. This is shown by Case II of Fig. 2.7, where the new operating points are identified as B_1 and B_2 .

For any change in $P_{pvo-MPPT}$ and/or the load, the slope of the droop slope will be changed accordingly by the PI control loop to keep supplying the PV available power to the microgrid and keep regulating the SOC . This is illustrated by Case III when $P_{pvo-MPPT}$ changes from $P_{pvo-MPPT-1}$ to $P_{pvo-MPPT-2}$, with the operating points are referred to as C_1 and C_2 .

In this scenario, the hybrid unit supplies the maximum PV power to the microgrid only if there is enough load demand and, hence, maintains the power balance in the islanded microgrid. This is due to the fact that the PV/battery unit is designed to

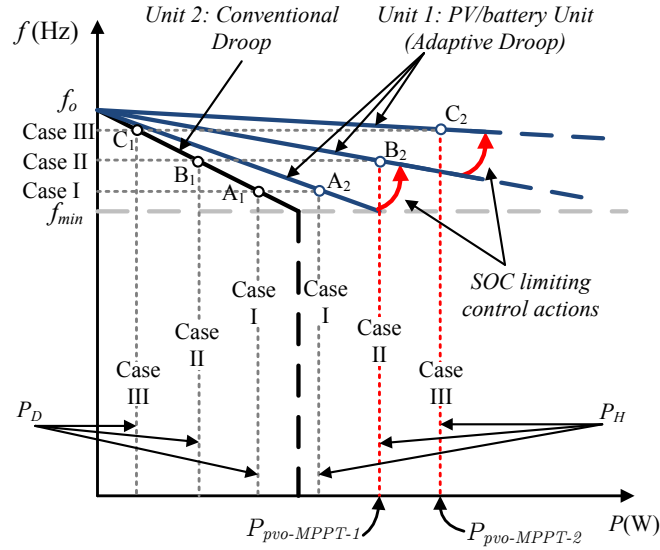


Figure 2.7: Adaptive droop actions to regulate the SOC at its limit. Case I: Power sharing scenario – operating points A_1 and A_2 . Case II: SOC upper limit control – operating points B_1 and B_2 . Case III: SOC upper limit control – operating points C_1 and C_2 .

operate as a voltage source that tries to control the output power by modifying the droop slope, in contrast to the PV control strategies in the literature that are designed to operate as current controlled sources.

On the other hand, when the load demand in the microgrid is less than $P_{pv0-MPPT}$, the adaptive droop will become flat (slope=0) due to the PI control action and the PV/battery unit will supply the entire load, reducing the power share of the other units to zero. In this case, the hybrid unit will continue matching the load, and the battery will continue charging with the remaining power until the SOC reaches the absolute SOC_{max} .

At this point the PV curtailment control loop mentioned in Section 2.4 starts to regulate the SOC at SOC_{max} by adjusting the PV operating point to match the load. If the load becomes higher than the available PV power, the SOC will drop below SOC_{max} , but it will still be higher than \overline{SOC}_{max} . Consequently, the hybrid unit will continue to supply the increasing load demand from the battery while regulating the frequency at $f = f_0$. All other units will continue supplying no power until the SOC drops below \overline{SOC}_{max} . At this point, the droop slope starts to increase again to supply $P_{pv-MPPT}$ only, with the battery neither absorbing nor supplying any power.

2.5.4 Battery Charging Priority Scenario

The control strategy places a higher priority on charging the battery, rather than on operating in the power sharing scenario when the SOC is less than SOC_{min} . The choice

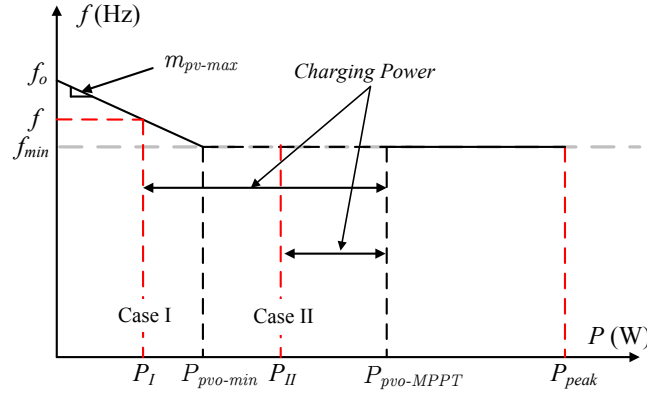


Figure 2.8: Adaptive droop control behavior during battery charging priority scenario considering two loading cases

of SOC_{min} depends on designer preference and the expected level of battery usage when the PV power is unavailable. For example, SOC_{min} is chosen as 60% in this investigation. Assigning priority to battery charging is achieved by increasing the slope of the adaptive droop through a PI control loop until it reaches m_{pv-max} . The increase in the droop slope introduced by the PI control loop is represented by the variable $\tilde{m}_{soc-min}$ as will be illustrated in Section 2.6.

As mentioned earlier, in this work, m_{pv-max} is calculated based on $P_{pvo-min}$, which is 25% of the PV array rating. The hybrid unit supplies its power share based on the droop slope m_{pv-max} while the remaining PV power is being supplied to the battery as illustrated in Fig. 2.8 (Case I). When all units reach their maximum power the hybrid unit will be supplying $P_{pvo-min}$. Any increase in the load beyond $P_{pvo-min}$ will be supplied first from the available PV power due to the extended flat segment in the droop characteristic as shown in Fig. 2.8 (Case II). If the load demand increases beyond $P_{pvo-MPPT}$, the additional load power will be supplied by the battery. Therefore, even though the priority is given to charging the battery, the hybrid unit will always try to keep the power balance in the system, which is always the ultimate priority for any islanded microgrid.

It is worth mentioning that if the SOC reaches the absolute minimum SOC stated by the battery manufacturer, the system must shed some loads or shut down the microgrid. This cannot be avoided by any power management strategy. Mitigating this requires optimizing the size of the battery [83], and is beyond the scope of this work.

2.6 Implementation of the Adaptive Droop

The implementation of the multi-segment adaptive droop strategy that can facilitate the aforementioned four operating scenarios is shown in Fig. 2.9. The variable \tilde{m} represents the slope of the middle segment in the proposed adaptive droop characteristics. As can be seen from Fig. 2.9, \tilde{m} is generated by adding the three slope variables mentioned

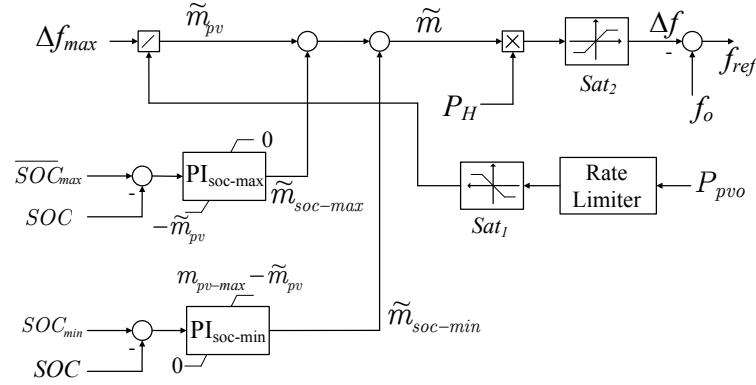


Figure 2.9: Proposed adaptive droop implementation.

previously, \tilde{m}_{pv} , $\tilde{m}_{soc-max}$, and $\tilde{m}_{soc-min}$.

As can be seen from Fig. 2.9, the saturation limits of the controllers $PI_{soc-max}$ and $PI_{soc-min}$ are chosen such that the controllers remain idle, i.e., both $\tilde{m}_{soc-max}$ and $\tilde{m}_{soc-min}$ equal zero, when $SOC_{min} \leq SOC \leq \overline{SOC}_{max}$. In this case, the slope \tilde{m} is solely determined by \tilde{m}_{pv} and the system is operating in the power sharing scenario. The slope \tilde{m}_{pv} in Fig. 2.9 is calculated as explained in Section 2.5.1.

The controller $PI_{soc-max}$ remains inactive ($\tilde{m}_{soc-max} = 0$) and can only go negative when the SOC increases above \overline{SOC}_{max} . At this point, $\tilde{m}_{soc-max}$ starts to go negative in order to reduce the slope \tilde{m} and regulate the SOC at \overline{SOC}_{max} as explained in the SOC limit control scenario. Similarly, the $PI_{soc-min}$ control loop starts to contribute to the slope \tilde{m} only when the SOC starts to decrease below SOC_{min} . Note that the $PI_{soc-max}$ and $PI_{soc-min}$ control loops can never be active simultaneously.

The lower saturation limit of $PI_{soc-max}$ is continuously adjusted to $-\tilde{m}_{pv}$ so that \tilde{m} is limited between 0 and \tilde{m}_{pv} during the SOC limit control scenario. Similarly, the upper saturation limit of $PI_{soc-min}$ is set to $(m_{pv-max} - \tilde{m}_{pv})$. Therefore, \tilde{m} is limited between \tilde{m}_{pv} and m_{pv-max} during the battery charging priority scenario. These saturation limits are adjusted continuously since \tilde{m}_{pv} is changing based on the available PV power. The saturation limit block Sat_1 in Fig. 2.9 is used to indirectly set the maximum limit of \tilde{m}_{pv} at m_{pv-max} by setting the PV power lower limit to P_{pv-min} . Sat_2 operates on the frequency deviation (Δf), not on the slope, to generate the flat lines in the adaptive droop characteristics. These limits are set to zero and Δf_{max} .

2.7 Control Design and Stability Analysis of the SOC and the PV Curtailment control Loops

The designs of voltage controllers for the DC-DC converters and VSCs are well established in the literature. In this work, the voltage controllers for the DC-DC converters are designed as in [50], and the voltage tracking loops for the VSCs are designed as in [14]. The structures and the parameters of these controllers are presented in Appendix A.

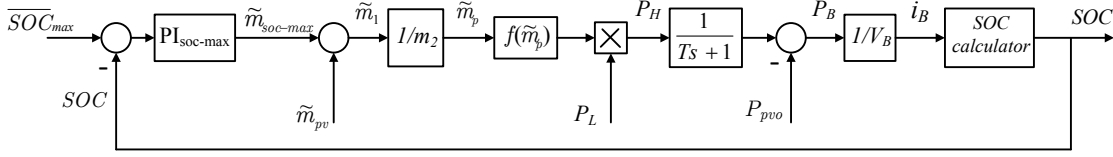


Figure 2.10: Approximated model of the SOC upper limit control loop.

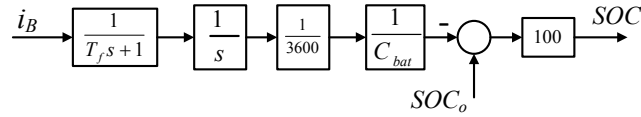


Figure 2.11: Block diagram illustrating the SOC calculation based on the coulomb counting principle.

Also, the small-signal stability analysis of the microgrid to determine the stable limit of the adaptive droop slope can be found in [84, 85]. Therefore, the analysis in this section is focused on investigating the small-signal models of the proposed SOC control loops to gain insight into the dynamics of these loops. Without loss of generality, the following analysis assumes a two-unit microgrid. The microgrid parameters are shown in Table 2.1.

2.7.1 Small-Signal Modeling of the SOC Control Loops

Due to the nonlinear nature of the considered SOC control loops, a small-signal model will be developed to study the dynamics of the considered loop around an operating point. The change in SOC is very slow in nature in comparison to the dynamics of the DC-DC converters, the DC-link, the VSCs, and the microgrid. Therefore, the SOC dominates the dynamics of the considered loops.

The approximated averaged model for the SOC control loops is proposed in Fig. 2.10 as the first step in developing the linearized model. The approximated model is shown for the $PI_{soc-max}$ control loop; however, it can also be used for the $PI_{soc-min}$ control loop. The efficiency of the power converters is assumed to be unity for simplicity. The LPF in Fig. 2.10 is used to include the dynamics of the power filter (see Fig. 2.3) as it is known that the dynamics of the droop control system are governed by the low frequency cut-off filters [85]. V_B represents the battery voltage at the considered operating point.

Regardless of the technique used to estimate the SOC , the SOC can be modeled based on the coulomb counting method as in Fig. 2.11 where C_{bat} is the battery capacity in Ah and SOC_o is the initial SOC . The nonlinear function $f(\tilde{m}_p)$ in Fig. 2.10 determines the relationship between the load demand power P_L and the power supplied by the hybrid unit (P_H), as follows:

Table 2.1: System Parameters

Description	Parameter	Value
Nominal DC-link Voltage	V_{dc-ref}	400 V
Nominal Battery Voltage	V_B	192 V
Battery Capacity	C_{bat}	32 Ah
PV Open Circuit Voltage	V_{oc}	287.26 V
PV Short Circuit Current	I_{sc}	7.73 A
PV Array Power Rating	P_{pv-max}	1.6 kW
Feeder Inductance	L	4 mH
Feeder Resistance	R	1.1 Ω
Frequency Droop - Unit 2	m_2	0.9817×10^{-3} (rad/s)/W
Frequency Droop Limit	Δf_{max}	0.25 (Hz)
Voltage Droop Coefficient	n_1, n_2	0.005 V/VAR
Time Constant of the Power LPF	T	0.032 s

$$P_H = f(\tilde{m}_p)P_L \quad (2.1)$$

where

$$f(\tilde{m}_p) = \frac{1}{1 + \tilde{m}_p} \quad (2.2)$$

$$\tilde{m}_p = \frac{\tilde{m}_1}{m_2} \quad (2.3)$$

where \tilde{m}_1 and m_2 are the droop coefficients of the hybrid unit (Unit 1) and the droop controlled unit (Unit 2), respectively.

The proposed approximated model is validated for two sets of controller gains against the detailed switching model as shown in Fig. 2.12. The models are simulated in PSCAD/EMTDC around an arbitrarily chosen operating point. The selected controller gain sets (K_{p-soc}, K_{i-soc}) are (0.5,0.4), designated as Controller 1, and (0.5,1) designated as Controller 2. The operating point is defined by: $\overline{SOC}_{max}=85\%$, $P_{pvo}=1.55$ kW, a load power (P_{Lo}) of 2 kW, and $V_B=192$ V. Also, in Fig. 2.12, a load disturbance (ΔP_L) of ∓ 200 W is considered to examine the approximated model. A good match between the detailed and the approximated model is shown in Fig. 2.12, for both sets of controller gains. However, the approximated model is still nonlinear due to the nonlinear function $f(\tilde{m}_p)$. To develop a small-signal model of the loop, $f(\tilde{m}_p)$ can be approximated by a linear function around the operating point \tilde{m}_{po} as

$$f(\tilde{m}_p) \approx f(\tilde{m}_{po}) + \left. \frac{df(\tilde{m}_p)}{d\tilde{m}_p} \right|_{\tilde{m}_{po}} \Delta\tilde{m}_p \quad (2.4)$$

where

$$\left. \frac{df(\tilde{m}_p)}{d\tilde{m}_p} \right|_{\tilde{m}_{po}} = \frac{-1}{(1 + \tilde{m}_{po})^2} = k_{mpo} \quad (2.5)$$

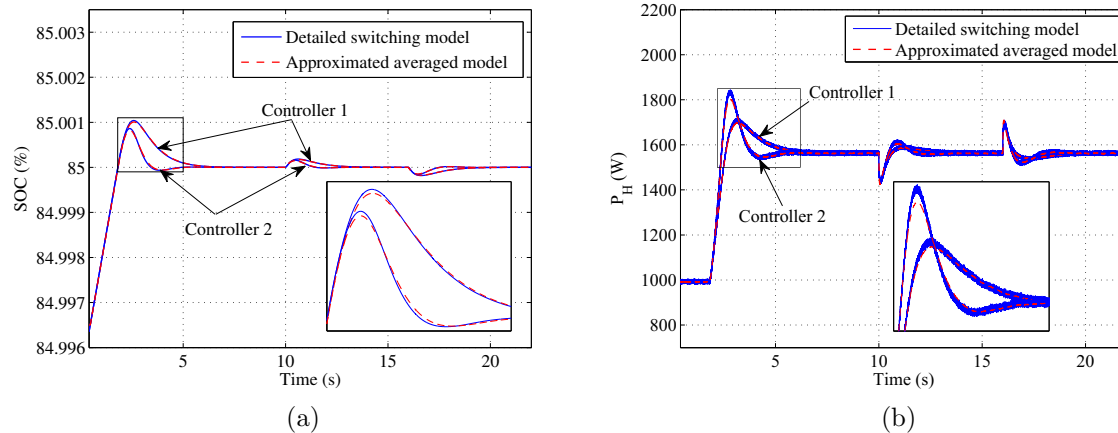


Figure 2.12: Validation of the approximated model of the SOC upper limit control loop for two different gain sets. (a) SOC transient response. (b) Output power (P_H) transient response.

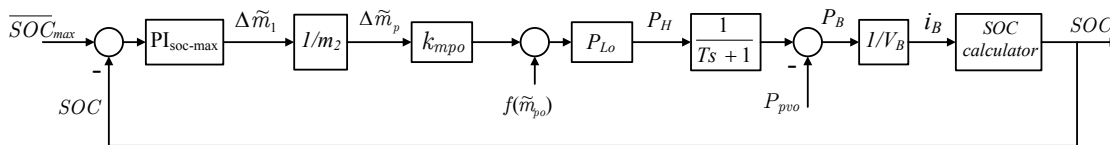


Figure 2.13: Linearized model of the SOC upper limit control loop.

The linearized averaged model is shown in Fig. 2.13. The linearized model is validated in Fig. 2.14 against the detailed switching model during the 200 W load disturbance. A good match between the detailed switching model and the approximated and linearized models is illustrated. Consequently, the open-loop transfer function can be derived from Fig. 2.13 as follows:

$$G_1(s) = \frac{(K_{p-soc}s + K_{i-soc})k_{mpo}K_1}{s^2(Ts + 1)(T_f s + 1)} \quad (2.6)$$

where

$$K_1 = \frac{-100P_{Lo}}{3600m_1V_B C_{bat}} \quad (2.7)$$

and T_f is the time constant of battery current filter which is chosen as 0.001 s. Using (2.6) the characteristic equation of this loop is given by

$$TT_f s^4 + (T + T_f)s^3 + s^2 + k_{mpo}K_1K_{p-soc}s + k_{mpo}K_1K_{i-soc} = 0 \quad (2.8)$$

The dominant roots of the characteristic equation are shown in Fig. 2.15 for the same operating point used in Fig. 2.12, when $K_{p-soc}=0.5$ and K_{i-soc} is changed from 0.1 to

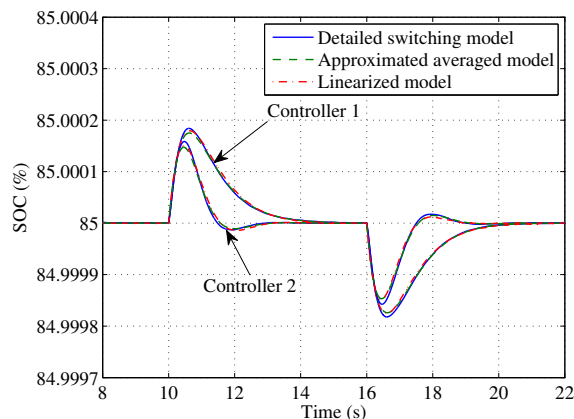


Figure 2.14: Transient response of the linearized model vs. the approximated and the detailed model of the SOC upper limit control loop.

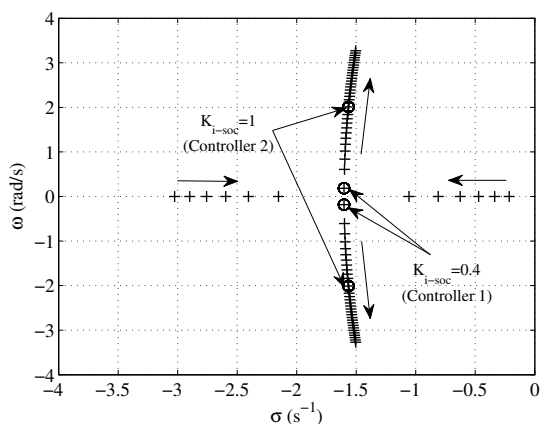


Figure 2.15: Dominant root trajectories of the SOC control loop.

2 with a step of 0.01. As shown in Fig. 2.15, the chosen controller gain sets result in under-damped roots ($\zeta=0.993$) that are very close to the critical ones for Controller 1 vs. $\zeta=0.623$ for Controller 2. Even though Controller 2 results in a faster SOC transient response, it requires a higher power transient to achieve this response (see Fig. 2.12b). This is due to the fact that the SOC control is a very slow process and requires high power (control effort) excursions to speed up the response. Therefore, faster controllers will result in higher power transients. The linearized model can be used along with simulation to study the performance and stability of the control loop for different operating points and controller gains. In this work, Controller 1 is considered adequate for the application and used for both $PI_{soc-max}$ and $PI_{soc-min}$ to validate the proposed control system experimentally.

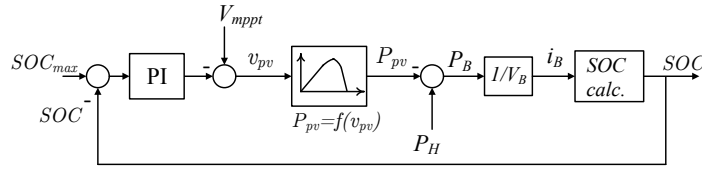


Figure 2.16: Approximated model of the PV curtailment control loop.

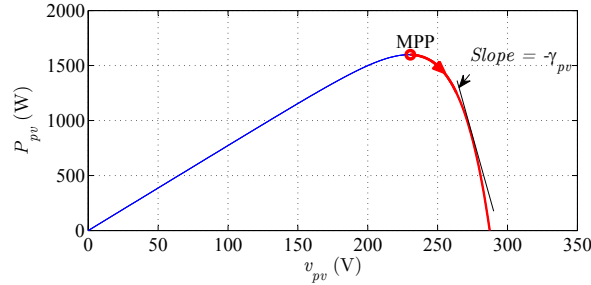
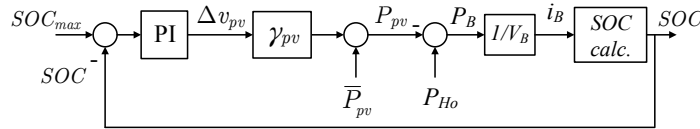

 Figure 2.17: PV power characteristic (Irradiance= $1000 \text{ W}/\text{m}^2$, $T=25 \text{ C}^\circ$) where a straight line is used to approximate the characteristic between the points of $P_{pv}=1000 \text{ W}$ and 800 W .


Figure 2.18: Linearized model of the PV curtailment control loop.

2.7.2 Small-Signal Modeling of the PV Curtailment Control Loop

By the time this loop starts operating the SOC limit control loop is already saturated at $\tilde{m} = 0$ (Section 2.5.3). Therefore, there will be no interaction between the PV curtailment and the SOC control loops, and hence the PV curtailment loop can be modeled separately. Neglecting the dynamics of the power converters, as discussed previously, results in the approximated model in Fig. 2.16. The function $f(v_{pv})$ represents the PV power characteristic under specific weather conditions. This is a nonlinear function, however, it can be approximated by a straight line in the PV characteristic region under consideration as shown in Fig. 2.17, where $-\gamma_{pv}$ represents the slope of the line. Consequently, the linearized model is shown in Fig. 2.18, where \bar{P}_{pv} and P_{Ho} define the PV power and the delivered power, respectively, at the considered operating point.

The linearized model is validated against the detailed switching model simulated in PSCAD/EMTDC, as shown in Fig. 2.19. The simulation results show how the models

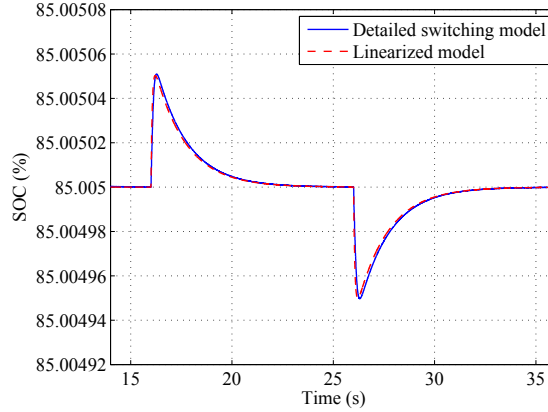


Figure 2.19: Transient response of the linearized model vs. the detailed switching model of the PV curtailment control loop, for load disturbances of -200 W at $t=16$ s and $+200$ W at $t=26$ s.

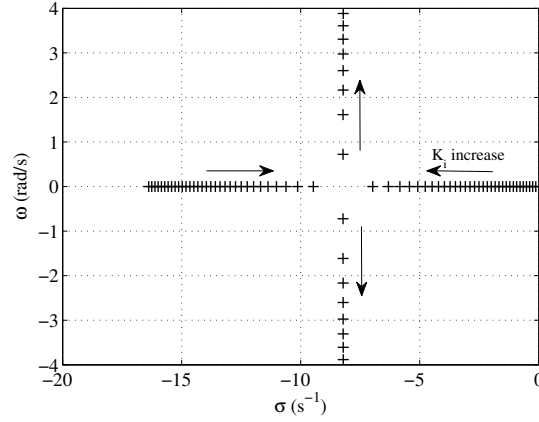


Figure 2.20: Dominant root trajectories of the PV curtailment control loop.

respond to disturbances in the load by regulating the PV operating point to keep the SOC regulated at SOC_{max} . In the considered operating scenario \bar{P}_{pv} is chosen as 1000 W, which matches the power consumed by the load. To illustrate the effect of a load disturbance, the load is then dropped to 800 W and then returned to 1000 W. Accordingly, $-\gamma_{pv}$ can be calculated from the PV characteristic in Fig. 2.17 as -44.9 W/V. SOC_{max} is set to be 85.005% ($\overline{SOC}_{max} + 0.005\%$) to reduce the simulation time required to reach this level. The linearized model illustrates a good match with the detailed switching model. From Fig. 2.18, the open loop transfer function of the linearized model can be written as

$$G_2(s) = \frac{-(K_p s + K_i) \gamma_{pv} K_2}{s^2 (T_f s + 1)} \quad (2.9)$$

where

$$K_2 = \frac{100}{3600 V_B C_{bat}} \quad (2.10)$$

From (2.9), the closed-loop characteristic equation is given by

$$T_f s^3 + s^2 - K_p \gamma_{pv} K_2 s - K_i \gamma_{pv} K_2 = 0 \quad (2.11)$$

To gain insight into the effect of the controller gains on the closed-loop poles, the root locus of the dominant poles for the operating conditions considered in the simulation is shown in Fig. 2.20. The dominant root trajectories are calculated for $K_p = 80 \times 10^3$ and K_i is changed from 10×10^3 to 4×10^5 . The gains used in the simulation of Fig. 2.19 ($K_p = 80 \times 10^3$, $K_i = 40 \times 10^3$) are also employed to validate the control strategy experimentally. The linearized model can be used along with simulation to further optimize the controller gains for different PV power and loading conditions.

2.8 Experimental Evaluation

The control strategy is evaluated using a series of experiments on a laboratory-scale microgrid. The experimental setup and the results are presented in the next two subsections.

2.8.1 Experimental Setup

The experimental setup consists of two DG units connected to a resistive load through a three-phase bus, as shown in Fig. 2.21. Unit 2 is the conventional droop controlled unit, which is a 3-phase inverter powered by a Chroma 62050H power supply. Unit 1 is a hybrid system consisting of a bidirectional DC-DC converter connected to a lead-acid battery bank, a unidirectional DC-DC converter powered by a Chroma 62050H running in PV simulator mode, and a 3-phase inverter. The inverters are based on Powerex PS22A78-E IGBT modules. Current and voltage sensing are implemented using LEM LA 20-PB and LV-20-P Hall effect sensors, respectively. Other system parameters are shown in Table 2.1 for both units.

The converter controllers are implemented in Simulink, compiled using the Embedded Coder toolchain, and run on Spectrum Digital eZdsp boards containing Texas Instruments TMS320F28335 32-bit floating-point microcontrollers. The power levels and the *SOC* are calculated by the controllers and made available over Texas Instruments serial-to-Ethernet interfaces for data collection and plotting purposes. The software that collects this data is programmed in the Python language and hosted on a PC running Ubuntu Linux. The recorded data is then plotted offline. A photograph of the experimental apparatus is shown in Fig. 2.22.

2.8.2 Experimental Results

Power Sharing Scenario

The results in Fig. 2.23 show how the hybrid PV/battery unit (Unit 1) shares power with the droop controlled unit (Unit 2) based on the available PV power (P_{pv0}). The solar irradiance changes at $t = t_1$, starting from 540 W/m^2 and settling at 1080 W/m^2 with

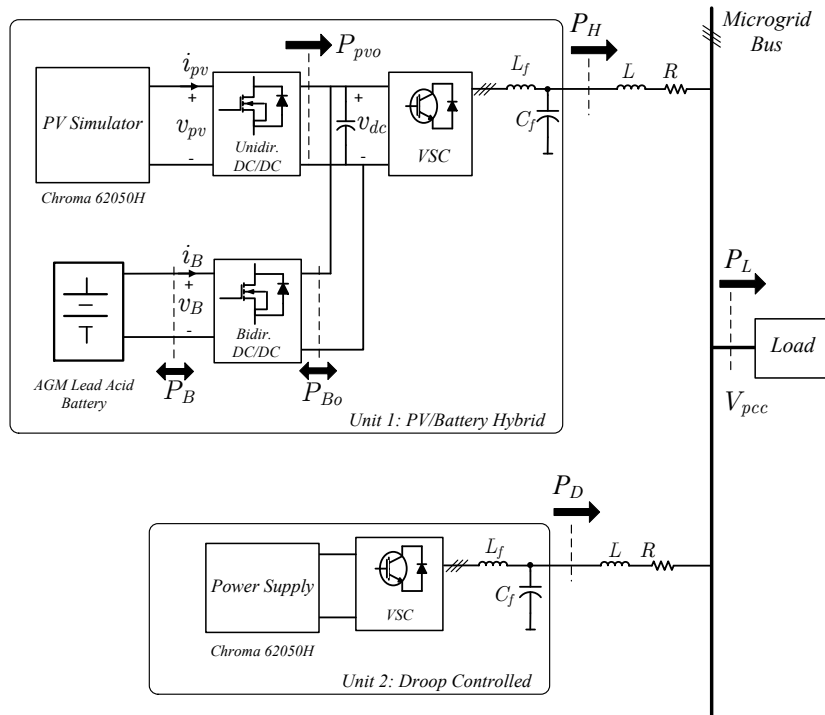


Figure 2.21: Schematic diagram of the two-unit microgrid prototype.

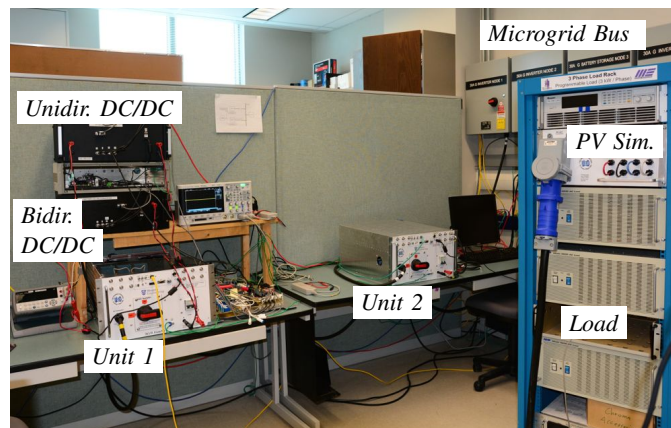


Figure 2.22: The experimental apparatus.

some random fluctuations. Accordingly, P_{pvo} changes from 810 W to 1600 W and the hybrid unit adapts the droop slope based on the available PV power. The change in the droop slope and, accordingly, the power sharing is limited by the transition rate limiter shown in Fig. 2.9. Therefore, the fluctuations in the PV power are effectively suppressed in the power supplied to the microgrid. The rate limiter setting is chosen as 20 W/s to illustrate the concept, but can be changed in practice based on the dynamics of the other dispatchable sources [86].

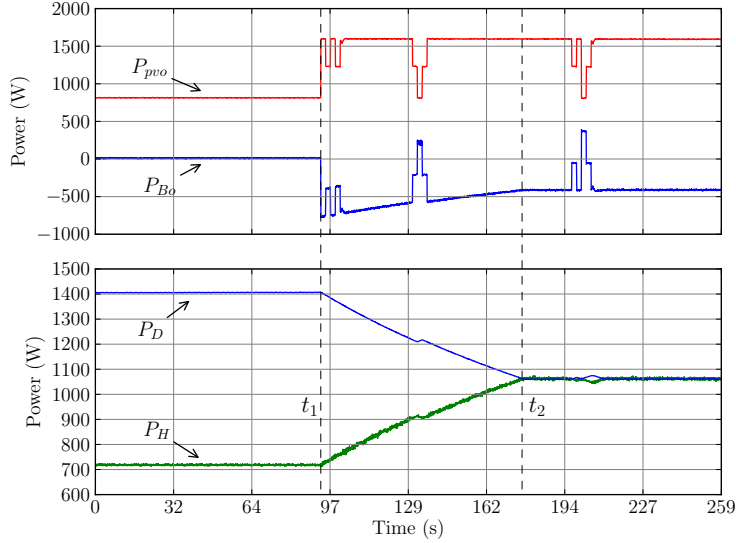


Figure 2.23: Experimental performance of the proposed strategy during the power sharing scenario.

As can be seen from Fig. 2.23, when $t \geq t_2$ both units share the load equally since P_{pvo} equals the power rating of the other unit (Unit 2), which is 1600 W in this system; whereas the hybrid unit supplies approximately half of P_D when P_{pvo} is 810 W ($t \leq t_1$). The excess PV power is directed to the battery when $P_{pvo}=1600$ W; however, the battery does not absorb any power when $P_{pvo}=810$ W since the surplus PV power approximately covers the power losses in the VSC converter.

Power Balancing Scenario

The results in Fig. 2.24 illustrate how the hybrid unit supplies the deficit power to maintain the power balance in the microgrid. At the beginning, the hybrid unit shares power based on the available PV power (810 W) and stores the surplus PV power. Therefore, P_H is approximately half of P_D until $t=t_1$ when the load exceeds the total of the available PV power and the power rating of the droop controlled unit combined. At this point, the hybrid unit starts operating in the flat segment of the droop characteristic while supplying the deficit power as discussed in Section 2.5.2. The battery switches from absorbing to supplying power at t_1 . When the load increases further at $t=t_2$, the hybrid unit matches the increased load from the battery due to the flat droop segment while the other unit keeps holding P_D regulated at 1600 W. The system goes back to operating in the power sharing scenario when the load drops below the total generation as illustrated in Fig. 2.24.

SOC Upper Limit Control Scenario

The results in Fig. 2.25a show the hybrid unit operating in the power sharing scenario until the SOC exceeds \overline{SOC}_{max} (85%). At this moment, the SOC upper limit control

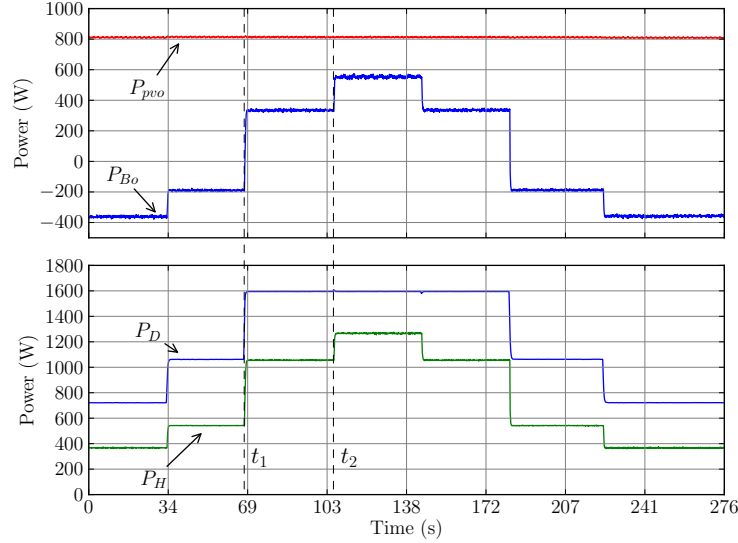


Figure 2.24: Experimental results showing the power balancing operating scenario.

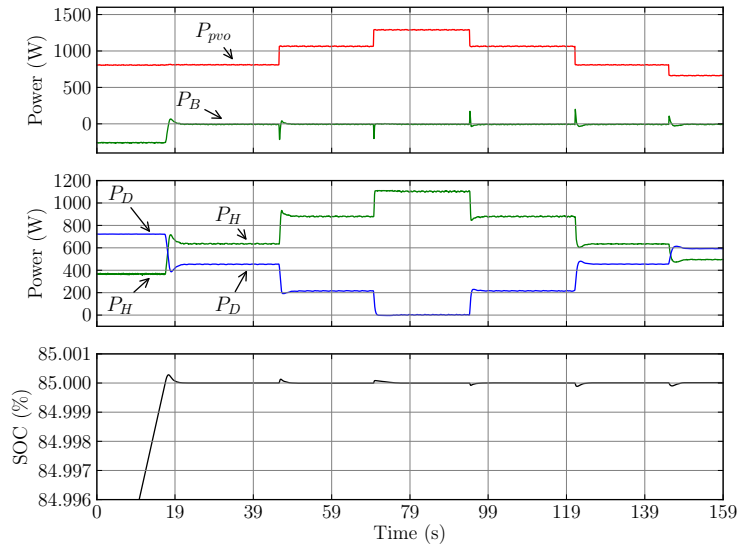
loop starts reducing the droop slope so that all the available PV power (after losses) is supplied to the microgrid, while regulating the SOC at \overline{SOC}_{max} . Consequently, the power flowing into the battery (P_B) is reduced and regulated at 0 W.

The solar irradiance is stepped up and down several times as shown in Fig. 2.25a to examine the performance of this control loop in response to PV power variations. The SOC control loop reacts to the change in the PV power by controlling the adaptive droop slope to supply the available PV power at any time to the microgrid while keeping P_B regulated at zero and the SOC at \overline{SOC}_{max} .

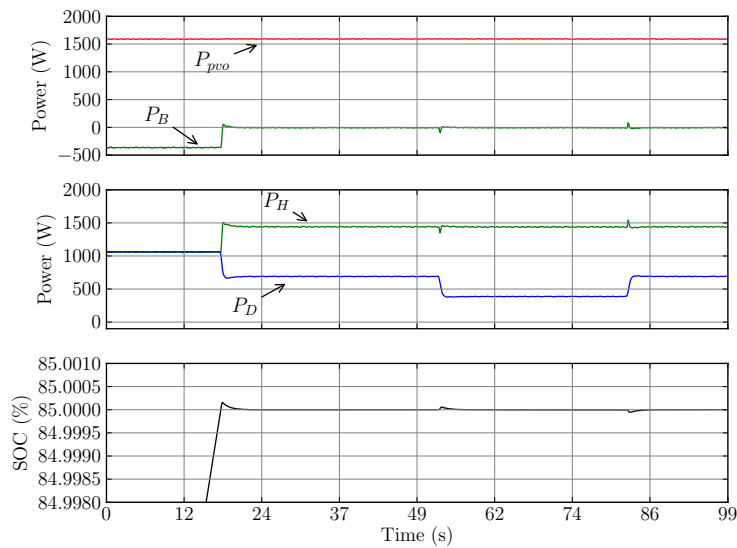
The performance of the considered SOC control loop in response to load changes is shown in Fig. 2.25b. When the load decreases, the SOC control loop reduces the droop slope to keep supplying the available PV power to the microgrid (including power losses) and to keep P_B regulated at zero.

PV Curtailment Control Scenario

The performance of the microgrid when the SOC reaches its upper limit (SOC_{max}) and the available PV power is higher than the total load demand of the microgrid is shown in Fig. 2.26. The hybrid unit is initially operating in the power sharing scenario where both units share the load power equally and the battery is being charged with about 750 W at the battery terminals (P_B). The SOC continues to increase until the SOC passes the first limit \overline{SOC}_{max} , then the SOC upper limit control loop reduces the droop slope until the hybrid supplies all the load and P_1 is reduced to zero. The battery continues to charge with the remaining PV power until the SOC exceeds SOC_{max} at $t = t_1$. At this point, the PV curtailment control loop ceases MPPT operation and modifies the PV array voltage reference v_{pv-ref} so that the PV power matches the microgrid load. As can be seen in Fig. 2.26, between $t = t_1$ and t_2 the controller keeps adjusting the PV operating point autonomously to match the changing load while the MPPT is still idle.



(a)



(b)

Figure 2.25: Experimental results showing the performance of the proposed strategy during the *SOC* upper limit control scenario. (a) Control strategy response to PV power changes (solar irradiance changes). (b) Control strategy response to load changes.

The PV curtailment control loop keeps decreasing the PV array voltage to match the increasing load power until $t=t_2$ when the load power becomes higher than the available PV power. The *SOC* then becomes less than SOC_{max} , the internal power management system starts the MPPT again, and the battery starts supplying the additional needed power.

Between $t = t_2$ and t_3 , the hybrid unit continues matching the changing load while

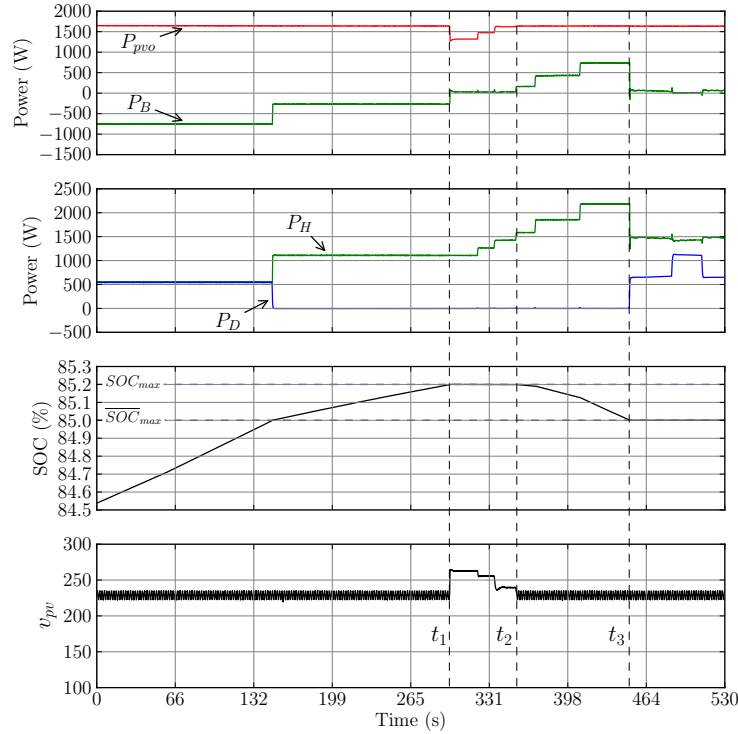


Figure 2.26: Experimental results showing the performance of the proposed strategy when the SOC exceeds the maximum limits and both the SOC upper limit control loop and the PV curtailment control loops start operating.

the droop controlled unit supplies no power. This is because the SOC is still higher than \overline{SOC}_{max} and the SOC control loop has pushed the droop to saturate at zero slope as intended. Therefore, the hybrid unit will continue to supply the whole load from the PV and the battery until the SOC drops below \overline{SOC}_{max} or the load increases beyond the hybrid unit rating. In other words, the hybrid unit gives priority to supplying the excess power from the battery when the SOC is higher than \overline{SOC}_{max} .

At $t = t_3$, the SOC drops below \overline{SOC}_{max} causing the SOC upper limit control loop to reduce the droop slope in order to regulate the SOC at \overline{SOC}_{max} . Therefore, as can be seen from Fig. 2.26, the hybrid unit output power P_H drops so that it supplies only the PV power to the microgrid, P_B drops to zero, and the droop controlled unit supplies the rest of the load power. The system continues to supply all the available PV power to the microgrid, and to regulate the SOC at \overline{SOC}_{max} while the droop controlled unit meets the rest of the load.

Battery Charging Priority Scenario

This operation scenario is illustrated in Fig. 2.27. This system is initially operating in the power balancing scenario where the battery is supplying a deficit power of 670 W and the SOC is continuously decreasing. When the SOC drops below SOC_{min} (60% here) the battery charging priority control loop starts to increase the adaptive droop slope to

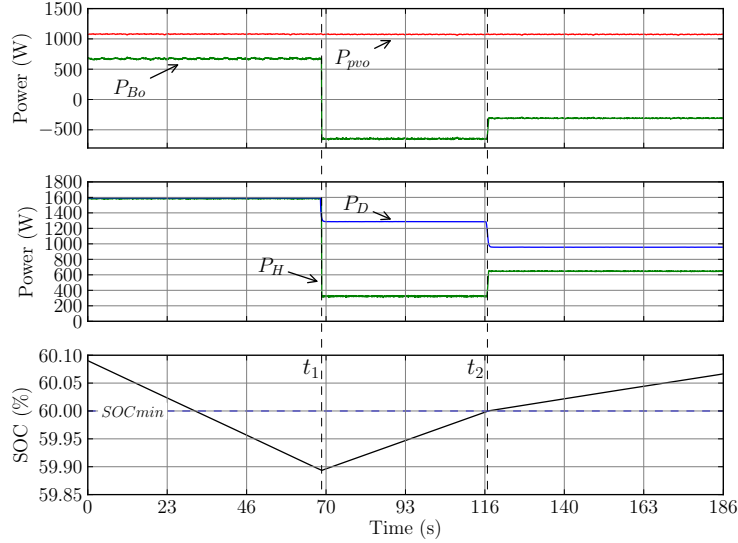


Figure 2.27: Experimental performance during the battery charging priority scenario.

reduce the power share supplied to the microgrid. However, since the system is already operating in the power balancing scenario, the hybrid unit continues to operate in the extended flat segment of the droop characteristic to maintain the power balance in the microgrid (see Fig. 2.8 – Case II).

Once the load drops below the total generation in the microgrid at $t=t_1$, the hybrid unit autonomously starts sharing power according the maximum droop slope m_{pv-max} (see Fig. 2.8), in order to place a higher priority on charging the battery.

Since m_{pv-max} is calculated based on 25% of the PV array rating in this work, as illustrated in Fig. 2.27, the hybrid unit supplies only 320 W during this operating scenario, which is approximately 25% of the power supplied by the droop controlled unit ($P_D=1285$ W). The system continues to work in this scenario until the SOC becomes higher than SOC_{min} at $t=t_2$ when the hybrid unit starts operating in the power sharing scenario.

2.9 Summery and Conclusion

In this chapter, a power management strategy for PV/battery hybrid units in an islanded microgrid has been proposed. The PV/battery unit is controlled to operate as a voltage source that employs an adaptive droop control strategy, in contrast to the PV control strategies in the literature where the PV units are controlled to operate as current controlled sources (the PQ control). It has been shown that controlling the PV/battery unit as a voltage source with the proposed adaptive droop provides the PV/battery hybrid unit with several unique features. First, the hybrid unit has the ability to share the load power with other sources while storing any surplus energy in the battery. Second, it can track and supply the maximum PV power to the microgrid provided that there is sufficient load demand in the microgrid. Otherwise, the hybrid unit will autonomously

match the available load while charging the battery with the excess energy as in standalone strategies. Third, the control strategy modifies the PV operating point to follow the load when the total microgrid load is less than the available PV power and the battery is fully charged. Moreover, the battery may also provide the operational functions that a separate storage unit may provide in an islanded microgrid, such as regulating voltage and frequency, and supplying the deficit power in the microgrid.

Decentralized Control Strategy for PV/Battery Hybrid Units in Islanded Microgrids – Part II: Multi-Segment Adaptive (P/f) Curves Approach

3.1 Introduction

In this chapter, an alternative control strategy is proposed to achieve decentralized power management of PV/battery hybrid units in islanded microgrids. The proposed strategy offers new features in addition to those achieved by the strategy introduced in Chapter 2. More specifically, it eliminates the operational limitations of the former technique, which are:

- When the PV power is very low or not available, e.g. at night, the hybrid unit supplies power based on the maximum droop slope (m_{pv-max}), which is calculated based on a predefined reduced power rating. The reduced power rating is set to 25% of the PV array rating as an example in Chapter 2. This could deplete the battery prematurely, if the battery power rating is close or equal to the reduced power rating. In this case, the battery appears in the microgrid as a droop controlled unit with a power capacity close or equal to the battery power rating.
- During the battery charging priority scenario, the portion of the PV power available to charge the battery is constrained by the maximum limit of the droop slope (m_{pv-max}). Also, the battery can only be charged by the PV power. In other words, the flexibility to support charging the battery from the other units is not offered.
- PV curtailment starts only when the battery SOC reaches the maximum limit of SOC_{max} [54, 55, 57, 62, 64]. However, in practice, the charging power should be reduced gradually when the SOC approaches its maximum limit SOC_{max} , to avoid battery voltage excursions [29, 87–91]. Therefore, a more practical charging control strategy is required.

According to the proposed strategy, the PV unit is controlled as voltage source that follows a multi-segment adaptive power/frequency (P/f) characteristic curve. The proposed P/f characteristics, of the hybrid unit and of the whole microgrid, adapt autonomously to the microgrid operating conditions so that the hybrid unit may supply the maximum PV power, match the load, and/or charge the battery, while maintaining the power balance in the microgrid and respecting the battery state of charge (SOC) limits. These features are achieved without relying on a central management system and communications, as most of the existing algorithms do. The control strategy is implemented using multi-loop controllers, which provide smooth and autonomous transitions between the operating scenarios. The small-signal stability of the proposed control loops is investigated and the system performance is experimentally validated on a 4 kVA microgrid.

The objectives of the proposed control strategy and the problem statement are discussed in Section 3.2. The control strategy is subdivided into two parts, VSC control, and DC-DC converters control. The VSC control system is discussed in detail in Section 3.3, while the DC-DC converters control system is presented in Section 3.4. Small-signal models of the proposed control loops are developed, and stability is analyzed in Section 3.5. Experimental results that validate the proposed control strategy are presented and discussed in Section 3.6, followed by concluding remarks in Section 3.7.

3.2 Problem Statement

The same configuration of the microgrid and the PV/battery hybrid unit that was introduced in Chapter 2 (Section 2.3), is used here as shown in Fig. 3.1. The objective of the proposed control strategy is to coordinate the operation of the PV/battery unit with the other droop controlled units, to deliver the available PV power to the microgrid, while maintaining the power balance in the system and respecting the SOC limits and power rating of the battery. More specifically, the proposed control strategy should provide the following functional features without relying on communications or any central management algorithm:

1. The hybrid unit tracks and delivers all the available PV power to the microgrid after charging the battery to the desired SOC .
2. The hybrid unit can absorb power from the microgrid to support charging the battery without disturbing the power balance in the microgrid. In other words, the power used to charge the battery will vary autonomously based on the varying load and the available power from the PV unit, to ensure that the load demand is met, and to avoid exceeding the power ratings of the other units.
3. If the the available PV power is more than the load demand, the hybrid unit will match the varying load, while storing the surplus energy in the battery.
4. If the battery is fully charged, or if the surplus power is higher than the battery converter rating, the control strategy will autonomously adjust the PV operating point to curtail the PV power generation so that it matches the load.

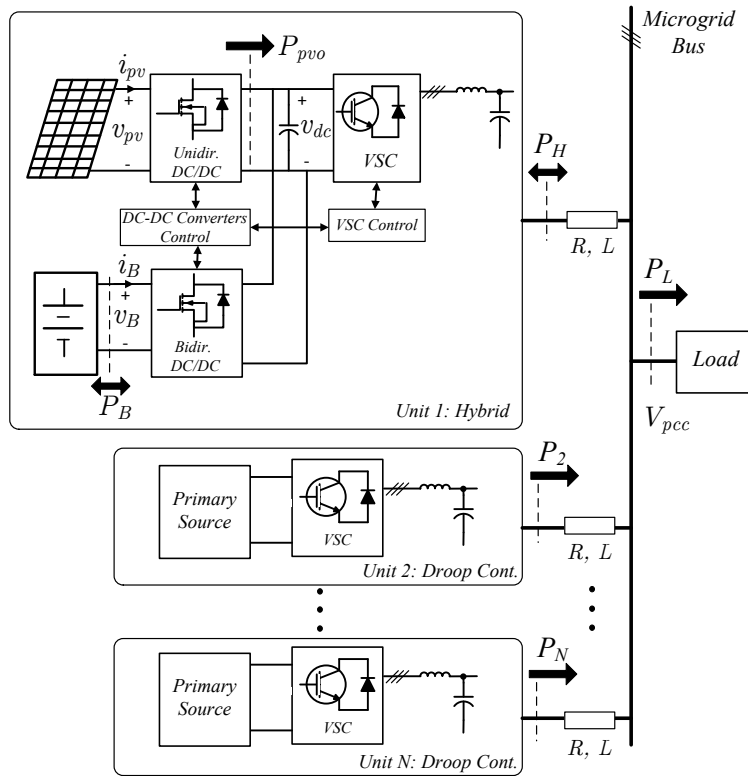


Figure 3.1: Schematic diagram of the PV/battery hybrid system and the microgrid structure.

5. The battery does not supply any power at steady state, unless the load increases beyond the total generation in the microgrid. Therefore, the battery within the hybrid unit can maintain the power balance in the islanded microgrid, similar to any separate battery storage unit.

As in Chapter 2, the power management strategy can be subdivided into two control systems. The first part is the VSC Control System which is in charge of managing the power flow between the hybrid system and the microgrid. It also indirectly coordinates the operation of the PV and the battery to maintain the power balance in the hybrid system. The second is the DC-DC Converters Control System. This part manages the power flow among the PV array, the battery, and the DC-link in order to maintain the power balance within the hybrid system. This is achieved by controlling the DC-DC converters and the PV array voltage reference. In general, the battery DC-DC converter is controlled to regulate the DC-link voltage, while the PV converter is controlled to inject the available PV power into the DC-link.

3.3 VSC Control Strategy

The objective of the VSC control strategy is to coordinate the operation of the hybrid unit with other droop controlled units in the microgrid. The power/frequency (P/f)

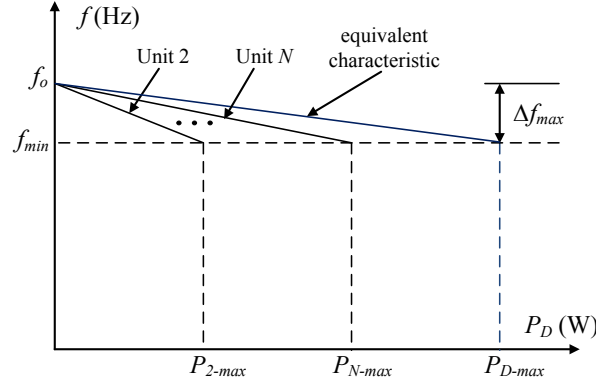


Figure 3.2: Power/frequency characteristics of the droop controlled units, and the equivalent characteristic that represents the combined behavior of the units.

characteristics of these units are illustrated in Fig. 3.2. The equivalent characteristic is the P/f characteristic of a single unit that represents the aggregate behavior of these droop controlled units, with an output power of $P_D = (P_2 + \dots + P_N)$. The power rating of the equivalent unit (P_{D-max}) is the sum of the power ratings of the droop controlled units.

On the other hand, the VSC in the hybrid unit is controlled as a voltage source to regulate the unit output power (P_H) by controlling the frequency of the output voltage, as shown in Fig. 3.3a. The output power (P_H) is indirectly regulated by controlling the battery power (P_B) using the PI controller PI_P . Since the battery DC-DC converter is maintaining the power balance within the hybrid unit by controlling the DC-link voltage, the control error (e_p) at the input of PI_P can be given by

$$\begin{aligned} e_p &= P_{B-ref} - P_B \\ &= P_{B-ref} + (P_{pvo} - P_H) \end{aligned} \quad (3.1)$$

where the power losses are ignored to simplify the discussion [51–57]. Defining P_{ref} as

$$P_{ref} = P_{B-ref} + P_{pvo} \quad (3.2)$$

the control error e_p can be rewritten as

$$e_p = P_{ref} - P_H \quad (3.3)$$

Therefore, regulating P_B at P_{B-ref} is equivalent to regulating the output power (P_H) at the reference P_{ref} . Note that, the controller can be implemented to directly regulate P_H at the reference P_{ref} , which can be generated using the measured P_{pvo} and the reference P_{B-ref} . However, in the case of calculating the reference using the measured P_{pvo} , when the VSC output power is regulated at P_{ref} the losses of the power converters will be supplied by the battery. Therefore, the implementation in Fig. 3.3a is preferred because it inherently takes into account the power converter losses.

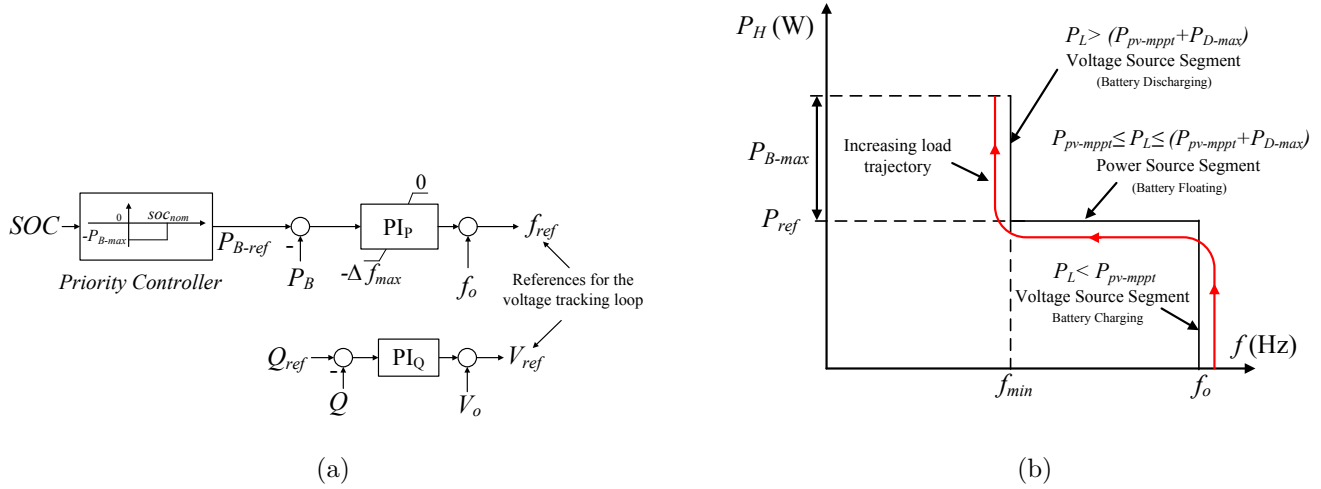


Figure 3.3: Hybrid unit VSC controller and the proposed P/f characteristics of the hybrid unit. (a) Hybrid unit VSC controller. (b) Equivalent power/frequency characteristics of the hybrid unit.

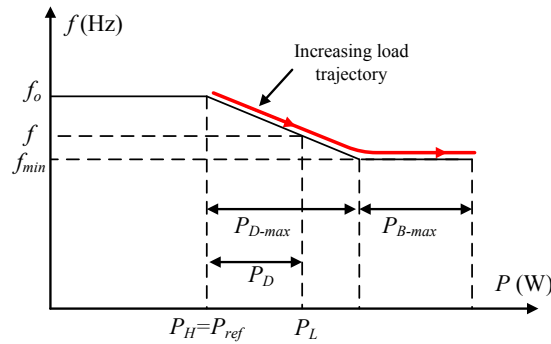


Figure 3.4: Equivalent P/f characteristics of the microgrid, along with the increasing load trajectory

Even though the operating frequency is used to control the power, the frequency range available to control the power is deliberately restricted within the band $[f_{min}, f_o]$, to produce the proposed P/f characteristic of the hybrid unit. The equivalent P/f characteristic of the hybrid unit, as seen by the microgrid, is illustrated in Fig. 3.3b, where P_L is the load demand, P_{B-max} is the maximum power that can be supplied/absorbed by the battery (battery power rating). Note that, since the microgrid operating frequency is regulated by the droop controlled units based on the delivered power (P_D), the operating frequency is considered as the independent variable in Fig. 3.3b. Despite the operating point frequency that changes with P_D , the hybrid unit regulates P_H at P_{ref} . This is achieved by using a PI controller instead of the simple proportional control (droop

control) that is commonly used in grid connected applications where the frequency is fixed by the utility grid side [36, 65]. In other words, the integral control is added to compensate for the change in frequency that is set by the droop controlled units. To gain insight into the coordination of the microgrid units, the P/f characteristics, from Fig. 3.2 and Fig. 3.3b, can be combined into one that describes the P/f characteristics of the whole microgrid, as shown in Fig. 3.4. The shape of the P/f characteristic curve, and the microgrid operating point, are determined by the proposed strategy based on the variables P_L , P_{pvo} , and the battery SOC .

The objective of the VSC controller at any given time is either to charge the battery or to supply all the available PV power to the microgrid. The *Priority Controller* in Fig. 3.3a sets the objective of the control strategy by determining the reference P_{B-ref} based on the battery SOC and the reference SOC_{nom} . The reference SOC_{nom} is the nominal SOC that the controller should always attempt to reach, to ensure that the battery can support the microgrid during peak loads and/or low PV power periods. The control loops are designed so that the objective of the control strategy at any time is set based on two levels of priority, as follows:

- *Level 1*: At this level, the priority of the control strategy is either set to charge the battery or to deliver all the available PV power to the microgrid. The *Priority Controller* decides the objective at this level based on the battery SOC . The implementation of this controller (comparator) is discussed in Section 3.3.2.
- *Level 2*: This level represents the highest priority of the control strategy, which is dedicated to maintaining the power balance in the islanded microgrid, and to prevent the battery SOC and the battery power from exceeding their maximum limits, regardless of the *Level 1* priority.

The reactive power flow is controlled using a PI controller (PI_Q) to follow the reference Q_{ref} [36, 65]. It is worth mentioning that controlling the hybrid unit as a voltage source provides the advantage of using V/Q droop control, which is commonly used in islanded microgrids [66, 70, 74, 76, 77, 92].

To effectively explain the concept of the proposed control strategy, the microgrid operation is divided into two operating scenarios, based on the battery SOC and the control strategy objectives. In both of these scenarios, a maximum power point tracking (MPPT) scheme is activated to track the maximum PV power ($P_{pv-mppt}$); in other words, $P_{pvo} = P_{pv-mppt}$. The details of the control action in these operating scenarios are discussed in the following subsections.

3.3.1 Nominal Operating Scenario

The control strategy operates in this scenario when $SOC \geq SOC_{nom}$. Accordingly, the *Priority Controller* sets the reference P_{B-ref} to zero, and hence, P_{ref} is determined by $P_{pvo} = P_{pv-mppt}$. Therefore, in the nominal operating scenario, the objective is to supply all available PV power to the microgrid.

It is worth emphasizing that the *Priority Controller* has no direct control (closed-loop control) over the battery power (P_B). Instead, the battery power is controlled indirectly

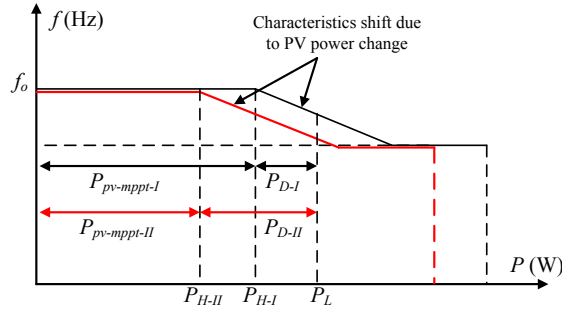


Figure 3.5: P/f characteristics of the microgrid in the Nominal Operating Scenario when the PV power decreases from $P_{pv-mppt-I}$ to $P_{pv-mppt-II}$.

by regulating the power supplied to the microgrid at the reference P_{ref} . This design allows the control strategy to place the highest priority on maintaining the power balance in the microgrid, as will be discussed later in this section. More details on direct charging control will be discussed in Section 3.4.

The system operating point can be on any of the three P/f characteristic segments, depending on the load demand (P_L) and $P_{pv-mppt}$, as in the following three cases:

$$1) P_{pv-mppt} \leq P_L \leq (P_{pv-mppt} + P_{D-max})$$

This case corresponds to the middle segment in Fig. 3.3b and Fig. 3.4, where the hybrid unit supplies all the available PV power to the microgrid ($P_H = P_{pv-mppt}$). The rest of the load is supplied by the droop controlled units, which cooperatively set the operating frequency according to the equivalent droop characteristics (Fig. 3.2), and the supplied power P_D .

Since $P_{pv-mppt}$ depends on the solar irradiance and the temperature, the P/f characteristic in Fig. 3.3b may shift up or down accordingly, which corresponds to shifting the characteristic curve right or left in Fig. 3.4. This effect is shown in Fig. 3.5 where the PV power drops from $P_{pv-mppt-I}$ to $P_{pv-mppt-II}$, causing the output power to drop from P_{H-I} to P_{H-II} , and the whole P/f characteristic to shift to the left. Accordingly, the total output power of the droop controlled units increases from P_{D-I} to P_{D-II} to compensate for the reduction in PV generation, with each unit supplying its share based on its own droop characteristic (Fig. 3.2).

$$2) P_L > (P_{pv-mppt} + P_{D-max})$$

The droop controlled units reduce the frequency in response to any increase in delivered power, while the hybrid unit follows the change in frequency to maintain the output power at $P_{pv-mppt}$. The droop controlled units reach their rated powers at $f = f_{min}$ (see Fig. 3.2). If the load increases and/or the PV power drops such that P_L is greater than the total of $(P_{pv-mppt} + P_{D-max})$, the droop controlled units attempt to reduce the frequency below f_{min} according to their droop characteristics. However, according to the proposed P/f

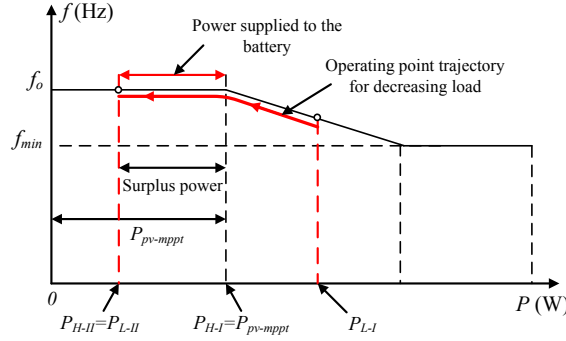


Figure 3.6: P/f operating point trajectory when the load changes from P_{L-I} to P_{L-II} , where $P_{L-II} < P_{pv-mppt}$.

characteristic (see Fig. 3.4), the hybrid unit starts regulating the frequency at f_{min} . This results in regulating the output of the droop controlled units at their rating limits, and in the hybrid unit supplying the deficit in the generation/load balance, while regulating the frequency at f_{min} .

This scenario corresponds to the flat segment of the P/f characteristic at f_{min} in Fig. 3.4, where the operating point transition into this segment is illustrated by the increasing load trajectory. The battery DC-DC converter will supply this extra power (deficit power) from the battery to maintain the DC-link voltage regulated at its nominal value. When the load decreases below $(P_{pv-mppt} + P_{D-max})$, the droop control units increase the frequency above f_{min} . Accordingly, the hybrid unit starts regulating the supplied power P_H at $P_{pv-mppt}$ again.

3) $P_L < P_{pv-mppt}$

According to the earlier discussion, the hybrid unit always attempts to supply all available PV power $P_{pv-mppt}$ to the microgrid, while the droop controlled units match the rest of the load. Therefore, as the load demand decreases, P_D decreases until the point when P_D reaches to zero. At this point, the entire load is being supplied by the hybrid unit ($P_H = P_{pv-mppt} = P_L$) at $f = f_o$. If the load decreases beyond this point, i.e. ($P_L < P_{pv-mppt}$), the droop controlled units try to increase the frequency above f_o to avoid reverse power flow [93]. On the other hand, the hybrid unit still tries to supply $P_{pv-mppt}$ to the microgrid by increasing the frequency too. However, the upper limit of the frequency reference is set to f_o as shown in Fig. 3.3a, and illustrated by the flat segment of the P/f characteristic at f_o in Fig. 3.6. This results in the hybrid unit regulating the frequency at f_o while matching the varying load demand ($P_H = P_L$) autonomously. The surplus power determined by $(P_{pv-mppt} - P_L)$ tends to raise the DC-link voltage; however, since the battery DC-DC converter regulates the DC-link voltage, it will direct the surplus power to the battery. This maintains the power balance in the hybrid unit and also in the whole microgrid. This scenario is illustrated in Fig. 3.6 when the load drops from P_{L-I} to P_{L-II} .

In conclusion, even though the objective is set to supplying all available PV power

to the microgrid, maintaining the power balance is given the highest priority, which is achieved by autonomously matching the load and storing the surplus power.

3.3.2 Battery Charging Scenario

The control strategy operates in this scenario when $SOC < SOC_{nom}$. Therefore, the reference P_{B-ref} is set to $-P_{B-max}$, and accordingly, the power reference P_{ref} is set to $(P_{pv} - P_{B-max})$. The maximum charging power is assumed to be P_{B-max} in this work; however, a different value can be used based on the battery specifications and the design preference.

Using a hard comparator to implement the *Priority Controller* can result in a chattering problem in the reference P_{B-ref} . Instead, a fixed SOC/P_{B-ref} charging curve is used as shown in Fig. 3.7 [29]. The SOC/P_{B-ref} curve is defined by

$$P_{B-ref} = -P_{B-max} + P_{B-max} \left(1 - e^{-\frac{SOC - SOC_{nom} + \delta SOC}{\delta SOC / k_\delta}} \right) \quad (3.4)$$

where the constant k_δ dictates how fast the P_{B-ref} curve approaches zero when the SOC approaches SOC_{nom} . Note that, by choosing $\delta SOC \ll SOC_{nom}$, e.g. $\delta SOC = 0.1\%$ vs. $SOC_{nom} = 65\%$, the curve in Fig. 3.7 operates as a comparator with a soft transition in the reference P_{B-ref} .

The behavior of the proposed control strategy in this scenario is discussed through the following two cases:

$$1) P_{pv-mppt} \geq P_{B-max}$$

In this case, the PV available power is sufficient to charge the battery at P_{B-max} , while the remaining power is supplied to the microgrid. The power supplied to the microgrid (P_H) is determined by the reference P_{ref} , i.e., by the difference $(P_{pv-mppt} - P_{B-max})$. When the VSC supplies this power to the microgrid, the battery DC-DC converter injects the remaining PV power (P_{B-max}) into the battery, to regulate the DC-link voltage. Therefore, charging the battery is indirectly achieved by controlling the power supplied to the microgrid.

Even though the objective of the control strategy during this operating scenario is to charge the battery, maintaining the power balance in the microgrid is still given the highest priority. The transition in the operating point and the P/f characteristics, to maintain the power balance in the microgrid while charging the battery, is illustrated in Fig. 3.8, and described in the following steps:

- Initially, the battery is being charged solely by the PV power with $P_{B-I} = P_{B-max}$, whereas the remaining PV power is supplied to the microgrid to cover part of the load demand P_{L-I} . The rest of the load is supplied by the droop controlled units according to the equivalent droop characteristic which determines the operating point A.
- The droop controlled units continue to supply any increase in the load demand until they reach their ratings at f_{min} (point B).

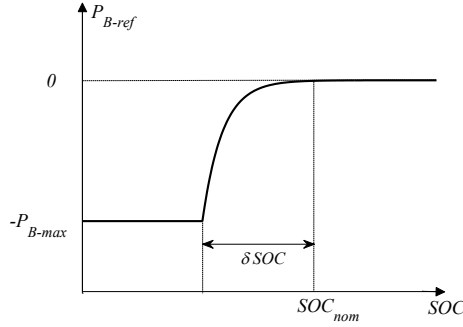


Figure 3.7: SOC/P_{B-ref} characteristic curve of the *Priority Controller*.

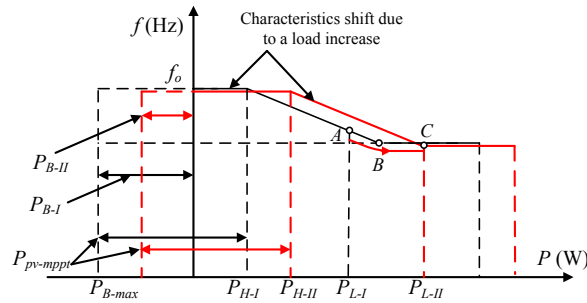


Figure 3.8: P/f characteristic illustrating the *Battery Charging Scenario* when $P_{pv-mppt} \geq P_{B-max}$, and when the load increases.

- If the load increases beyond point B , e.g., to P_{L-II} (point C), the droop controlled units will attempt to decrease the operating frequency below f_{min} . However, as explained earlier, the hybrid unit starts regulating the frequency at f_{min} . This results in regulating the output of the droop controlled units at their ratings, while the increase in the load is supplied by the hybrid unit. The increase in the hybrid unit output from P_{H-I} to P_{H-II} , is equivalent to shifting the P/f characteristic curve to the right as shown in Fig. 3.8. Accordingly the charging power is reduced by the battery DC-DC converter to P_{B-II} in order to regulate the DC link voltage.
- The hybrid unit continues to supply any increase in the load from the PV, until it supplies all the available PV power, i.e. $P_H = P_{pv-mppt}$. In this case, the charging power is reduced to zero. Any further increase in the load demand will be met by the battery to maintain the power balance in the microgrid as in the Nominal Operating Scenario (see Fig. 3.4).

In conclusion, even though the objective in this scenario is to charge the battery, the control strategy still places higher priority on maintaining the power balance in the microgrid by meeting the increasing load demand.

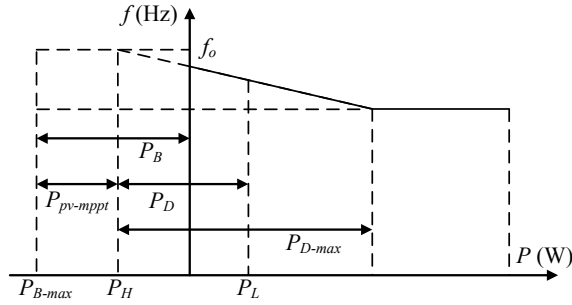


Figure 3.9: P/f characteristic during the Battery Charging Scenario when $P_{pv-mppt} < P_{B-max}$.

2) $P_{pv-mppt} < P_{B-max}$

In this case, P_{ref} is negative and the hybrid unit absorbs the power difference ($P_{pv-mppt} - P_{B-max}$) to support charging the battery at P_{B-max} . This is equivalent to shifting the P/f characteristic to the left resulting in the characteristic of Fig. 3.9. Under this condition, the hybrid unit is seen as part of the load demand by the droop controlled units.

The droop controlled units continue to support the battery charging and supply any increase in the load until they reach their ratings. Any increase in the load beyond this point will cause the P/f characteristic to shift to the right similar to the previous case illustrated in Fig. 3.8.

3.4 DC-DC Converters Control System

In both operating scenarios discussed earlier in Section 3.3, the PV converter extracts and injects all the available PV power ($P_{pv-mppt}$) into the DC-link, whereas the DC-link voltage is regulated by the battery DC-DC converter. In those scenarios, the PV voltage reference (v_{pv-ref}) is determined solely by the MPPT algorithm.

Two operational cases have not been considered yet in the aforementioned scenarios. These cases are discussed below:

- *Case 1:* The SOC may increase beyond the maximum preset SOC limit of the battery (SOC_{max}), while the hybrid unit is attempting to store the surplus PV power in the battery, in order to maintain the power balance in the microgrid. This may occur during the Nominal Operating Scenario when $P_L < P_{pv-mppt}$.
- *Case 2:* This case occurs when the surplus PV power is larger than the battery power rating P_{B-max} . This can only happen if the battery and its converter ratings are chosen to be less than the PV power rating. Moreover, in practice, the charging power is commonly reduced when the SOC approaches its maximum limit SOC_{max} , to avoid battery voltage excursions [29, 87].

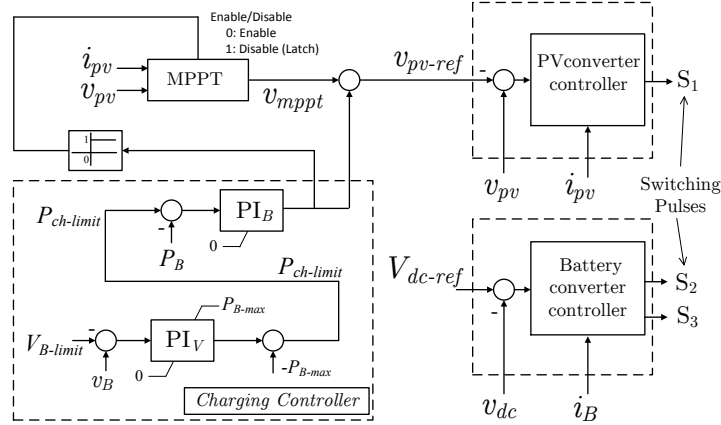


Figure 3.10: Control system for the DC-DC converters.

Accordingly, a dedicated controller is required to ensure controlled charging. One option is to use a simple two-stage charging control, a constant current/power stage followed by a constant voltage stage. Since the main focus of this paper is on the coordination of the hybrid unit in the microgrid, the two-stage charging is considered adequate for validating the proposed power management strategy. Moreover, the control strategy is able to incorporate different charging curves that may use the battery *SOC* or voltage to set the charging power reference [87–91].

However, since the power available to charge the battery varies based on the varying PV power and the load, the proposed controller is used here only to set the charging power limit ($P_{ch-limit}$) based on the battery voltage, as can be seen in Fig. 3.10. The inner P_B control loop, shown in Fig. 3.10, is introduced to limit the charging power from exceeding $P_{ch-limit}$ at any time.

When the voltage is lower than the set voltage limit $V_{B-limit}$, the output of the controller PI_V is saturated at zero and, hence $P_{ch-limit}$ is set to $-P_{B-max}$. The controller continues operating in this constant power stage, until the battery voltage goes beyond $V_{B-limit}$. At this point, the controller PI_V starts reducing the charging power reference $P_{ch-limit}$ to regulate the battery voltage while charging the battery at a reduced rate.

If the charging power is less than the reference $|P_{ch-limit}|$, the output of the controller PI_B remains zero, and therefore, the battery continues charging at the same rate. If the load decreases and/or V_B increases such that $|P_B|$ is higher than the reference $|P_{ch-limit}|$, the controller PI_B starts adjusting the PV voltage so that the charging power follows the reference $P_{ch-limit}$. In other words, the charging reference sets the upper limit for the charging power.

The charging controller moves the PV operating point away from the maximum power point (MPP) (see Fig. 3.11), into the voltage source region of the PV characteristic curve, to curtail the PV power, until P_B settles at P_{B-ref} . During this control action, the MPPT algorithm is disabled and the voltage v_{mpppt} is held at the most recent MPP voltage. The output of PI_B is used here to disable the MPPT scheme using the logic shown in Fig. 3.10.

The PI_B control loop continues adjusting the PV operating point so that the PV power

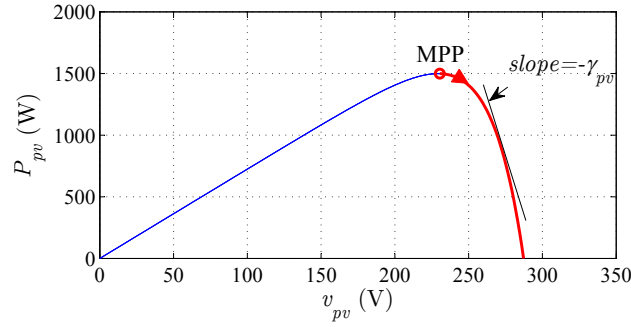


Figure 3.11: PV power characteristics (Irradiance=1000 W/m², T=25C^o) showing the MPP and the PI_B control region.

autonomously matches the varying load demand and the charging power combined, as explained in the following:

1. Initially, the controller PI_B can only curtail the PV power by adjusting the PV operating point in one direction as shown in Fig. 3.11, which is achieved using the chosen saturation limits. Once the controller starts operating such that $P_B = P_{ch-limit}$, the PI_B output settles at a positive value due to the integral action. Accordingly, this gives the controller the freedom to adjust the operating point in both directions, reducing the PV power and, also, increasing the PV power up to the $P_{pv-mppt}$ limit.
2. If $|P_B|$ drops below $|P_{ch-limit}|$, due to an increase in demand for example, PI_B starts decreasing the PV voltage reference. This results in moving the operating point towards the MPP (increasing the PV power) until $P_B = P_{ch-limit}$ and the increase in the PV power matches the increase in the load demand. Similarly, if $|P_B|$ increases above $|P_{ch-limit}|$, the controller increases the PV voltage which moves the operating point further from the MPP. In both cases, the hybrid unit matches the change in the load demand using the PV power.

During the above control action, the hybrid unit continues operating in the same operating scenario (Nominal or Battery Charging Scenario), however with reduced PV power output.

When the load demand increases and/or the PV power drops, the controller moves the PV operating point towards the MPP until the PI_B output is reduced to zero. Consequently, the MPPT scheme is activated again, and hence, $P_{pvo} = P_{pv-mppt}$. Any increase in the load demand beyond this point will be supplied by the droop controlled units as explained in Section 3.3.

3.5 Small-Signal Model of the Proposed Control Loops

Modeling and control designs of the voltage controllers for the DC-DC converters and VSCs are well established in the literature. As in Chapter 2, the voltage controllers for the DC-DC converters are designed in this work as in [50], while the voltage control

loops for the VSCs are designed as in [14]. The structures and the parameters of these controllers are presented in Appendix A.

Therefore, the focus of this section is only on the real/reactive control loops, and the battery charging loop (P_B control loop), to gain insight into the dynamics and the control design of these loops.

3.5.1 Real/Reactive Control Loops

The real and reactive power flows at the output of the hybrid unit are described as follows [94]:

$$P_H = \frac{(RV^2 - RVV_{pcc} \cos \delta + XVV_{pcc} \sin \delta)}{R^2 + X^2} \quad (3.5)$$

$$Q_H = \frac{(XV^2 - XVV_{pcc} \cos \delta - RVV_{pcc} \sin \delta)}{R^2 + X^2} \quad (3.6)$$

where R and X are the resistive and inductive components of the feeder impedance, δ is the power angle, V is the unit output voltage, and V_{pcc} is the microgrid bus voltage. The real and reactive power controllers equations, taking into account the low-pass filters in the measurement channels, are given by

$$\omega = \omega_o + \frac{K_{p-p}s + K_{i-p}}{s} (P_{B-ref} - \frac{1}{T_s + 1} (P_{pvo} - P_H)) \quad (3.7)$$

$$V = V_o + \frac{K_{p-q}s + K_{i-q}}{s} (Q_{ref} - \frac{1}{T_s + 1} Q_H) \quad (3.8)$$

where V and ω are the output voltage and angular frequency, V_o and ω_o are the nominal voltage and angular frequency, K_{p-p} and K_{i-p} are the proportional and integral gains of the real power controller (PI_P), K_{p-q} and K_{i-q} are the proportional and integral gains of the reactive power controller (PI_Q). Linearizing (6.8), (6.9), (3.7), and (3.8) around an operating point

$$\begin{aligned} \Delta P_H &= \left(\frac{\partial P_H}{\partial V}\right) \Delta V + \left(\frac{\partial P_H}{\partial \delta}\right) \Delta \delta \\ &= K_{pv} \Delta V + K_{p\delta} \Delta \delta \end{aligned} \quad (3.9)$$

$$\begin{aligned} \Delta Q_H &= \left(\frac{\partial Q_H}{\partial V}\right) \Delta V + \left(\frac{\partial Q_H}{\partial \delta}\right) \Delta \delta \\ &= K_{qv} \Delta V + K_{q\delta} \Delta \delta \end{aligned} \quad (3.10)$$

$$\Delta \omega = -\frac{K_{p-p}s + K_{i-p}}{s(T_s + 1)} \Delta P_H \quad (3.11)$$

$$\Delta V = -\frac{K_{p-q}s + K_{i-q}}{s(Ts + 1)}\Delta Q_H = G_v(s)\Delta Q_H \quad (3.12)$$

where K_{pv} , $K_{p\delta}$, K_{qv} , and $K_{q\delta}$ are evaluated at the considered operating point. Considering that $\Delta\omega = s\Delta\delta$, (3.11) can be rewritten as

$$\Delta\delta = -\frac{K_{p-p}s + K_{i-p}}{s^2(Ts + 1)}\Delta P_H = G_\delta(s)\Delta P_H \quad (3.13)$$

Substituting for ΔP_H from (3.13) in (3.9), $\Delta\delta$ is given by

$$\Delta\delta = \frac{G_\delta(s)K_{pv}}{1 - K_{p\delta}G_\delta(s)}\Delta V = G_{\delta v}(s)\Delta V \quad (3.14)$$

Substituting for ΔQ_H from (3.12) in (3.10), ΔV can be given by

$$\Delta V = \frac{G_v(s)K_{q\delta}}{1 - K_{qv}G_v(s)}\Delta\delta = G_{v\delta}(s)\Delta\delta \quad (3.15)$$

Using (3.14) and (3.15), the characteristic equation can be written as:

$$1 - G_{\delta v}(s)G_{v\delta}(s) = 0 \quad (3.16)$$

Substituting for $G_{\delta v}(s)$ and $G_{v\delta}(s)$ from (3.14) and (3.15), the characteristic equation can be written as follows:

$$a_5s^5 + a_4s^4 + a_3s^3 + a_2s^2 + a_1s + a_0 = 0 \quad (3.17)$$

where

$$a_5 = T^2 \quad (3.18)$$

$$a_4 = 2T + TK_{qv}K_{p-q} \quad (3.19)$$

$$a_3 = 1 + TK_{qv}K_{i-q} + K_{qv}K_{p-q} + TK_{p\delta}K_{p-p} \quad (3.20)$$

$$a_2 = K_{qv}K_{i-q} + K_{p\delta}K_{p-p} + K_{p\delta}K_{p-p}K_{qv}K_{p-q} + TK_{p\delta}K_{i-p} - K_{pv}K_{p-p}K_{q\delta}K_{p-q} \quad (3.21)$$

$$a_1 = K_{p\delta}K_{p-p}K_{qv}K_{i-q} + K_{p\delta}K_{i-p} + K_{p\delta}K_{i-p}K_{qv}K_{p-q} - K_{pv}K_{p-p}K_{q\delta}K_{i-q} - K_{pv}K_{i-p}K_{q\delta}K_{p-q} \quad (3.22)$$

$$a_0 = K_{p\delta}K_{i-p}K_{qv}K_{i-q} - K_{pv}K_{i-p}K_{q\delta}K_{i-q} \quad (3.23)$$

Root trajectories considering the system parameters in Table 3.1 are shown in Fig. 3.12a, when the gain K_{i-p} is varied from 0.01 to 0.07 with a step of 0.005 rad/(W·s²), and $K_{p-p} = 2\pi \times 0.0005$ rad/(W·s). The zoomed-in view of the encircled root trajectory is shown Fig. 3.12b, which shows that the effect of the gain K_{i-p} on the position of this pole is insignificant. The position of this pole is mainly determined by the integral gain of PI_Q.

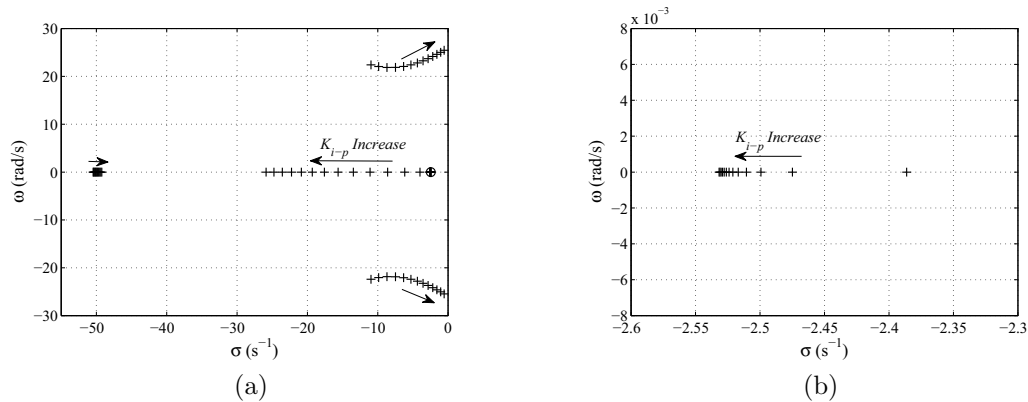


Figure 3.12: Root trajectories of the real/reactive control loops when the gain K_{i-p} changes from 0.01 to 0.07 with a step of 0.005 rad/(W·s²). (a) All the roots trajectories. (b) Zoomed in view of the least sensitive trajectory.

Table 3.1: System Parameters

Description	Parameter	Value
Nominal frequency	f_o	60 Hz
Hybrid Unit (Unit 1) Power Rating	P_{H-max}	2500 W
Droop Controlled Unit Rating	P_{D-max}	1000 W
Frequency Droop Limit	Δf_{max}	0.25 Hz
Nominal DC-link Voltage	V_{dc-ref}	400 V
Nominal Battery Voltage	V_B	156 V
Battery Capacity	C_{bat}	32 Ah
Battery Converter Rating	P_{B-max}	1000 W
PV Open Circuit Voltage	V_{oc}	287 V
PV Short Circuit Current	I_{sc}	7.25 A
PV Array Power Rating	P_{pv-max}	1.5 kW
Feeder Inductance	L	4 mH
Feeder Resistance	R	1.1 Ω
PI _P Controller Gains	K_{p-p}	0.0005 Hz/W
	K_{i-p}	0.005 Hz/(W·s)
PI _Q Controller Gains	K_{p-q}	0.01 V/var
	K_{i-q}	0.5 V/(var·s)
PI _B Controller Gains	K_{p-B}	0 V/W
	K_{i-B}	0.6022 V/(W·s)

3.5.2 Charging Control Loop

The dynamics of the battery SOC , and hence voltage, are considerably slower in comparison to those of the control loops of the DC-DC converters and the VSC. Therefore, the set-point $P_{ch-limit}$ can be considered as an independent reference.

On the other hand, the P_B control loop can be designed to have slower dynamics than those of the DC-DC converters, to avoid interaction with the inner voltage control loops of these converters, which is a common practice in designing multi-loop control systems. In other words, the closed-loop of the DC-DC converters can be represented as unity gains in the considered bandwidth range of the outer P_B control loop, as will be discussed next.

Accordingly, the approximated model of the P_B control loop is developed as shown in Fig. 3.13a. The transfer functions G_{pv} and G_B represent the dynamics of the PV and the battery control loops, while $f(v_{pv})$ represents the P_{pv}/v_{pv} characteristic curve (Fig. 3.11), which is a nonlinear function. This function can be approximated by a straight line in the PV characteristic region under consideration as illustrated in Fig. 3.11, where $-\gamma_{pv}$ indicates the slope of the line. Considering the linearized PV characteristic curve, and that G_{pv} and G_B are approximated by unity gains in the loop bandwidth under consideration, the linearized model of the charging loop is illustrated in Fig. 3.13b. \bar{P}_{pv} and P_{Ho} represent the PV power and the load power, supplied by the hybrid unit, at the considered operating point. Accordingly, the open-loop transfer function can be given by

$$G_{B-ol} = \frac{K_{p-B}s + K_{i-B}}{s} \gamma_{pv} \quad (3.24)$$

where K_{p-B} and K_{i-B} are the proportional and integral gains of the controller PI_B . By setting $K_{p-B} = 0$, the closed-loop results in a first order transfer function as follows:

$$G_{B-cl} = \frac{1}{T_{ch}s + 1} \quad (3.25)$$

where

$$T_{ch} = \frac{1}{K_{i-B}\gamma_{pv}} \quad (3.26)$$

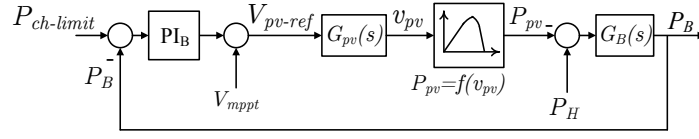
In conclusion, a simple integral controller can be used in the charging control loop. The gain K_{i-B} is chosen so that the P_B control loop is 10-15 times slower than the inner control loops. The voltage control loops (inner loops) are designed as in [50], which results in closed-loop cross-over frequencies of 271 rad/s and 471 rad/s for the battery and the PV controllers, respectively. Considering the nominal PV characteristics in Fig. 3.11 where $\gamma_{pv} = 45$ W/V, choosing K_{i-B} as 0.6022 results in $1/T_{ch} = 27.1$ rad/s, which is one tenth of the bandwidth of the slowest inner loop (271 rad/s).

Consequently, the outer voltage control loop can be modeled as in Fig. 3.14. The transfer function G_{Bv} is used to describe the behavior of the battery voltage around the maximum voltage limit ($V_{B-limit}$) operating region. To gain insight into the behavior of the battery in this operating region, the experimental results in Fig. 3.15 show the battery voltage excursions beyond the maximum limit $V_{B-limit}$ of 185 V, when the battery is being charged at a constant rate (P_{Bo}) of 780 W at high SOC levels ($SOC > 90\%$).

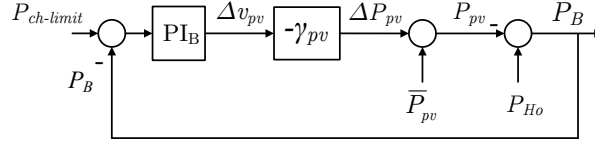
The battery voltage behavior can be approximated by two lines in the considered operating region as shown in Fig. 3.15. Accordingly, the transfer function G_{Bv} can be approximated by an integrator as below

$$G_{Bv} = \frac{K_{Bv}}{s} \quad (3.27)$$

where the constant K_{Bv} has two different values which correspond to the different operating segments represented by the slopes S_1 and S_2 . Considering the battery voltage



(a)



(b)

Figure 3.13: Approximated model of the P_B Control Loop. (a) Nonlinear model. (b) Linearized model.

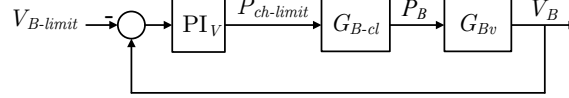


Figure 3.14: Approximated model of the charging control loop.

behavior in Fig. 3.15, K_{Bv} can be approximated by two values, $K_{Bv1} = 5.38 \times 10^{-5}$ V/(s·W) and $K_{Bv2} = 1.129 \times 10^{-3}$ V/(s·W), corresponding to S_1/P_{Bo} and S_2/P_{Bo} .

Note that, when the charging power changes, the slopes S_1 and S_2 will change, since they represent the change in voltage vs. time (V/s) at a certain charging power. However, the gains K_{Bv1} and K_{Bv2} can still approximate the battery behavior since they represent the change in voltage vs. charging power and time (V/s·W). For a more accurate approximation, a specific set of charging curves can be used to calculate the gains K_{Bv1} and K_{Bv2} for a specific set of charging rates.

From Fig. 3.14, the characteristic equation of the closed-loop system is given by

$$T_{ch}s^3 + s^2 + K_{p-ch}K_{Bv}s + K_{i-ch}K_{Bv} = 0 \quad (3.28)$$

where K_{p-ch} and K_{i-ch} are the proportional and the integral gains of the controller PI_V . Considering that $K_{Bv} = K_{Bv2}$ and $K_{p-ch} = 100$, while varying K_{i-ch} from 2 to 100 with a step of 0.25, the dominant root trajectories are shown in Fig. 3.16.

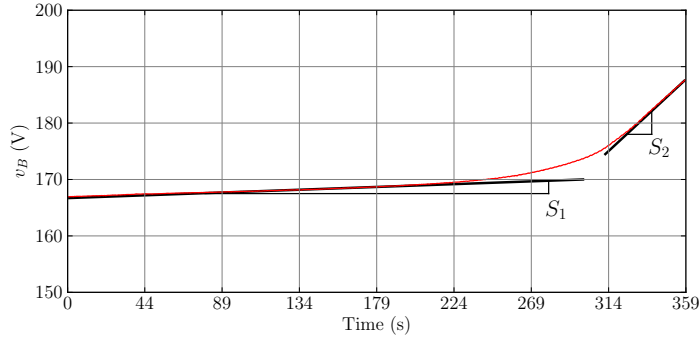


Figure 3.15: Experimental results illustrating the battery voltage excursion beyond $V_{B-limit}$ during unconstrained constant power charging.

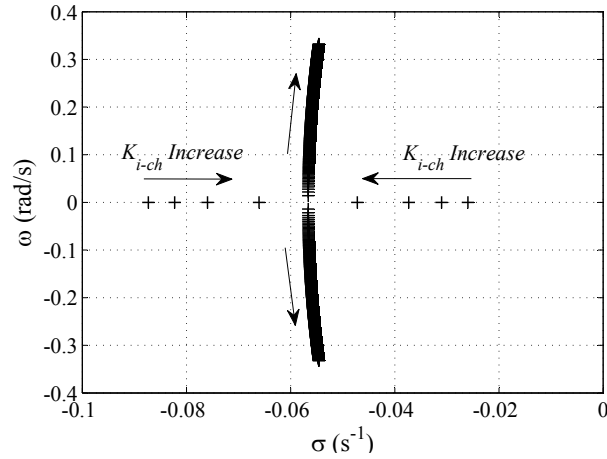


Figure 3.16: Dominant root trajectories of the charging control loop when the gain K_{i-ch} is varied from 2 to 100 with a step of 0.25.

3.6 Experimental Evaluation

3.6.1 Experimental Setup

The power management strategy is evaluated experimentally on the two-unit prototype microgrid presented in Chapter 2. Unit 1 is the hybrid unit, while Unit 2 represents the equivalent of the droop controlled units with a combined output power of P_D . The PV array is emulated using a commercial PV simulator from Chroma. Both units are connected to a 3-phase microgrid bus, which is connected to a programmable load bank. The key parameters of the experimental system are shown in Table 3.1. The hybrid unit is configured as in Fig. 3.1, with MOSFET-based boost and synchronous boost topologies used for the unidirectional and bidirectional converters, respectively. The experimental data collection programs are written in Python and run on a Ubuntu Linux platform, which is connected to the microcontrollers using Texas Instruments Ethernet-to-serial converters.

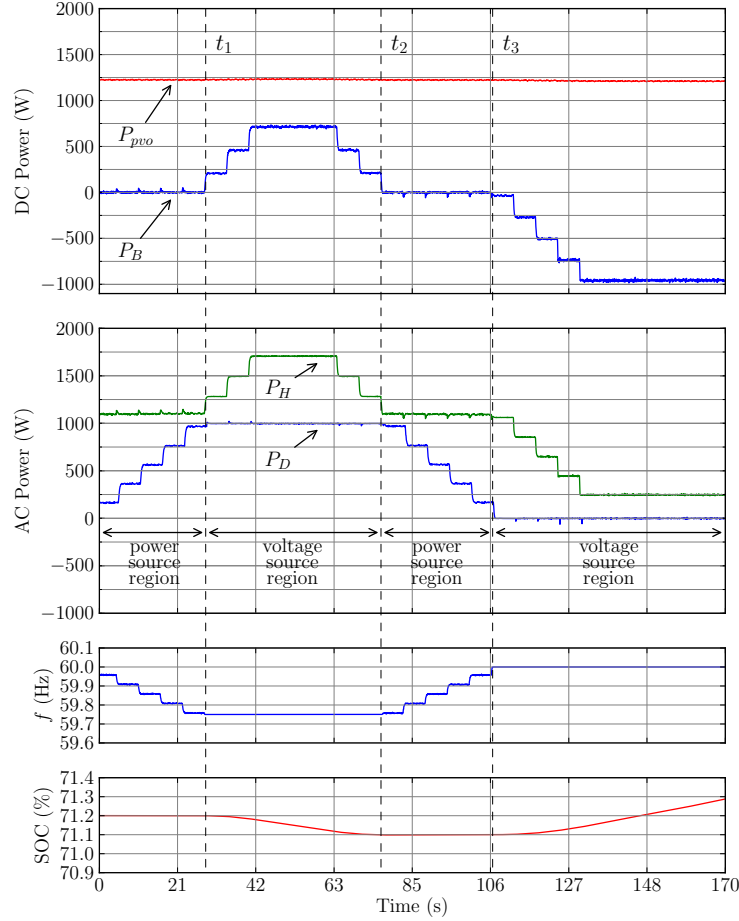


Figure 3.17: Experimental performance of the proposed strategy during the nominal operating scenario in response to load changes.

3.6.2 Experimental Results

The performance of the proposed strategy is validated through experiments under the nominal scenario with changes in both load and generation, and under the charging scenario. Additional experiments show the transition between the scenarios and the action of the charging control loop.

Nominal Scenario

Performance of the proposed strategy during the nominal operating scenario in response to load changes is illustrated in Fig. 3.17. During this scenario, the SOC is higher than SOC_{nom} , which is set to 65%. To effectively illustrate the performance, the system behavior is divided into four regions.

Between $t = 0$ and $t = t_1$, the hybrid unit delivers all available PV power to the microgrid by regulating the battery power at $P_B = 0$ W. Therefore, the hybrid unit appears in the microgrid as a power controlled source. On the other hand, the increasing

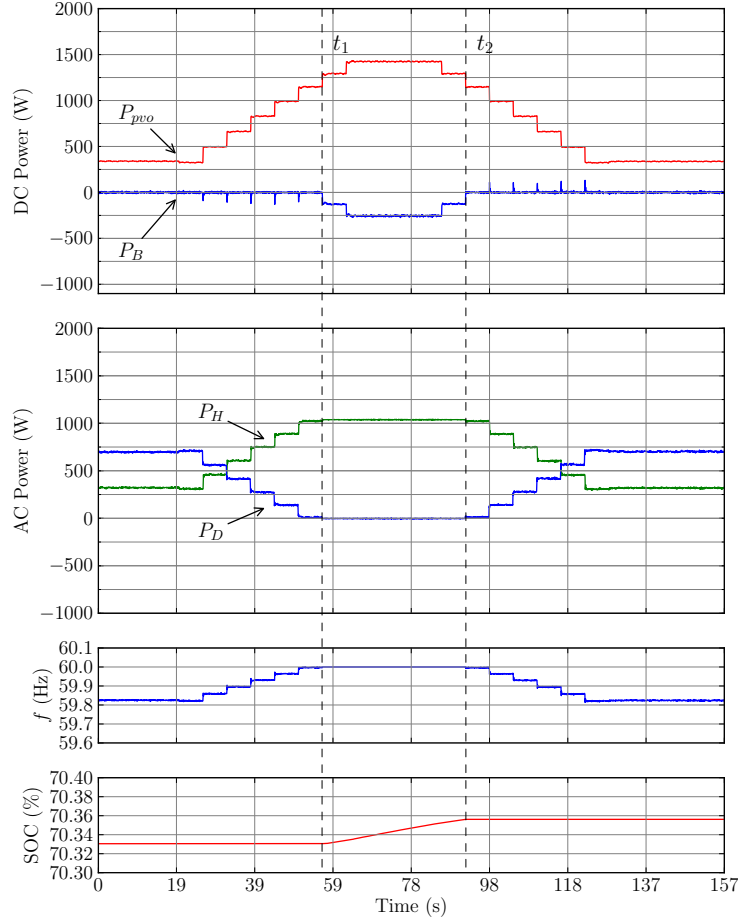


Figure 3.18: Experimental results of the proposed strategy during the nominal operating scenario in response to PV power changes.

load demand is met by the droop controlled unit. This results in dropping the frequency in response to the increasing load. The droop controlled unit continues to supply the increasing load demand until it reaches its maximum power rating of 1000 W at $t = t_1$. At this point the frequency reaches its minimum limit of f_{min} , i.e. 59.75 Hz.

From $t = t_1$ to $t = t_2$, the load increases beyond the power available from the PV and the droop controlled unit combined, i.e. ($P_L > P_{pv-mppt} + P_{D-max}$). As discussed in Section 3.3.1 and illustrated by the microgrid P/f characteristics (see Fig. 3.4), the hybrid unit starts regulating the operating frequency at f_{min} , which results in limiting the P_D at P_{D-max} . Consequently, the hybrid unit operates as a voltage source, and therefore matches the varying load by supplying the deficit power from the battery, resulting in a drop in the SOC .

At $t = t_2$, the load demand drops below the total of ($P_{pv-mppt} + P_{D-max}$), and therefore the hybrid unit returns to operating as a power controlled source, while the droop controlled unit supplies the rest of the load.

The load demand continues to drop until $P_D = 0$ W at $t = t_3$. For $t \geq t_3$, the load decreases below the available PV power, i.e. $P_L < P_{pv-mppt}$. Consequently, as

discussed in Section 3.3.1 (see Fig. 3.6), the hybrid unit autonomously starts acting as a voltage source, while regulating the frequency at $f = f_o$ and matching the available load demand in the microgrid. As can be seen in Fig. 3.17, the surplus power from the PV is absorbed by the battery to maintain the power balance in the hybrid unit and, also, in the microgrid.

Performance of the strategy in response to PV power variations is illustrated in Fig. 3.18. In this experiment, the load is kept constant around 1000 W, and the PV power is varied by changing the irradiance setting in the PV simulator from 200 W/m² to 1000 W/m².

Between $t = 0$ and $t = t_1$, it is shown in Fig. 3.18 that the hybrid unit tracks and supplies all the available PV power to the microgrid while regulating the battery power at $P_{B-ref} = 0$ W, as explained in Section 3.3.1. Since the load demand is kept constant, the output power from the droop controlled unit is reduced in response to the increasing power from the hybrid unit, which operates as a power controlled source in this period. The output power P_H continues to increase with increasing PV power until it supplies all the load, and P_D reduces to zero.

The increase in the PV power beyond this limit (for $t \geq t_1$) results in the controller PI_P (see Fig. 3.3a) saturating at $f = f_o$. This causes the hybrid unit to behave as a voltage source and therefore matches the load demand. This shows how the highest priority of maintaining the power balance in the microgrid is achieved by the control strategy autonomously. Consequently, the surplus PV power is absorbed by the battery, through the DC-DC converter which is responsible for regulating the DC-link voltage. The battery continues to store the surplus energy until the PV power drops below the load demand.

Charging Scenario

The performance of the proposed strategy during the charging operating scenario is illustrated in Fig. 3.19. In this scenario, the objective is to charge the battery at P_{B-max} (-1000 W). Since the available PV power is less than P_{B-max} , the rest of the charging power and the losses is imported from the microgrid. In this case, the hybrid unit appears as a load in the microgrid, which is equivalent to shifting the P/f characteristics to the left as explained in Section 3.3.2 (see Fig. 3.9).

When the load starts increasing at $t = t_1$, the droop controlled unit starts supplying the increased load demand, while the battery is still being charged at its maximum rating, until P_D reaches P_{D-max} at $t = t_2$. As the load increases beyond this point, the hybrid unit starts regulating the frequency at f_{min} , due to the chosen limit of the controller PI_P output. This results in limiting the output of the droop controlled units at their rated powers, while reducing the power flow into the hybrid unit until $P_H = 0$ W. This happens because the hybrid unit operates as a voltage controlled source that regulates the frequency. On the other hand, the output powers of the droop controlled units are regulated at their ratings, i.e. they start operating as power controlled sources.

Any increase in the load demand beyond this point will be supplied by the hybrid unit as the P/f characteristic continues to shift to the right, until all the PV power is being delivered to the load, which happens at $t = t_3$. At this moment, the P/f characteristic

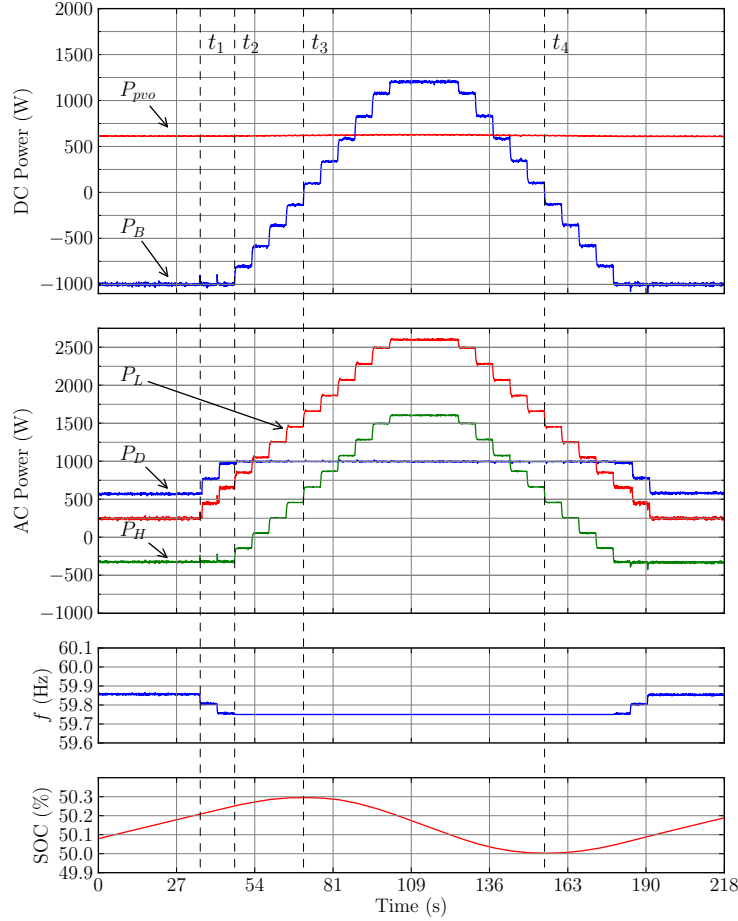


Figure 3.19: Experimental results of the proposed strategy during the charging operating scenario.

curve will resemble the one in Fig. 3.4. Any further increase in the load will be supplied by the battery as discussed in Section 3.3.1.

The control strategy resumes charging the battery after the load demand drops below the total generation as shown in Fig. 3.19 for $t > t_4$.

Transition between Operating Scenarios

The performance of the proposed strategy during a transition from the charging scenario to the nominal operating scenario is illustrated in Fig. 3.20. In this experiment, δSOC is set to 0.1%, while SOC_{nom} is set to 65%.

Initially, the system is operating in the charging scenario while the battery is being charged at its maximum rating. The SOC continues increasing until it reaches the limit of $(SOC_{nom} - \delta SOC)$, i.e. 64.9% at $t = t_1$. At this moment, the charging priority controller starts reducing the reference P_{B-ref} exponentially as a function of the rising SOC (see Fig. 3.7). As can be seen in Fig. 3.20, the charging power is reduced and, consequently, the hybrid unit output P_H increases until all the available PV power is delivered to the

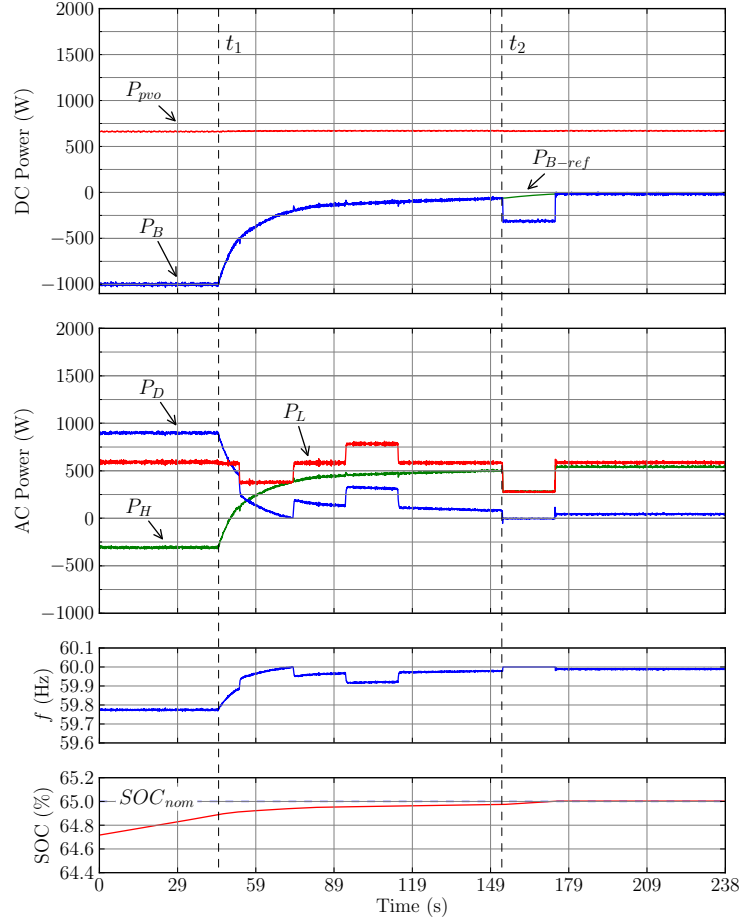


Figure 3.20: Experimental results of the proposed strategy during a transition from the charging scenario to the nominal operating scenario.

microgrid.

Moreover, the load P_L is stepped up and down several times to examine the performance of the power control loop during the transition phase, in response to load disturbances. As shown in Fig. 3.20, the hybrid unit continues to operate as a power controlled source until $t = t_2$. At this point, the load demand is dropped below the supplied PV power and, therefore, the hybrid unit autonomously starts to operate as a voltage source to match the available load demand while regulating the frequency at f_o .

Performance of the Charging Control Loop

The performance of the battery voltage and charging control loops is validated through experiments. The results are shown in Fig. 3.21. Initially, the load is less than 200 W, while the available PV power is 1000 W, which forces the hybrid unit to operate as a voltage source to match the available load demand. In this case, the battery is used to store the surplus PV power in order to maintain the power balance in the microgrid. The battery is charged continuously until a voltage excursion occurs at $t = t_1$, when the

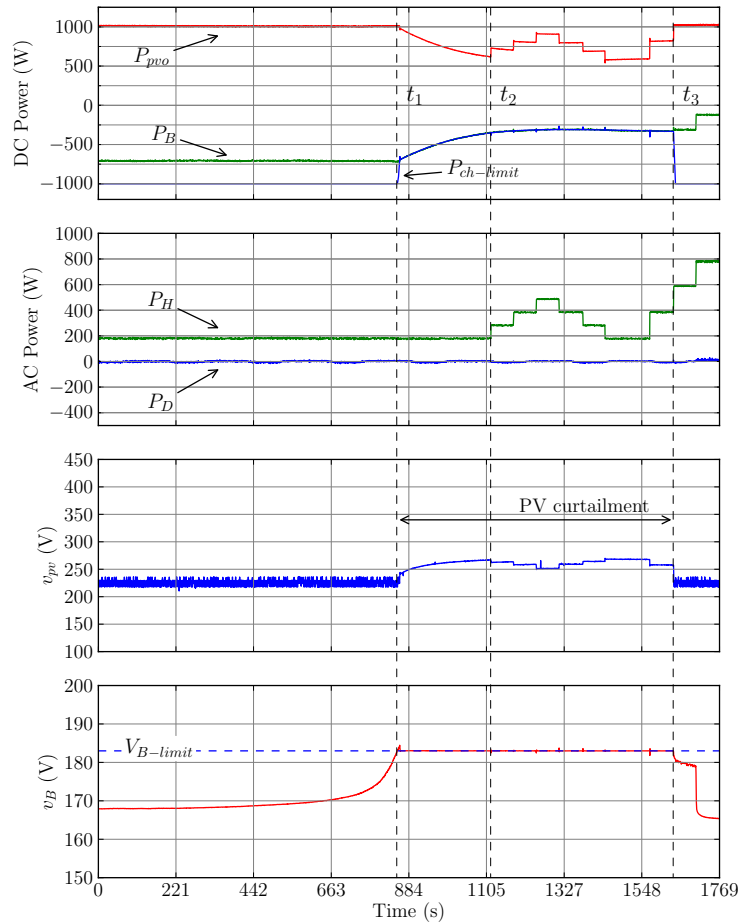


Figure 3.21: Experimental results showing the action of the proposed charging controller.

voltage starts to exceed the maximum voltage limit of the battery $V_{B-limit}$. This indicates that the battery can no longer be charged at the current rate.

Accordingly, the controller PI_V (see Fig. 3.10) starts reducing the charging limit reference $P_{ch-limit}$ at $t = t_1$. Once the charging limit becomes less than charging power, the controller PI_B starts reducing the PV power output so that P_B matches $P_{ch-limit}$. As shown in Fig. 3.21, the control loop disables the MPPT algorithm and starts increasing the PV voltage to move the PV operating point to the right of the MPP on the PV curve.

To examine the performance of the proposed strategy in the event of load changes, the load is stepped up and down several times starting at $t = t_2$. The results show that the control strategy can successfully adjust the PV operating point autonomously so that the PV power matches the varying load, while regulating the battery voltage at its limit. At $t = t_3$, the load demand increase forces the PV operating point to move back to the MPP while enabling the MPPT algorithm again.

3.7 Summery and Conclusion

In this chapter, a power management strategy that enables controlling a PV/battery unit as a voltage source in an islanded microgrid is proposed. In contrast to the common way of controlling the PV unit as a current source in the literature, it is shown that controlling the hybrid unit as a voltage source that follows the proposed adaptive power/frequency characteristics, can achieve decentralized control of the hybrid unit in the islanded microgrid without relying on a central EMS and communications. This strategy eliminates the operational limitations of former technique that presented in Chapter 2. It is demonstrated experimentally that the proposed power/frequency characteristics can adapt autonomously to the microgrid operating conditions so that the hybrid unit could supply the maximum PV power, match the load, and/or charge the battery, while maintaining the power balance in the microgrid and respecting the battery *SOC* limits. Also, small-signal stability of the proposed control loops is investigated to gain insight into the dynamic behavior of these loops.

Strategies for Independent Deployment and Autonomous Control of PV and Battery Units in Islanded Microgrids

4.1 Introduction

In this chapter, autonomous control strategies are proposed for PV and battery units operating in a droop controlled islanded microgrid. Based on the proposed strategies, the PV and the battery units can be deployed independently in any droop controlled microgrid. Similar to the strategy developed in Chapter 3, both the PV unit and the battery unit are controlled as voltage sources that follows multi-segment adaptive power/frequency (P/f) characteristic curves. These P/f characteristic curves are adjusted locally in real-time based on the available PV power, load demand, and the state-of-charge of the battery, to autonomously coordinate the operation of these units and maintain the power balance in the microgrid. The strategy proposed for the battery unit enables it to autonomously supply power only during peak load periods, to support the droop controlled units and maintain the power balance in the islanded microgrid. The control strategies are implemented in each unit using multi-loop controllers without relying on communications, a central management algorithm, or switching logic. Small signal models of the proposed control loops are presented, and the performance of the proposed strategy is validated using simulation, and also through experiments on a 4 kVA prototype microgrid.

The problem statement and the objectives of the proposed power management strategy are presented in Section 4.2. The control strategy proposed for a PV unit in a droop controlled microgrid is introduced in Section 4.3. The control strategy of the battery unit in the droop controlled microgrid is presented in Section 4.4. Thereafter, in Section 4.5, the P/f characteristic curves of the PV, the battery, and the droop controlled units are combined into a single P/f characteristic curve that describes the decentralized coordination of the whole microgrid. Small signal models of the proposed control loops are presented in Section 4.6. Simulation results that validate the proposed strategy are discussed in Section 4.7, while the experimental results are presented in Section 4.8,

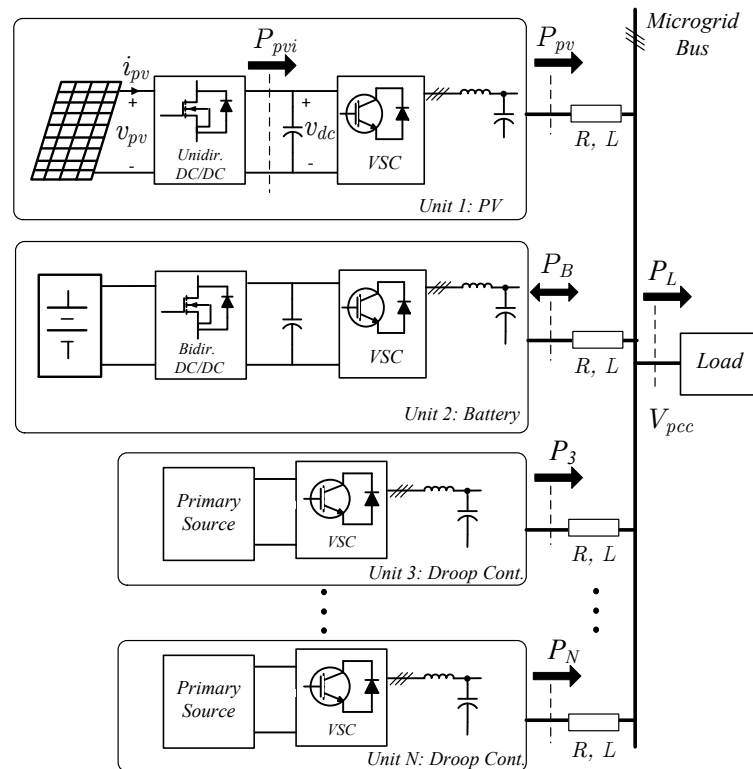


Figure 4.1: Structure of the islanded microgrid.

followed by the concluding remarks.

4.2 Problem Statement and Objectives

The microgrid structure considered in this work is shown in Fig. 4.1, where Unit 1 is the PV unit, Unit 2 is the battery storage unit, and Unit 3 to Unit N are the droop controlled units. The main focus will be on designing the local control strategies for the PV and the battery units to achieve fully decentralized coordination of the power flow in the microgrid. More specifically, the local control strategies of the PV and the battery units must have the following functional features:

1) PV Unit

- The PV unit must be able to track and supply all the available PV power to the microgrid as long as there is sufficient load demand, which includes the battery charging power.
- The PV unit must be able to curtail the PV generation and autonomously match the varying load when the available PV power is higher than the load demand. Matching the varying load must be achieved autonomously, without relying on any external reference signal and communications.

- Transition among the control objectives of supplying all the available power and matching the varying load demand must be initiated by the local control strategy without requiring any external reference, communications, or central management.

2) Battery Unit

- The battery unit supplies power only when the load demand increases beyond the total generation in the microgrid. In other words, the battery is used to supply the peak load only; otherwise it is either being charged or it is floating.
- The charging power must be adjusted locally in real-time based on the load demand, the total available generation, and the battery *SOC*, in order to maintain the power balance in the microgrid.
- The battery unit must be able to switch from charging to supplying peak loads autonomously, without relying on any external reference or central management.
- Transition between the control strategy objectives, as well as the adjustment of the charging power, must only be done by the local controller, without relying on any external reference or communications.

The above objectives are achieved by controlling the PV and the battery units as voltage sources that follow the proposed multi-segment adaptive P/f characteristic curves. According to the proposed P/f characteristics, depending on the microgrid generation/loading conditions at any time, either the PV, the battery, or the droop controlled units will be responsible for regulating the microgrid frequency, while the other units operate as power controlled sources. Switching between frequency regulation and power regulation roles is achieved autonomously by employing the proposed P/f characteristic curves in the local controllers.

Since the main focus of the proposed strategy is on the management of the real power flow as in [43, 51–55, 59, 95], the reactive power flow is regulated to follow a certain reference Q_{ref} , by controlling the unit output voltage [36]. It is worth mentioning that controlling the PV unit as a voltage source provides the opportunity of using V/Q droop control. The topic of accurate reactive power sharing in islanded microgrids has been explored in [66, 70, 74, 76, 77, 92, 96].

4.3 Control Strategy of the PV Unit

Decentralized power management of the PV unit can be achieved through the interaction of the proposed P/f characteristic curves and the characteristics of the droop controlled units. Droop control characteristic curves for Unit 3 to Unit N are shown in Fig. 4.2. As in Chapter 3, these curves can be combined into a single equivalent curve that describes the steady state P/f characteristics of all the droop controlled units, as shown in Fig. 4.2. Therefore, these units can be seen by the microgrid as a single droop controlled unit with P_D representing the output power, and $P_{D-max} = P_{3-max} + \dots + P_{N-max}$ representing the power rating of this equivalent unit.

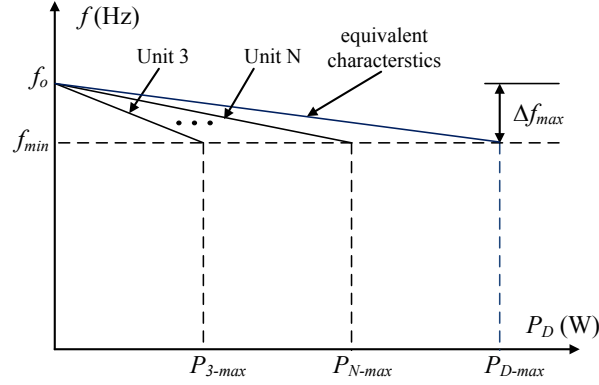
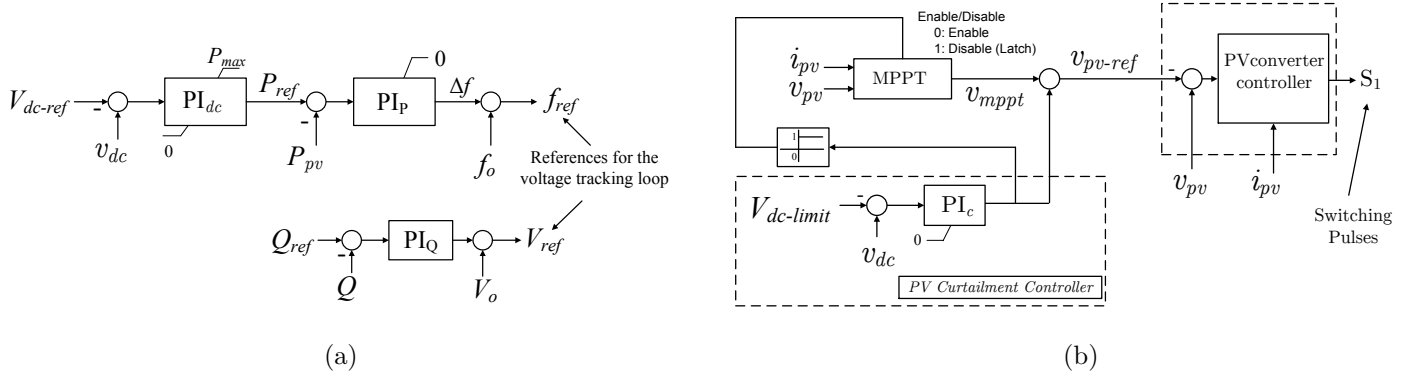
Figure 4.2: P/f characteristics of the droop controlled units.

Figure 4.3: Control system of the PV unit. (a) VSC power controller. (b) PV DC-DC converter controller.

The voltage-sourced converter (VSC) in the PV unit is controlled to supply all the PV power available at the DC-link to the microgrid by controlling the DC-link voltage at its nominal value V_{dc-ref} . On the other hand, the DC-DC converter injects the PV power into the DC-link by regulating the voltage at the PV array terminals (v_{pv}). The controllers of the VSC and the DC-DC converter are shown in Fig. 4.3, where V_o and f_o are the nominal voltage and frequency of the microgrid.

As illustrated in Fig. 4.3, output frequency and voltage are used to control the output real/reactive power of the PV unit, respectively. The controller PI_P regulates the output power by using the frequency deviation Δf . For example, when the reference P_{ref} increases due to an increase in the PV power output, the controller PI_P attempts to follow the reference P_{ref} by increasing Δf . However, the upper limit for Δf is intentionally set to zero, in order to configure the P/f characteristic of the VSC into two segments, called the Power Source Segment and the Voltage Source Segment, as shown in Fig. 4.4a. The power $P_{pv-mppt}$, is the available PV power that can be harvested using a maximum power point tracking (MPPT) algorithm.

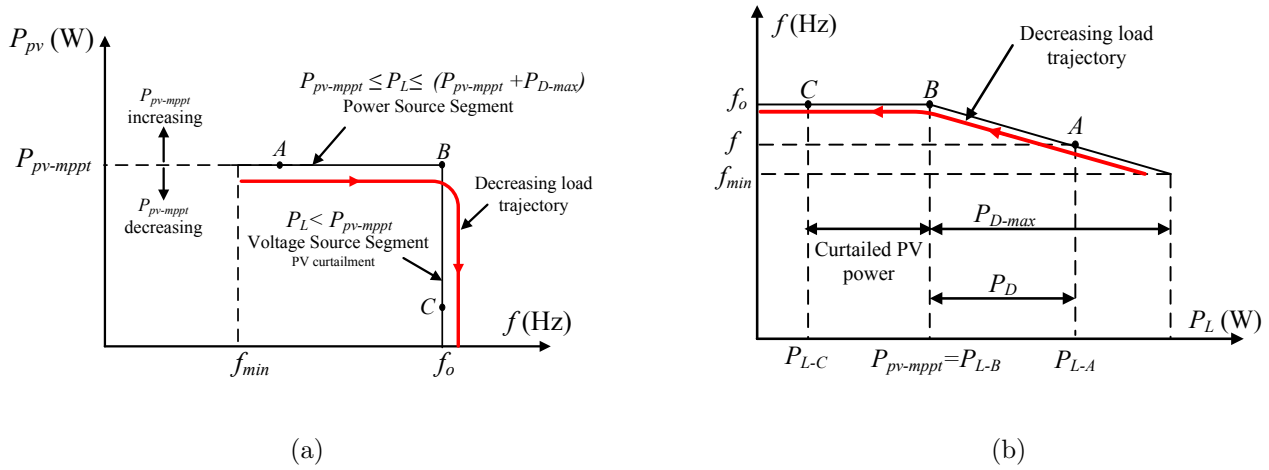


Figure 4.4: Multi-segment P/f characteristics of the PV unit and the microgrid. (a) P/f characteristics of the PV unit. (b) Equivalent P/f characteristics of the microgrid when combining the characteristics of the PV unit and the droop controlled units.

Regardless of the microgrid frequency, which is regulated by the droop controlled units in the range (f_{min}, f_o) , the PV unit continues regulating the output power at $P_{pv-mpppt}$. This is equivalent to the P/f operating point moving horizontally along the Power Source Segment shown in Fig. 4.4a, in response to changes in the load demand. This is the reason behind considering the frequency as the independent variable in Fig. 4.4a. Power regulation is achieved using the integral action of the controller PI_p . For this reason, a PI controller is used instead of the simple droop (proportional) controller that is commonly used in grid connected applications, where the operating frequency is maintained by the grid [65].

The P/f characteristic curves of the PV and the droop controlled units can be combined into a single characteristic curve that describes the operation of the PV unit in a droop controlled microgrid, as shown in Fig. 4.4b. At a given $P_{pv-mpppt}$, the P/f operating point moves along the characteristic curves in Fig. 4.4 as the load demand changes. On the other hand, the characteristic curve in Fig. 4.4a shifts up/down in response to the increase/decrease in $P_{pv-mpppt}$, respectively. Correspondingly, the characteristic curve in Fig. 4.4b shifts to the right or to the left as will be discussed later. In other words, a change in the load demand is reflected in the movement of the P/f operating point, while a change in PV power generation results in shifting the whole P/f characteristic curve. The reactive power (Q) is regulated at the reference Q_{ref} by adjusting the output voltage reference V_{ref} using the controller PI_Q [36, 65].

The behavior of the PV unit and the whole microgrid, in response to different load and PV power output conditions, is discussed under the following scenarios.

$$1) P_{pv\text{-}mppt} \leq P_L \leq (P_{pv\text{-}mppt} + P_{D\text{-}max})$$

In this case, the PV unit is able to supply all the available PV power ($P_{pv\text{-}mppt}$) to the microgrid, while the droop controlled units supply the rest of the load demand, i.e. P_D . This is illustrated by the operating point A in Fig. 4.4b, when $P_L = P_{L\text{-}A}$. The frequency of the microgrid (f) is, therefore, determined and regulated by the droop controlled units based on P_D and the equivalent droop characteristic. Note that, each unit supplies its share of the total P_D based on its own droop characteristic shown in Fig. 4.2.

$$2) P_{pv\text{-}mppt} > P_L$$

The droop controlled units raise the operating frequency in response to any decrease in the delivered load, while following the decreasing load trajectory shown in Fig. 4.4. The operating frequency continues increasing as the load demand drops, until all the load is supplied by the PV unit, and $f = f_o$ at point B in Fig. 4.4. At this point, $P_D = 0$ W, and $P_{L\text{-}B} = P_{pv\text{-}mppt}$.

Any decrease in the load demand beyond this point results in the droop controlled units attempting to increase the frequency above f_o according to their droop characteristics. On the other hand, the PV unit attempts to supply all the PV power to the microgrid by also increasing the frequency. However, Δf is limited to zero and, therefore, the PV unit starts regulating the frequency at $f = f_o$ as shown in Fig. 4.4. This results in regulating the droop controlled output at zero power, and in the PV units matching all the available load demand autonomously, e.g. supplying the load $P_{L\text{-}C}$ at point C in Fig. 4.4b.

Even though the power is curtailed at the output of the PV unit, the DC-DC converter continues to inject $P_{pv\text{-}mppt}$ into the DC-link. Consequently, the surplus PV power, i.e. $P_{pv\text{-}mppt} - P_L$, causes the DC-link voltage to increase above the nominal DC-link voltage ($V_{dc\text{-}ref}$). This is utilized by the *PV Curtailment Controller*, shown in Fig. 4.3b, to adjust the PV harvested power in order to regulate the DC-link voltage at the new set point $V_{dc\text{-}limit}$, while matching the load demand.

The *PV Curtailment Controller* reduces the PV power to match the load demand by moving the PV operating point away from the maximum power point (MPP), as shown in Fig. 4.5. The controller continues adjusting the PV operating point in response to any load change, so that the PV power matches the load and the DC-link voltage stays regulated, as follows:

- Initially, the DC-link voltage is regulated by the VSC at $V_{dc\text{-}ref}$, and the output of the PI_c remains zero, while $V_{pv\text{-}ref}$ is generated solely by the MPPT algorithm. Note that, initially, the PI_c can only increase the $v_{pv\text{-}ref}$.
- Once P_L decreases below $P_{pv\text{-}mppt}$, the DC-link voltage tends to increase beyond the $V_{dc\text{-}limit}$. At this point, MPPT is disabled and the PI_c starts regulating the DC-link voltage by increasing $v_{pv\text{-}ref}$ and, hence, reducing the PV power until it matches the load demand.
- At this point, the PI_c has the ability to either increase or decrease the $v_{pv\text{-}ref}$ to regulate the DC-link voltage at $V_{dc\text{-}limit}$. Accordingly, if the load increases again,

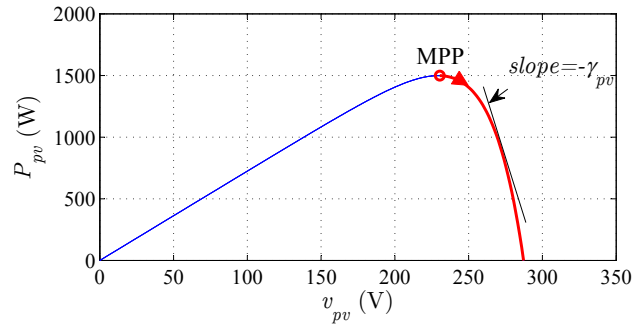


Figure 4.5: Power characteristic curve of a PV array showing the curtailment operating region.

the VSC supplies the new load increase and, therefore, the DC-link voltage tends to decrease below $V_{dc-limit}$. Consequently, PI_c decreases the v_{pv-ref} , i.e. moves the operating point towards the MPP again to match the increased load demand, and keep the voltage regulated at $V_{dc-limit}$.

- If the load demand continues to increase, the output of the PI_c continues decreasing until it becomes zero. At this point, the MPPT algorithm is reactivated. Any increase in the load beyond this point will cause the DC-link voltage to drop to V_{dc-ref} when the VSC starts regulating the DC-link voltage again, while the droop controlled units supply the rest of the increased load.

3) $P_{pv-mppt}$ Variations

As mentioned earlier, the increase/decrease in the PV power $P_{pv-mppt}$ results in shifting the P/f characteristic curve in Fig. 4.4b to the right/left, respectively. Coordination of the power flow in the microgrid in response to a PV power change is illustrated in Fig. 4.6. As the available PV power and, hence, the unit output power increases from $P_{pv-mppt-A}$ to $P_{pv-mppt-B}$, the P/f curve shifts to the right, which results in decreasing the power delivered by the droop controlled units from P_{D-A} to P_{D-B} . Consequently, this results in increasing the frequency from f_A to f_B in response to the decrease in the output power of the droop controlled units.

If the PV power increases such that $P_{pv-mppt} > P_L$, P_D will reduce to zero and the PV unit starts matching the load demand while curtailing the PV power, as discussed previously and shown in Fig. 4.4b.

4.4 Control Strategy of the Battery Unit

According to the proposed control strategy, the battery VSC is nominally controlled to regulate the output power at $-P_{ch-ref}$ by controlling the output frequency. In other words, voltage-mode control is used to regulate the output power. The reference P_{ch-ref} represents the charging power reference that varies between 0 and P_{ch-max} , depending on the

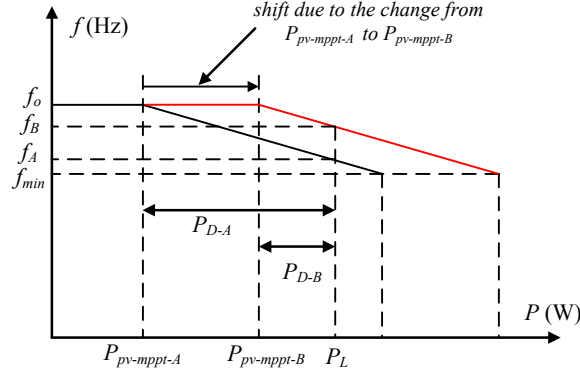


Figure 4.6: Shift in the microgrid P/f characteristic due to a change in the PV power from $P_{pv-mppt-A}$ to $P_{pv-mppt-B}$.

battery SOC and the battery specifications. The frequency control range is intentionally constrained by the minimum limit f_{min} in order to segment the P/f characteristic curve as shown in Fig. 4.7.

The reference P_{ch-ref} can be determined, based on the battery SOC , using a fixed charging curve as in [29, 88, 90, 91]. Also, P_{ch-ref} can be generated based on the battery voltage using two- or three-stage charging scenarios [87]. Since the main focus in this paper is on the power management of the microgrid, a charging curve similar to the one used in [29] is considered adequate for this purpose. This charging curve is shown in Fig. 4.8, and the exponential part can be determined by

$$P_{ch-ref} = P_{B-max} - P_{B-max} \left(1 - e^{-\frac{SOC - SOC_{ref} + \delta SOC}{\delta SOC / k_{\delta}}} \right) \quad (4.1)$$

where SOC_{ref} is the battery SOC that the controller intends to reach. The constant k_{δ} determines how fast P_{ch-ref} approaches zero when the SOC approaches SOC_{ref} . Both k_{δ} and δSOC are chosen based on the battery specification and the design preference.

Any decrease/increase in the reference P_{ch-ref} results in shifting the P/f curve up/down as illustrated in Fig. 4.7. The P/f characteristic curves of the battery unit and the droop controlled units can be combined into a single curve that describes the operation of the microgrid, as shown in Fig. 4.9. Two operational cases are considered in Fig. 4.9. *Case I* illustrates P/f curve when the battery is fully charged and, therefore, $P_{ch-ref} = 0$, while the droop controlled units supply the load demand only ($P_{D-I} = P_L$).

On the other hand, *Case II* shows the P/f curve when $P_{ch-ref} > 0$, i.e., when the controller attempts to charge the battery at $P_B = -P_{ch-ref}$. This results in shifting the P/f curve of *Case I* to the left, and in extending the length of the flat segment from P_{B-max} to $(P_{B-max} + P_{ch-ref})$.

In *Case II*, the droop controlled units charge the battery, at P_{ch-ref} , as a part of the total load demand in the microgrid, i.e. $P_{D-II} = P_L + P_{ch-ref}$. However, if the load demand increases such that $(P_L + P_{ch-ref}) > P_{D-max}$, the battery unit starts decreasing the charging power autonomously, so that the droop controlled units can supply the

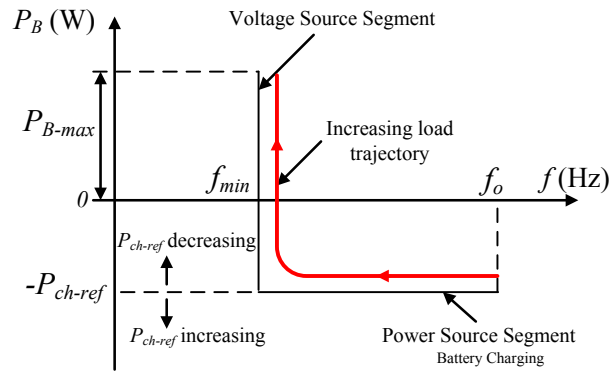


Figure 4.7: Multi-segment P/f characteristics of the Battery unit.

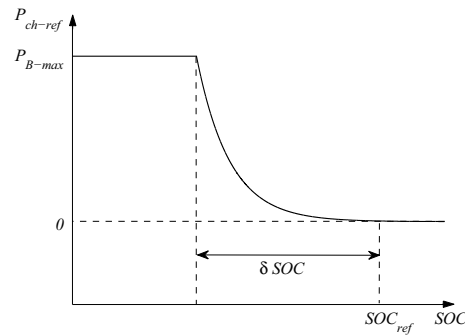


Figure 4.8: P_{ch-ref}/SOC charging curve.

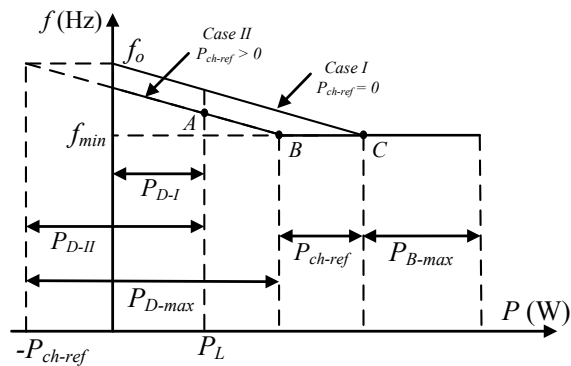


Figure 4.9: Equivalent P/f characteristics of the battery unit and the droop controlled units, for different values of P_{ch-ref} .

load, in addition to charging the battery at a reduced rate ($P_{ch} < P_{ch-ref}$). This can be achieved autonomously by relying on the P/f characteristic curve of the battery unit,

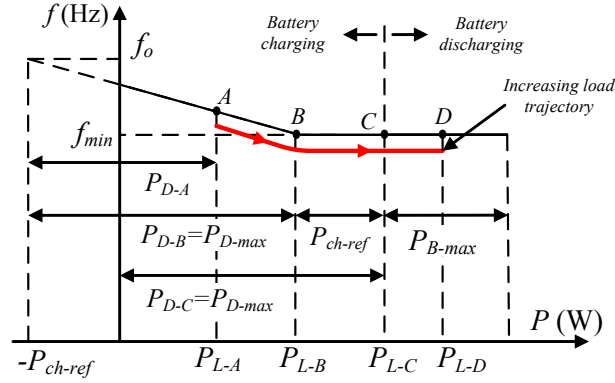


Figure 4.10: Equivalent P/f characteristics of the microgrid showing the increasing load trajectory - Supplying the peak load from the battery.

without requiring any external reference and a central management algorithm, as shown in Fig. 4.10, and explained in the following:

- Initially, $P_L = P_{L-A}$ (point A), the battery is charging at P_{ch-ref} , and the droop controlled units supply all the load demand including the charging power ($P_{D-A} = P_{L-A} + P_{ch-ref}$).
- The droop controlled units continue supplying any increase in the load until $P_L = P_{L-B}$. At this point (point B), the droop controlled units reach their ratings P_{D-max} at $f = f_{min}$, while supplying the load, and charging the battery at P_{ch-ref} , i.e. ($P_{D-max} = P_{L-B} + P_{ch-ref}$).
- If the load increases further beyond this point, the droop controlled units attempt to drop the frequency below f_{min} according to their droop control characteristics. On the other hand, the battery unit starts regulating the frequency at f_{min} (see point B), due to the chosen limit of the controller PI_P output. This results in limiting the output of the droop controlled units at their rated powers, while reducing the power flow into the battery unit in response to any increase in the load. This is equivalent to the operating point moving from point B towards point C, which happens because the battery unit operates as a voltage source that regulates the frequency at f_{min} . On the other hand, the output powers of the droop controlled units are regulated at their ratings, i.e. they start operating as power controlled sources.
- Any increase in the load demand will continue to be supplied from the droop controlled units, until the battery charging power is reduced to zero ($P_B = 0$) at point C, and the droop controlled units supply the load only, i.e. $P_{D-C} = P_{L-C}$.
- Any further increase in the load, e.g. $P_L = P_{L-D}$ (point D), will be supplied solely by the battery unit. In this case, the battery starts discharging to supply the

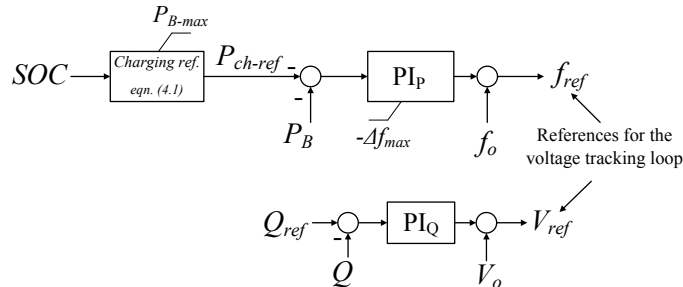


Figure 4.11: Control strategy of the battery unit that produces the proposed P/f characteristic curve

increased load. This is achieved autonomously due to controlling the battery unit as a voltage source with a fixed frequency in this segment.

In conclusion, even though the nominal objective of the battery control strategy is to regulate the output power at a certain reference in the range $\{-P_{ch-max}, 0\}$, it can always adjust the output power autonomously to maintain the power balance in the microgrid, without requiring any communication or a central management strategy.

The implementation of the VSC controller that achieves the proposed P/f characteristic curve is illustrated in Fig. 4.11. In addition, the battery DC-DC converter is controlled to regulate the DC-link voltage at its nominal value using the voltage controller presented in Appendix A.

4.5 Decentralized Coordination of the PV, the Battery, and the Droop Controlled Units

Combining the P/f characteristic curves of the PV, battery and the droop controlled units results in the multi-segment P/f curve shown in Fig. 4.12a, which describes the decentralized coordination of the whole microgrid. The left hand (flat) segment of the P/f curve corresponds to the operating region where the PV unit operates as a voltage source with a fixed frequency, while both the battery unit and the droop controlled units operate as power controlled sources. In this segment, the PV unit regulates the microgrid frequency, while curtailing the PV power to maintain the power balance in the microgrid, as discussed in Section 4.3 and shown in Fig. 4.4b.

The right hand (flat) segment of the P/f curve shows the region where the battery operates as a voltage source with a fixed frequency to ensure supplying the peak load demand in the microgrid, as shown in Fig. 4.10 and discussed in Section 4.4. In this region, the microgrid frequency is regulated by the battery unit, while both the PV and the droop controlled units operate as power controlled sources.

In the middle (droop) segment, both the PV and the battery units operate as power controlled sources, while the droop controlled units regulate the microgrid frequency according to their droop characteristics. Note that, in Fig. 4.12a, $P_{pv-mppt}$ is assumed to

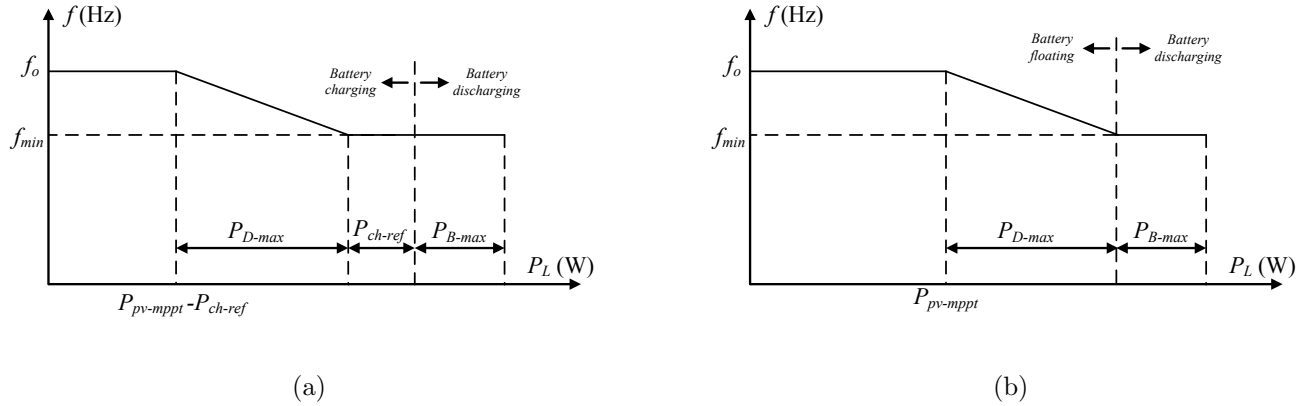


Figure 4.12: P/f characteristics of the PV, the battery, and the droop units combined in a single multi-segment curve for the microgrid (a) when $P_{ch-ref} > 0$ (battery charging); (b) when $P_{ch-ref} = 0$ (battery floating).

be higher than P_{ch-ref} . When $P_{pv-mppt} = 0$ or $P_{pv-mppt} < P_{ch-ref}$, the P/f characteristic will be similar to that shown in Fig. 4.9.

On the other hand, when the battery is fully charged, i.e. $P_{ch-ref} = 0$, the P/f characteristic curve in Fig. 4.12a will shift to the right resulting in the characteristic curve illustrated in Fig. 4.12b. In conclusion, all the operational features discussed separately in Sections 4.3 and 4.4, for the PV and the battery units, are valid when both units are operating in a droop controlled microgrid.

4.6 Small-Signal Modeling of the Proposed Control Loops

The voltage controllers for the DC-DC converters are designed in this work as in [50], while the voltage tracking loops for the VSCs are designed as in [14]. Since control designs of the voltage controllers for the DC-DC converters and VSCs are well established in the literature, the main focus in this section is only on the power control loops, and the DC-link voltage regulation loops in the PV unit, to gain insight into the dynamics of these loops.

4.6.1 Power Control Loops

The power control loop represents the inner loop of the DC-link voltage controller in the PV unit (see Fig. 4.3a), and the main loop of the battery power controller. The real and reactive power flows at the output of the DG unit are described as follows [94]:

$$P = \frac{(RV^2 - RVV_{pcc} \cos \delta + XVV_{pcc} \sin \delta)}{R^2 + X^2} \quad (4.2)$$

$$Q = \frac{(XV^2 - XVV_{pcc} \cos \delta - RVV_{pcc} \sin \delta)}{R^2 + X^2} \quad (4.3)$$

where R and X are the resistive and inductive components of the feeder impedance, δ is the power angle, V is the unit output voltage, and V_{pcc} is the microgrid bus voltage. The real and reactive power controller equations, taking into account the low-pass filters in the measurement channels, are given by

$$\omega = \omega_o + \frac{K_{p-p} s + K_{i-p}}{s} (P_{ref} - \frac{1}{T_s + 1} P) \quad (4.4)$$

$$V = V_o + \frac{K_{p-q} s + K_{i-q}}{s} (Q_{ref} - \frac{1}{T_s + 1} Q) \quad (4.5)$$

where ω is the angular frequency in rad/s, V_o and ω_o are the nominal voltage and angular frequency, K_{p-p} and K_{i-p} are the proportional and integral gains of the real power controller (PI_P), K_{p-q} and K_{i-q} are the proportional and integral gains of the reactive power controller (PI_Q). Linearizing (4.2), (4.3), (4.4), and (4.5) around an operating point

$$\begin{aligned} \Delta P &= \left(\frac{\partial P}{\partial V}\right) \Delta V + \left(\frac{\partial P}{\partial \delta}\right) \Delta \delta \\ &= K_{pv} \Delta V + K_{p\delta} \Delta \delta \end{aligned} \quad (4.6)$$

$$\begin{aligned} \Delta Q &= \left(\frac{\partial Q}{\partial V}\right) \Delta V + \left(\frac{\partial Q}{\partial \delta}\right) \Delta \delta \\ &= K_{qv} \Delta V + K_{q\delta} \Delta \delta \end{aligned} \quad (4.7)$$

$$\Delta \omega = \frac{K_{p-p} s + K_{i-p}}{s} (\Delta P_{ref} - \frac{1}{T_s + 1} \Delta P) \quad (4.8)$$

$$\Delta V = -\frac{K_{p-q} s + K_{i-q}}{s(T_s + 1)} \Delta Q = G_v(s) \Delta Q \quad (4.9)$$

where K_{pv} , $K_{p\delta}$, K_{qv} , and $K_{q\delta}$ are calculated at the considered operating point.

Substituting for ΔQ from (4.9) in (4.7), ΔV can be given by

$$\Delta V = \frac{G_v(s) K_{q\delta}}{1 - K_{qv} G_v(s)} \Delta \delta = G_{v\delta}(s) \Delta \delta \quad (4.10)$$

Substituting for ΔV from (4.10) in (4.6), ΔP can be written as

$$\Delta P = (K_{pv} G_{v\delta}(s) + K_{p\delta}) \Delta \delta = G_{p\delta}(s) \Delta \delta \quad (4.11)$$

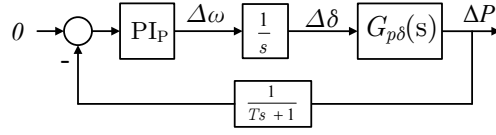
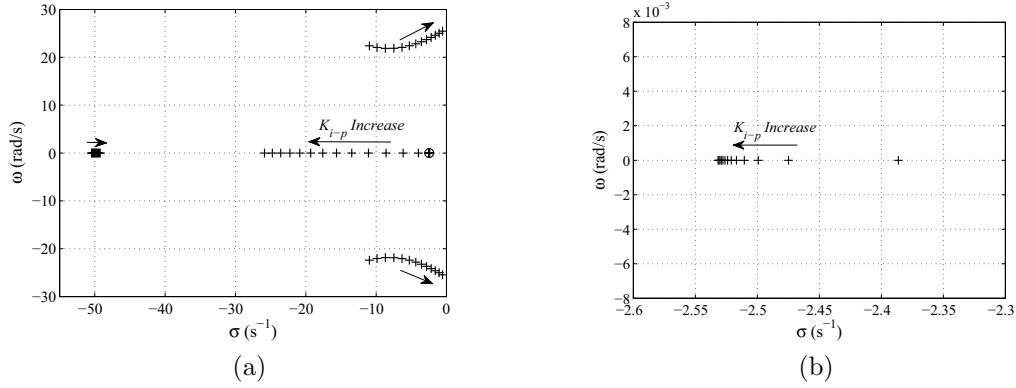


Figure 4.13: Linearized model of the power control loop.

Figure 4.14: Root trajectories of the power control loops when the gain K_{i-p} is varied from 0.01 to 0.07 with a step of 0.005 rad/(W·s²). (a) All the root trajectories. (b) Zoomed in view of the encircled root trajectory.

Considering that $\Delta\omega = s\Delta\delta$, (4.11) can be rewritten as

$$\Delta P = \frac{1}{s} \cdot G_{p\delta} \Delta\omega \quad (4.12)$$

Using (4.8), (4.11), and (4.12), the linearized closed-loop is shown in Fig. 4.13, and the transfer function of the closed-loop system can be written as

$$G_P(s) = \frac{b_4 s^4 + b_3 s^3 + b_2 s^2 + b_1 s + b_0}{a_5 s^5 + a_4 s^4 + a_3 s^3 + a_2 s^2 + a_1 s + a_0} \quad (4.13)$$

where the parameters a_5 to a_0 , and b_4 to b_0 are detailed in Appendix B. Trajectories of the the closed-loop poles, considering the system parameters in Table 4.1, are shown in Fig. 4.14 when the gain K_{i-p} is varied from 0.01 to 0.07 with a step of 0.005 rad/(W·s²), and K_{p-p} is set to $2\pi \times 0.0005$ rad/(W·s). The zoomed-in view of the encircled root trajectory is shown Fig. 4.14b, which shows that the effect of the gain K_{i-p} on the position of this pole is insignificant. The position of this pole is mainly determined by the integral gain of the reactive power controller.

4.6.2 DC-Link Voltage Regulation Loop

The DC-link voltage dynamics can be expressed as

Table 4.1: System Parameters

Description	Parameter	Value
PV Unit Power Rating	P_{pv-max}	1500 W
Battery Unit Power Rating	P_{B-max}	1000 W
Unit 3 Rating	P_{3-max}	1500 W
Unit 4 Rating (simulation)	P_{4-max}	1000 W
Frequency Droop Limit	Δf_{max}	0.25 Hz
Nominal DC-link Voltage	V_{dc-ref}	400 V
Nominal Battery Voltage	V_B	192 V
Battery Capacity	C_{bat}	32 Ah
PV Open Circuit Voltage	V_{oc}	287 V
PV Short Circuit Current	I_{sc}	7.25 A
DC-Link Capacitors	C_{dc}	2400 μ F
Feeder Inductance	L	4 mH
Feeder Resistance	R	1.1 Ω
PI _P Controller Gains	K_{p-p}	$2\pi \times 0.0005$ rad/(W·s)
	K_{i-p}	$2\pi \times 0.005$ rad/(W·s ²)
PI _Q Controller Gains	K_{p-q}	0.01 V/var
	K_{i-q}	0.5 V/(var·s)
PI _{dc} Controller Gains	K_{pdc}	20 W/V
	K_{idc}	40 W/(V·s)
PI _c Controller Gains	K_{p-c}	20
	K_{i-c}	40 (1/s)

$$\frac{1}{2}C_{dc} \frac{dv_{dc}^2}{dt} = P_{pvi} - P_{pv} = P_{net} \quad (4.14)$$

where C_{dc} is the DC-link capacitor, P_{pvi} is the PV power injected into the DC-link by the PV DC-DC converter, and P_{pv} is the power delivered to the microgrid, which is regulated at P_{ref} by the inner power control loop (see Fig. 4.3a). P_{net} is the net power injected/extracted in/from the DC-link capacitor. Linearizing (4.14) around the operating point $P_{net} = 0$ W, and $v_{dc} = V_{dc-ref}$

$$\frac{d\tilde{v}_{dc}}{dt} = \frac{1}{V_{dc-ref}C_{dc}} \Delta P_{net} \quad (4.15)$$

where \tilde{v}_{dc} is the small signal perturbation of v_{dc} around the considered operating point. In s-domain, (4.15) is given by

$$\tilde{v}_{dc} = \frac{1}{V_{dc-ref}C_{dc}s} \Delta P_{net} = G_{dc}(s) \Delta P_{net} \quad (4.16)$$

Accordingly, the model of the DC-link voltage regulation loop can be developed as in Fig. 4.15, and the characteristic equation of the closed-loop can be written as

$$\bar{a}_7 s^7 + \bar{a}_6 s^6 + \bar{a}_5 s^5 + \bar{a}_4 s^4 + \bar{a}_3 s^3 + \bar{a}_2 s^2 + \bar{a}_1 s + \bar{a}_0 = 0 \quad (4.17)$$

where the parameters \bar{a}_7 to \bar{a}_0 are defined in Appendix B. Trajectories of the characteristic equation roots are shown in Fig. 4.16, when the integral gain K_{idc} is changed from 10 to 100 with a step of 1 W/(V·s), while K_{pdc} is set to 20 W/V.

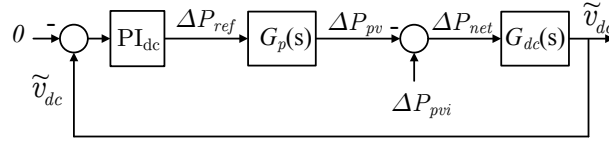
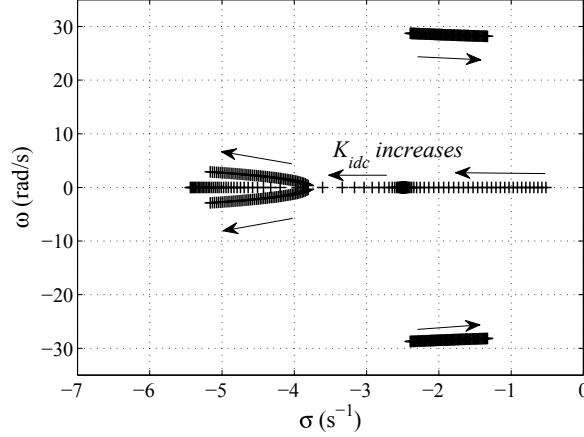


Figure 4.15: Linearized model of the DC-link voltage regulation loop.

Figure 4.16: Root trajectories of the DC-link regulation loop when the integral gain K_{idc} is changed from 10 to 100 with a step of 1 W/(V·s), while K_{pdc} is set to 10 W/V.

4.6.3 PV Curtailment Control Loop

The dynamics of $G_{dc}(s)$ are much slower than those of the inner PV voltage control loop. More specifically, the bandwidth of the PV control loop, as designed in [50], is 471 rad/s, in comparison to 0.96 rad/s, which is the bandwidth of $G_{dc}(s)$. Therefore, the PV voltage control loop can be approximated by a unity gain throughout the considered bandwidth. Accordingly, the model of the curtailment loop can be approximated as in Fig. 4.17, where $f(v_{pv})$ represents the PV power characteristics as a function of the PV array voltage, which is a nonlinear function (see Fig. 4.5). To linearize the loop, this function is approximated by a straight line with a slope of $-\gamma_{pv}$ in the region around the considered operating point, as shown in Fig. 4.5. Accordingly, the linearized model of the curtailment control loop is shown in Fig. 4.18. The characteristic equation of the closed-loop in Fig. 4.18 can be written as

$$C_{dc}V_{dc-limit}s^2 + \gamma_{pv}K_{p-c}s + \gamma_{pv}K_{i-c} = 0 \quad (4.18)$$

where K_{p-c} and K_{i-c} are the proportional and integral gains of the controller PI_c . The trajectory of the dominant pole is shown in Fig. 4.19, when the gain K_{i-c} is varied between 10 and 60 with a step of 0.5/s, and K_{p-c} is set to 20. The other non-dominant pole changes between -594.7 to -592.2 rad/s. The gain γ_{pv} is calculated as 40 W/V at $P_{pvi} = 1000$ W, considering the nominal irradiance and temperature.

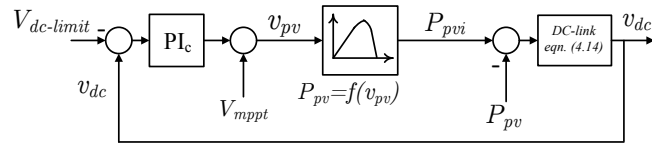


Figure 4.17: Approximated model of the PV curtailment control loop.

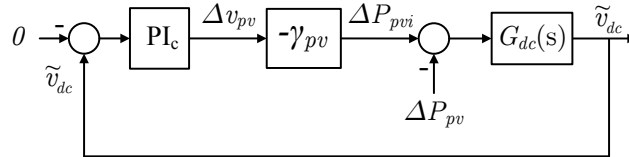
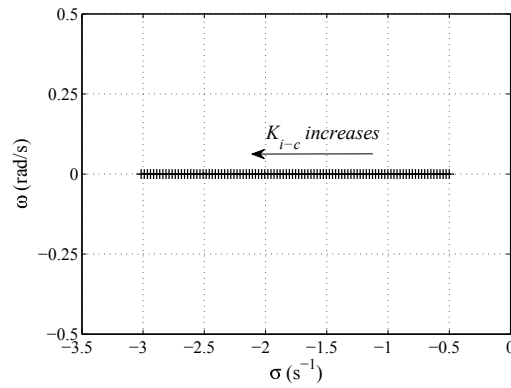


Figure 4.18: Linear model of the PV curtailment control loop.


 Figure 4.19: Root trajectories of the PV curtailment control loop when the gain K_{i-c} is changed between 10 and 60 with a step of 0.5/s, and K_{p-c} is set to 20.

4.7 Simulation Studies

A four-unit microgrid is simulated in PSCAD/EMTDC to validate the performance of the proposed control strategy. This microgrid consists of a PV unit, a battery unit, and two droop controlled units, which are referred to as Unit 3 and Unit 4. The parameters of the units are listed in Table 4.1. The performance of the proposed strategy is examined throughout the following operation scenarios:

4.7.1 Simulated Performance of the PV Control Strategy

The performance of the PV control strategy in response to load demand variations is illustrated in Fig. 4.20. Since the focus is on the performance during different loading conditions, the solar irradiance (1000 W/m^2) and, hence, $P_{pv-mpppt}$, are fixed during this scenario. Also, the battery is considered to be fully charged and, therefore, P_B is regulated

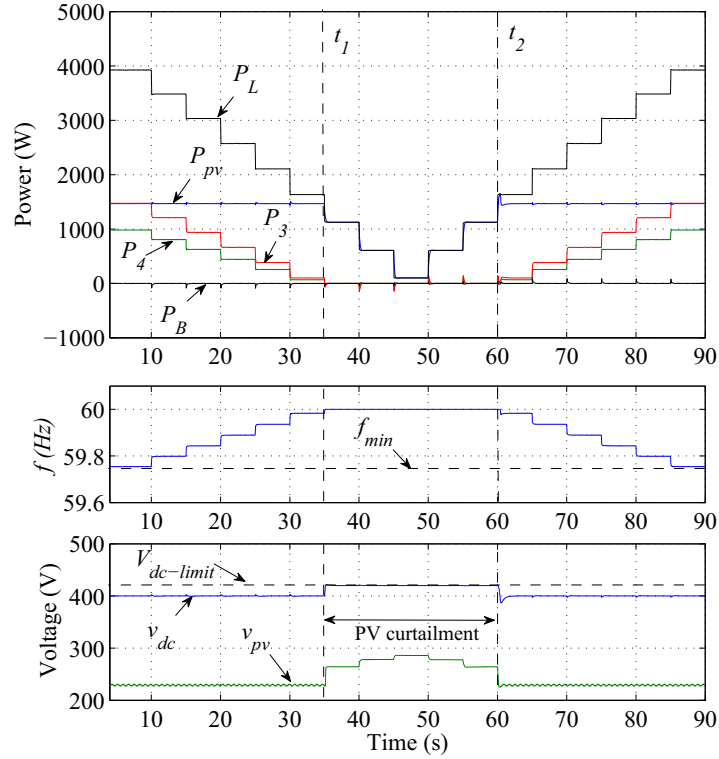


Figure 4.20: Simulated performance of the PV control strategy in response to variations in load demand.

at $P_{ch-ref} = 0$.

Initially, the PV unit supplies all the available PV power to the microgrid, while the droop controlled units share the rest of the load and regulate the frequency based on their droop characteristics. In other words, the microgrid is operating in the middle segment of the P/f characteristic in Fig. 4.12a, until $t = t_1$. At this point, the load demand drops below the available PV power $P_{pv-mppt}$, and the PV unit starts matching the varying load autonomously while regulating the microgrid frequency at $f_o = 60$ Hz, as discussed in Section 4.3. On the other hand, the PV curtailment controller starts adjusting the PV operating point autonomously, based on the delivered power, to curtail the surplus PV power while regulating the DC-link voltage at $V_{dc-limit} = 420$ V. Meanwhile, the outputs of the droop controlled units and the battery unit are regulated at zero output power as discussed in Section 4.3.

The PV unit continues to match the microgrid load until it increases above $P_{pv-mppt}$ at $t = t_2$. The microgrid P/f behavior between $t = t_1$ and $t = t_2$ can be graphically illustrated by the P/f operating point trajectory between points B and C in Fig. 4.4b.

At $t = t_2$, the PV unit starts regulating the output power at $P_{pv-mppt}$ again, while the droop controlled units supply the rest of the load and regulate the microgrid frequency. The output of the PV curtailment controller (PI_c) is reduced to zero at $t = t_2$ and, therefore, the MPPT algorithm is reactivated. Also, the VSC starts regulating the DC-

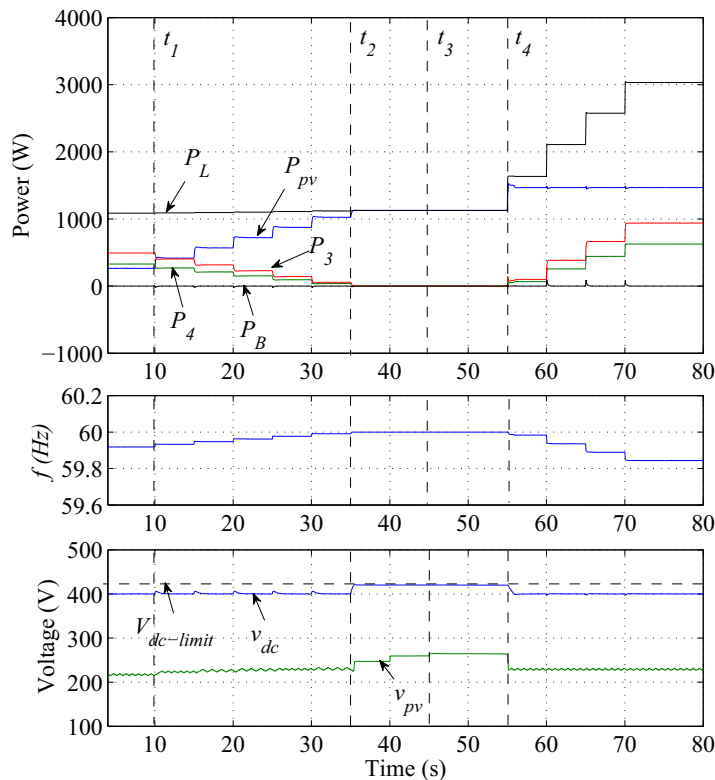


Figure 4.21: Simulated behavior of the PV control strategy in response to variations in the available PV power.

link voltage again at $V_{dc-ref} = 400$ V, as proposed in Section 4.3.

The behavior of the PV control strategy in response to variations in the available PV power is illustrated in Fig. 4.21. Initially, the solar irradiance is set to 200 W/m^2 . At $t = t_1$ the irradiance is increased with steps of 100 W/m^2 until it reaches 1000 W/m^2 at $t = t_3$. Between $t = t_1$ and $t = t_2$, the PV unit tracks and supplies the increasing PV power to the microgrid, while the droop controlled units supply the rest of the load demand and regulate the microgrid frequency. This is equivalent to shifting the P/f characteristic to the right as illustrated previously in Fig. 4.6. At $t = t_2$, the available PV power becomes higher than the load demand, and the PV unit starts matching the load demand autonomously while curtailing the surplus PV power, regulating the frequency at $f_o = 60$ Hz, and regulating the DC-link voltage at $V_{dc-limit}$.

Meanwhile, the power outputs of the droop controlled units are regulated at zero. Note that, the irradiance changes twice in the period between t_2 and t_4 . This can be observed by the change in the PV voltage v_{pv} , which is adjusted by the PV curtailment controller to successfully curtail the increase in the surplus PV power. At $t = t_4$, the load demand increases beyond the available PV power. Accordingly, the output of the PV curtailment controller reduces to zero and the MPPT algorithm is reactivated to operate at the MPP.

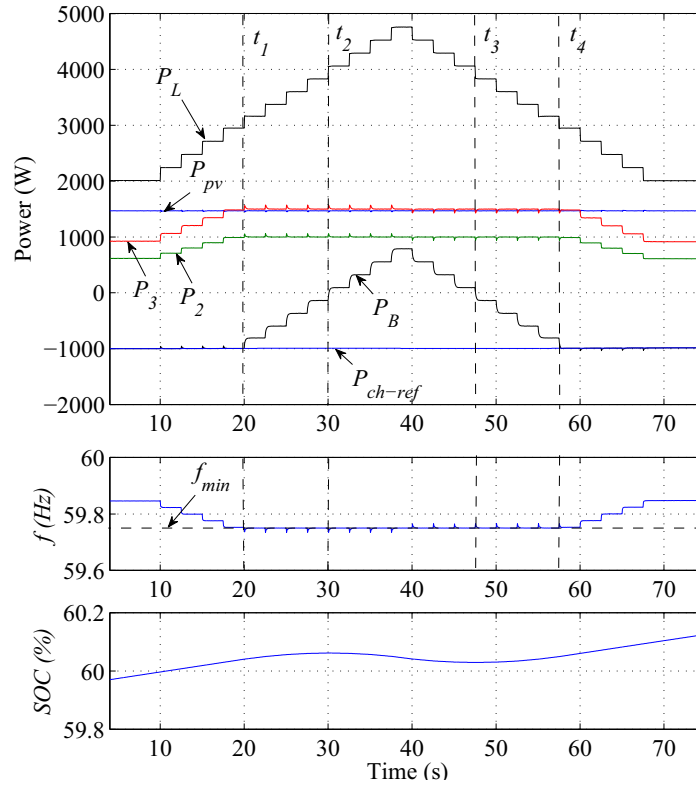


Figure 4.22: Simulated performance of the battery unit using the proposed controller.

4.7.2 Simulated Performance of the Battery Control Strategy

Simulated performance of the battery control strategy is illustrated in Fig. 4.22. In this scenario, the output power of the PV unit is regulated at P_{pv-mpp} and the droop controlled units match the rest of the load demand, while regulating the microgrid frequency.

On the other hand, the battery unit absorbs power initially, as part of the load demand, to charge the battery at $P_B = -P_{ch-ref}$. The reference P_{ch-ref} is determined based on the charging curve in Fig. 4.8 and (4.1), where $SOC_{ref} = 90\%$, $\delta SOC = 30\%$, and $k_\delta = 4$. Accordingly, the charging power reference is set to $-P_{B-max}$, and reduced once SOC exceeds 60%. The change in P_{ch-ref} is not noticeable in Fig. 4.22 due to the insignificant change in the SOC during the relatively short simulation period. However, the change in P_{ch-ref} will be emphasized in the experimental results in Section 4.8.2, due to the longer experiment periods.

The droop controlled units continue supplying the increasing load until $t = t_1$, when they reach their rated power limits at $f = f_{min}$. At this point, the battery unit starts regulating the frequency at $f_{min} = 59.75$ Hz. This results in reducing the power flows into the battery while matching the increase in the load demand until $t = t_2$. From t_1 to t_2 , the charging power is determined by the available generation and load demand, regardless of the reference $P_B = P_{ch-ref}$ value, in order to maintain the power balance in the microgrid. The microgrid P/f behavior between $t = t_1$ and $t = t_2$ can graphically be

illustrated by the P/f operating point trajectory between points B and C in Fig. 4.10.

At $t = t_2$, the load becomes higher than the total generation in the microgrid, and therefore, the battery unit starts discharging to match the increasing load autonomously until $t = t_3$. The microgrid P/f behavior between $t = t_2$ and $t = t_3$ is equivalent to moving the P/f operating point along the trajectory between points C and D in Fig. 4.10.

At $t = t_3$, the load demand drops below the total generation in the microgrid, and the battery starts charging again. Between t_3 and t_4 , the charging power is determined by the battery unit autonomously based on the available generation and load demand. In other words, the charging power increases with any decrease in the load demand, until the charging power attempts to increase beyond P_{ch-ref} at $t = t_4$. At this point, the battery unit starts regulating P_B at P_{ch-ref} , while the droop controlled units start regulating the microgrid frequency, while matching the rest of the load, i.e. $(P_L + P_{ch-ref}) - P_{pv-mppt}$.

4.8 Experimental Evaluation

Since the microgrid prototype consists of two units only, the control strategy of the PV unit and the battery unit are validated separately using two case studies. In the first case, the microgrid consists of a PV unit, configured as in Fig. 4.1, and a droop controlled unit. In the second case, the microgrid consists of a battery unit and a droop controlled unit. In both cases, the droop controlled unit represents Unit 3 in Table 4.1, with the output power referred to as P_D . Internal measurements of voltage, power, frequency, and calculated SOC are sent via serial-to-Ethernet converters to central data collection and plotting software, which is implemented in Python and run under Ubuntu Linux.

4.8.1 Experimental Performance of the PV Control Strategy

System performance in response to variations in the load demand is shown in Fig. 4.23. This experimental performance successfully validates the proposed strategy and the simulation results introduced in Section 4.7.1 and shown in Fig. 4.20. As illustrated in Fig. 4.23, the PV unit successfully matches the load demand autonomously between $t = t_1$ and $t = t_2$, when the load demand P_L is less than the available PV power $P_{pv-mppt}$. During this period the microgrid frequency is regulated by the PV unit at $f = f_o$. At the same time, the PV curtailment controller adjusts the PV operating point autonomously to curtail the surplus PV power while regulating the DC-link voltage at $V_{dc-limit} = 420$ V. Meanwhile, the output of the droop controlled unit is regulated at zero.

On the other hand, when the load demand is larger than the available PV power, the PV unit starts supplying all the PV power to the microgrid, while the droop controlled unit shares the rest of the load, and regulates the microgrid frequency. This is illustrated by the system performance during the periods of $(t < t_1)$ and $(t > t_2)$ in Fig. 4.23.

The experimental behavior of the PV control strategy in response to variations in the available PV power is shown in Fig. 4.24, to validate the simulated performance in Fig. 4.21. The solar irradiance is changed from 300 W/m² at $t = t_1$ to 1000 W/m² at

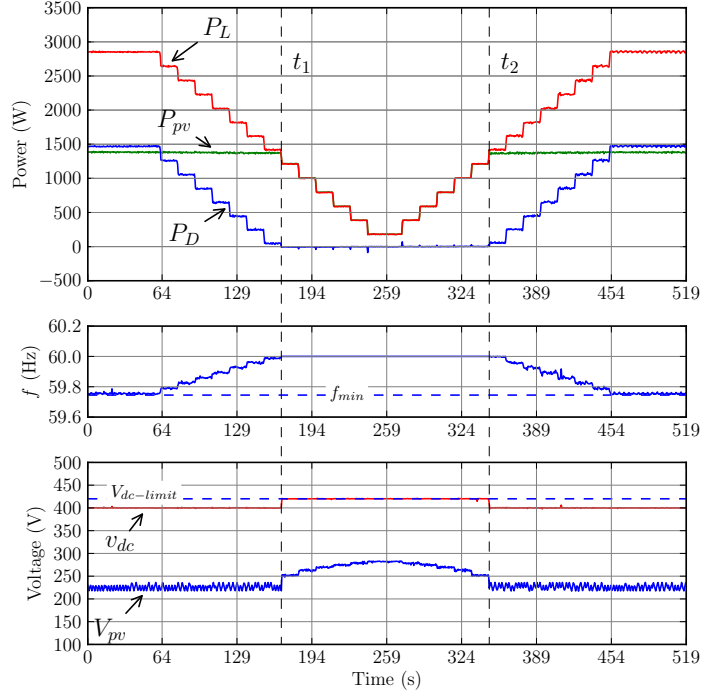


Figure 4.23: Experimental performance of the PV unit in response to variations in load demand.

$t = t_3$, with steps of 100 W/m^2 . The experimental system performance between $t = t_1$ and $t = t_4$ matches the simulated performance in the corresponding periods in Fig. 4.21.

Between $t = t_4$ and $t = t_5$, it is shown that the PV curtailment controller can successfully match the increasing load demand, while the PV unit is regulating the microgrid frequency, and the output of the droop controlled unit is still regulated at zero. At $t = t_5$, the load demand increases beyond the available PV power. At this point, the PV unit starts regulating the output power at $P_{pv\text{-}m\text{-}p\text{-}p\text{-}t}$ and the droop controlled unit matches the rest of the load while regulating the microgrid frequency, as discussed previously in Sections 4.7.1 and 4.3.

4.8.2 Experimental Performance of the Battery Control Strategy

The microgrid performance is shown in Fig. 4.25 to experimentally validate the battery control strategy and the simulation results introduced in Section 4.7.2, and shown in Fig. 4.22. At $t = 131 \text{ s}$, the battery SOC exceeds 60% and the battery unit starts reducing the charging power to follow the reference $P_{ch\text{-}ref}$, which is determined by the charging curve in Fig. 4.8. The output power of the droop controlled unit starts decreasing accordingly. The rest of the microgrid behavior in Fig. 4.25 successfully replicates the simulated action in Fig. 4.22, during the corresponding periods of $(t < t_1)$, (t_2, t_3) , (t_3, t_4) , and $(t > t_4)$.

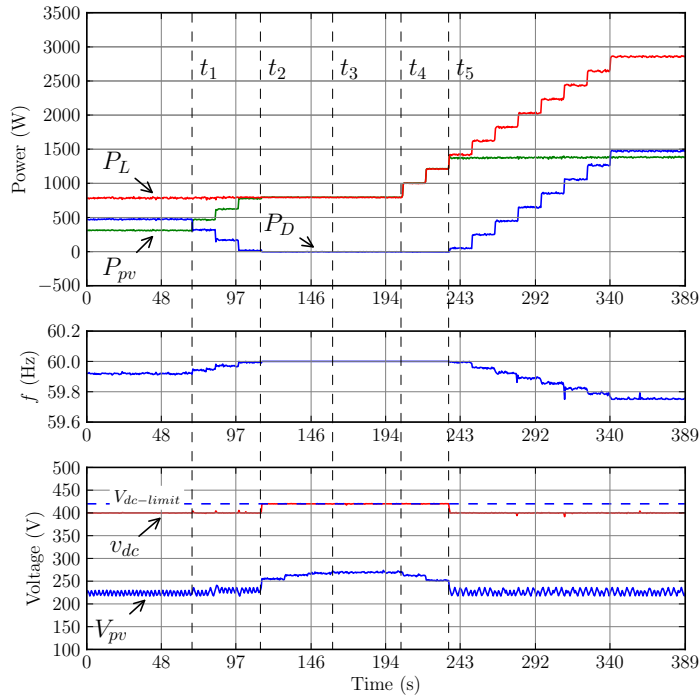


Figure 4.24: Experimental performance of the PV unit in response to variations in the available PV power.

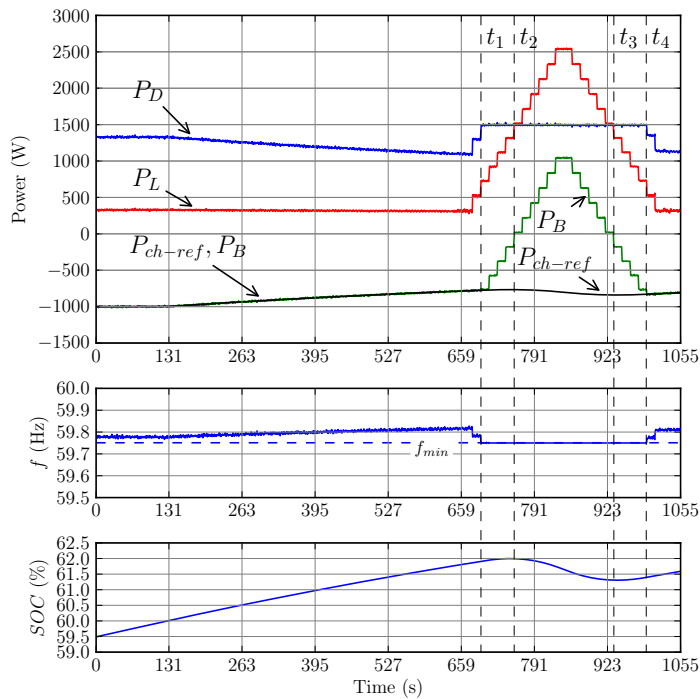


Figure 4.25: Experimental performance of the battery unit controller.

4.9 Summery and Conclusion

It is shown in this chapter that decentralized power management of PV and battery units can be achieved in a droop controlled microgrid, by employing the proposed multi-segment adaptive P/f characteristic curves at each of these units, without relying on a central management algorithm and communications. It has been demonstrated that the P/f characteristic can be configured and adjusted locally in real-time so that it either supplies the available PV power to the microgrid, or autonomously matches the varying load, and the battery charging power. On the other hand, the P/f characteristic curve at the battery unit is configured and adjusted locally in real-time, so that battery supplies power to the microgrid only when the load demand exceeds the total generation in the microgrid. Otherwise, the battery unit either stays floating, or charges the battery at a rate that is determined locally based on the battery SOC and the load/generation conditions. The decentralized power management has been demonstrated using simulation and, also, with experiments on a 3 KVA prototype microgrid.

Enhanced Reactive Power Sharing in Droop Controlled Microgrids – Part I: Adaptive Virtual Impedances

5.1 Introduction

In this chapter, a secondary control strategy is proposed to enhance the accuracy of reactive power sharing in an islanded microgrid. In the proposed strategy, communication is utilized to facilitate the tuning of adaptive virtual impedances in order to compensate for the mismatch in voltage drops across feeders. Once the virtual impedances are tuned for a given load operating point, the strategy will result in accurate reactive power sharing even if communication is disrupted. If the load changes while communication is unavailable, the sharing accuracy is reduced, but the proposed strategy will still outperform the conventional droop control method. In addition, the reactive power sharing accuracy based on the proposed strategy is immune to the time delay in the communication channel. The sensitivity of the tuned controller parameters to changes in the system operating point is also explored. The net control action of the adaptive virtual impedances is demonstrated to have a negligible effect on the microgrid bus voltage. The control strategy is straightforward to implement and does not require knowledge of the feeder impedances. The feasibility and effectiveness of the proposed strategy are validated using simulation and experimental results from a prototype microgrid.

In Section 5.2, an overview of the system structure is presented along with the problem of reactive power sharing using conventional droop control. The proposed controller is introduced in 5.3 along with a discussion of the controller sensitivity to the operating point and discussion of the communication mechanism. A small-signal model of the tuning control loop is developed in Section 5.4. Simulation and experimental results based on the proposed strategy are presented in Sections 5.5 and 5.6, respectively, followed by concluding remarks in Section 5.7.

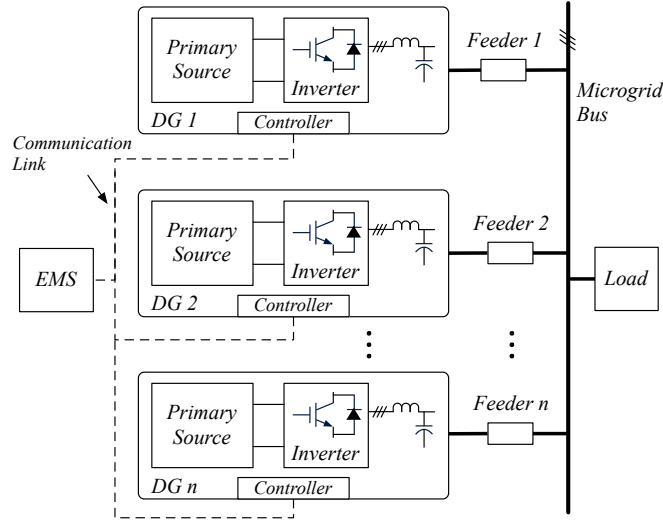


Figure 5.1: Islanded microgrid with communication links to an Energy Management System (EMS).

5.2 Islanded Microgrid Structure and Control

5.2.1 Islanded Microgrid Structure

The structure of an islanded microgrid is shown in Fig. 5.1. Each DG unit is connected to the microgrid bus through a feeder. The loads connected to the microgrid bus are lumped into a single load. The focus in this paper is on the fundamental real and reactive power sharing, as in [74] and [78], and therefore only linear loads are considered. Each DG unit consists of a primary energy source, a three-phase inverter, and an LC filter. The feeder impedance includes the impedances of the interface inductor, isolation transformer, and the impedance of the feeder cables.

The local controllers can communicate information, such as real power and reactive power measured at the DG unit output, to the central energy management system (EMS) over a communication link. Since the proposed strategy only requires that the local controllers exchange data periodically at a slow rate, low-bandwidth communication links are considered adequate for this application. The local controller consists of the power controller, which generates the output voltage reference, and the voltage controller to track the voltage reference. Conventional frequency and voltage droop control is implemented in the controller as follows:

$$\omega = \omega_o - mP_m \quad (5.1)$$

$$V^* = V_o - nQ_m \quad (5.2)$$

where ω and V^* are the frequency and voltage magnitude references, respectively. P_m and Q_m are the real and reactive powers measured at the output of the DG unit, respectively, and are filtered to extract the fundamental power components. m is the frequency droop coefficient and n is the voltage droop coefficient. It is worth mentioning that to

facilitate the utilization of the droop control concept in low voltage distribution networks, a physical and/or a virtual interface inductor is commonly added in line at the output of the DG unit in an attempt to reduce the coupling between the real and the reactive power flows.

5.2.2 Reactive Power Sharing Analysis

The effect of the feeder impedance mismatch on the reactive power sharing is examined in this section by analyzing the voltage drop across the feeders. The voltage drop across the feeder impedance can be approximated as in [70, 74]

$$\Delta V \approx \frac{XQ + RP}{V_o} \quad (5.3)$$

where X and R represent the feeder reactance and resistance, P and Q represent the active and reactive power flowing through the feeder, respectively, and V_o is the DG unit nominal output voltage. Without loss of generality, a two unit microgrid as shown in Fig. 5.2 is used as a case study in this section. The voltage drops across feeder 1 and feeder 2 in Fig. 5.2 can be approximated by

$$\Delta V_1 \approx \frac{X_1 Q_1 + R_1 P_1}{V_o} \quad (5.4)$$

$$\Delta V_2 \approx \frac{X_2 Q_2 + R_2 P_2}{V_o} \quad (5.5)$$

The mismatch in the feeder impedances is given by

$$\Delta X = X_1 - X_2 \quad (5.6)$$

$$\Delta R = R_1 - R_2 \quad (5.7)$$

Considering (5.6) and (5.7), the network as seen from *DG 1* is shown in Fig. 5.3, where V_1^* and V_2^* represent the voltage references generated by the conventional droop controllers. X and R are the reactance and resistance of feeder 2 (X_2 and R_2), respectively, that are chosen as references to calculate the mismatch between feeder impedances. X_v and R_v stand for the effect of any virtual impedance that might be implemented in the controller. δV_1^* represents the net change in the voltage reference that could be added by the controller, as will be seen later, to enhance the performance of the conventional droop control. Note that with proper design of the voltage controller, the voltages controlled and measured at the output filter capacitors of the DG units are assumed to match the references $V_1^* + \delta V_1^*$ and V_2^* at the steady state. P_1 , Q_1 , P_2 , and Q_2 are the powers that can be measured at the outputs of the DG units. Based on Fig. 5.3 and (5.3)

$$\begin{aligned} \Delta V_1 &\approx \frac{(X + \Delta X)Q_1 + (R + \Delta R)P_1}{V_o} \\ &= \frac{XQ_1 + RP_1}{V_o} + \frac{\Delta XQ_1 + \Delta RP_1}{V_o} \\ &= \overline{\Delta V_1} + \delta V_1 \end{aligned} \quad (5.8)$$

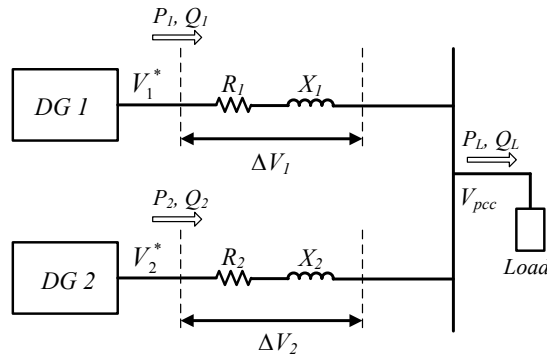
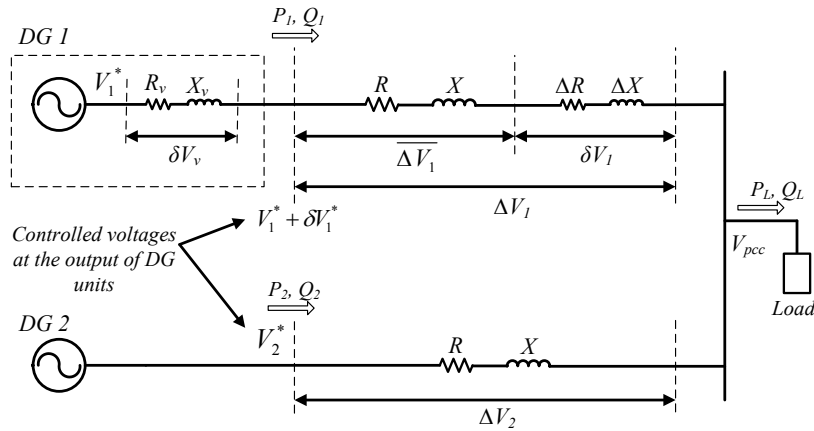


Figure 5.2: Simplified model of the microgrid with two inverters.

Figure 5.3: The detailed network model as seen from *DG 1*.

where, as shown in Fig. 5.3, ΔV_1 is the total voltage drop across the Feeder 1 impedance represented by $X + \Delta X$ and $R + \Delta R$. $\overline{\Delta V_1}$ is the voltage drop across Feeder 1 due to the reference reactance and resistance, X and R . Accordingly, since $P_1 = P_2$, then $\overline{\Delta V_1} = \Delta V_2$, and δV_1 indicates the voltage drop mismatch between Feeder 1 and Feeder 2 due to the mismatch in feeder impedances, ΔX and ΔR . The mismatch in the feeder impedances (ΔX , ΔR), and hence, in the voltage drop across the feeders (δV_1) results in errors in reactive power sharing between the units as detailed in [65, 70, 71, 74, 97].

However, identical feeders result in accurate sharing only if the units have the same power ratings, and correspondingly, the same droop coefficients. When the units have different power ratings, even though the feeder impedances may match, the unit supplying more power will result in a higher voltage drop across its feeder, in comparison to the unit supplying less power. The worst case may occur when the unit with the higher power rating is connected to the feeder with higher impedance.

For units with different power ratings, the feeder resistance and reactance must be

made inversely proportional to the real and reactive power ratings of the respective DG unit to achieve accurate reactive power sharing [65, 74, 75]. In other words, the following should be true

$$R_1 P_{r1} = R_2 P_{r2} \quad (5.9)$$

$$X_1 Q_{r1} = X_2 Q_{r2} \quad (5.10)$$

where P_{r1} , Q_{r1} are the real and reactive power ratings of Unit 1, and P_{r2} , Q_{r2} are those of Unit 2. Consequently, the voltage drop difference that can cause inaccurate reactive power sharing is not determined by the direct mismatch in the feeder impedances as in (5.7) and (5.6). Using the Unit 2 feeder as the reference again ($R = R_2$ and $X = X_2$), R_1 and X_1 can be expressed as

$$R_1 = \frac{P_{r2}}{P_{r1}} R + \Delta R \quad (5.11)$$

$$X_1 = \frac{Q_{r2}}{Q_{r1}} X + \Delta X \quad (5.12)$$

The conditions in (5.9) and (5.10), and stated in [65, 74, 75], are intuitive and based on the fact that they will result in the same voltage drop across feeders regardless of the different power ratings. To clarify this point mathematically, the voltage drops across the feeders under (5.11) and (5.12), are given by

$$\Delta V_2 \approx \frac{XQ_2 + RP_2}{V_o} \quad (5.13)$$

$$\begin{aligned} \Delta V_1 &\approx \frac{(\frac{Q_{r2}}{Q_{r1}} X + \Delta X)Q_1 + (\frac{P_{r2}}{P_{r1}} R + \Delta R)P_1}{V_o} \\ &= \frac{(\frac{Q_{r2}}{Q_{r1}} X)Q_1 + (\frac{P_{r2}}{P_{r1}} R)P_1}{V_o} + \frac{\Delta X Q_1 + \Delta R P_1}{V_o} \\ &= \overline{\Delta V_1} + \delta V_1 \end{aligned} \quad (5.14)$$

If the conditions in (5.9) and (5.10) are satisfied, i.e., $\Delta R=0$ and $\Delta X=0$, then (5.14) can be reduced to

$$\Delta V_1 \approx \frac{(\frac{Q_{r2}}{Q_{r1}} X)Q_1 + (\frac{P_{r2}}{P_{r1}} R)P_1}{V_o} = \overline{\Delta V_1} \quad (5.15)$$

Given the fact that real power sharing using frequency droop is always accurate, i.e. $\frac{P_{r2}}{P_{r1}} = \frac{P_2}{P_1}$, (5.15) can be rewritten as

$$\Delta V_1 \approx \frac{(\frac{Q_{r2}}{Q_{r1}} X)Q_1 + RP_2}{V_o} \quad (5.16)$$

Examining (5.13) and (5.16),

$$\Delta V_1 = \Delta V_2 \Leftrightarrow \frac{Q_2}{Q_1} = \frac{Q_{r2}}{Q_{r1}} \quad (5.17)$$

Therefore, regardless of the power ratings of different units, compensating for any mismatch in the voltage drop across feeders (δV_1) will result in accurate reactive power sharing [65, 70, 71, 74, 97].

One solution to this problem is to compensate for the effect of ΔX and ΔR by using a virtual impedance of $X_v = -\Delta X$ and $R_v = -\Delta R$. The drawback of this technique is that it requires knowledge of the feeder impedances which is often not readily available.

The other way to resolve this issue, as proposed in this thesis, is to employ voltage drop compensation instead of matching impedances. Without loss of generality, the case where both units have the same rating is considered in this analysis. When using conventional droop control only, V_1^* and V_2^* can be represented as

$$V_1^* = V_{pcc} + \overline{\Delta V_1} + \delta V_1 \quad (5.18)$$

$$V_2^* = V_{pcc} + \Delta V_2 \quad (5.19)$$

The effect of the voltage drop mismatch due to ΔX and ΔR on reactive power sharing can be compensated by modifying the voltage reference V_1^* as follows:

$$V_1^* + \delta V_1^* = V_{pcc} + \overline{\Delta V_1} + \delta V_1 \quad (5.20)$$

assuming that a controller can be designed such that at any time

$$\delta V_1^* = \delta V_1 \quad (5.21)$$

Consequently, equation (5.20) can be reduced to

$$V_1^* = V_{pcc} + \overline{\Delta V_1} \quad (5.22)$$

Although ΔV_1 will still not be equal to ΔV_2 , the effect of δV_1 on the reactive power sharing will be compensated. For example, every time δV_1 increases due to an increase in load, the controller will increase δV_1^* accordingly. This can be implemented by using an adaptive virtual impedance and communication as proposed in the next section.

5.3 Proposed Control Strategy

5.3.1 Proposed Controller

The feasibility of the condition in (5.21) can be further investigated by using the principle of virtual impedance and the approximation in (5.3). Considering the use of a virtual impedance to generate the voltage δV_1^* , from Fig. 5.3

$$\delta V_1^* = -\delta V_v \quad (5.23)$$

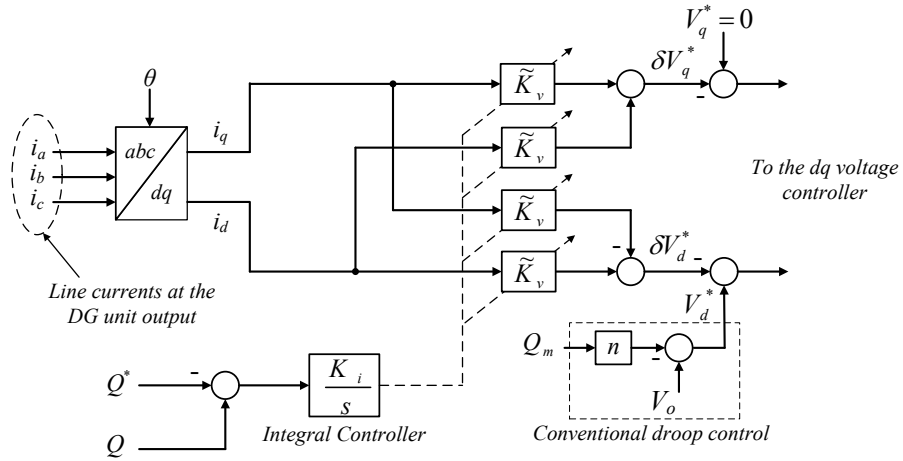


Figure 5.4: The proposed adaptive virtual impedance controller.

Using the approximation in (5.3), the condition in (5.21) can be approximated by

$$-\frac{X_v Q_1 + R_v P_1}{V_o} \approx \frac{\Delta X Q_1 + \Delta R P_1}{V_o} \quad (5.24)$$

Satisfying (5.24) by matching the impedances is not practical as stated in Section 5.2. However, (5.24) can be simplified by setting

$$\tilde{K}_v = X_v = R_v \quad (5.25)$$

where \tilde{K}_v is called the virtual impedance variable. The condition in (5.25) will result in a feasible controller as will be shown later in this section. Substituting (5.25) in (5.24) and rearranging

$$\tilde{K}_v \approx -\frac{\Delta X Q_1 + \Delta R P_1}{Q_1 + P_1} \quad (5.26)$$

As can be seen from (5.26), for any given values of ΔX , ΔR , P_1 and Q_1 , there is a corresponding \tilde{K}_v that matches the voltages to meet the condition in (5.21). However, (5.26) still cannot be used to implement the controller because the feeder discrepancies (ΔX and ΔR) are unknown. Nevertheless, the main goal of (5.26) is to show that one value for the virtual reactance and resistance can satisfy the condition in (5.21).

If the proper reference for Q_1 is available to the local controller, the variable \tilde{K}_v can be tuned to the required virtual impedance value as proposed in this work. To achieve this, each unit shares its actual reactive power load with the microgrid Energy Management System (EMS) over the communication link. The EMS calculates the proper share for each unit based on its rating and the total load, and sends it back to each unit along with a controller enable signal (EN).

Consequently, each unit will utilize the received reactive power share reference Q^* to adaptively tune \tilde{K}_v . The reference Q^* is calculated based on the total reactive power

demand in the microgrid ($Q_L = Q_1 + \dots + Q_N$). Therefore, when the output reactive power at each unit starts changing during the tuning process, Q_L remains the same unless the total reactive power demand changes. In other words, the reference Q^* received at each unit remains unaffected by the action of the local tuning closed loop. When the total demand changes, Q^* will be adjusted accordingly, and the local controllers start taking action as in any supervisory control system. Since the tuning loop is closed locally at each DG unit, and not through communications, the sharing accuracy at steady state is unaffected by time delays in the communication channels, which is not the case with the techniques in [72, 73, 77].

Once \tilde{K}_v is tuned for a given load condition, accurate reactive power sharing will continue even if the communication channel becomes unavailable, as long as the load does not change. Even if the load changes while communication is disrupted, the proposed strategy will still outperform the conventional droop control, as will be shown in Sections 5.5 and 5.6.

The controller proposed to tune the virtual impedance variable \tilde{K}_v is shown in Fig. 5.4. A simple integral control loop can be used to tune \tilde{K}_v by regulating Q indirectly to match Q^* . The virtual impedance is implemented in the dq-frame where θ represents the phase angle of the unit output voltage. Note that the objective of the controller is not to regulate the reactive power directly but to tune the virtual impedance to a value that compensates for the effect of the feeder voltage drop mismatch on the reactive power sharing. Therefore, once the virtual impedance is tuned for the current load conditions it will result in accurate sharing, and in reasonable sharing if the load changes and communication is disrupted. More details regarding the communication loss and delay will be discussed in Sections 5.3.3, 5.5, and 5.6. For a microgrid of two DG units, the controller can be implemented in one unit only or in both units. In general, for a microgrid with two or more DG units, the controller implemented at each unit tunes the virtual impedance in the same way as described previously for *DG 1*.

The integral control is chosen such that the integration time is much longer than the information update period; e.g., the integration time $T_i = 1/K_i$ is chosen to be 200 s·var/ Ω , versus an information update period of 0.2 s (see Table 5.1). Therefore, the time delay in the received Q^* sample, due to the fact that reference Q^* is updated periodically and held constant between updates, will have no effect on the reactive power sharing at steady state. This time delay is called the information update delay. Moreover, the tuning loop is slow enough that the interaction is negligible with the microgrid dynamics, which are dominated by the power low-pass filter dynamics [85, 98]. A detailed small-signal model of the virtual impedance tuning loop is developed and presented in Section 5.4.

Note that the reference Q^* is calculated by the EMS based on the total reactive power load in the microgrid, therefore Q^* stays unchanged during the tuning action unless the total load changes. This part of the strategy can be considered to be a supervisory control system, which reacts only when the total load in the microgrid changes (a disturbance).

5.3.2 Tuned Controller Sensitivity to Operating Points

The proposed controller is designed so that the tuned virtual impedance is held at its most recent value after a communication failure occurs, as will be illustrated in the following

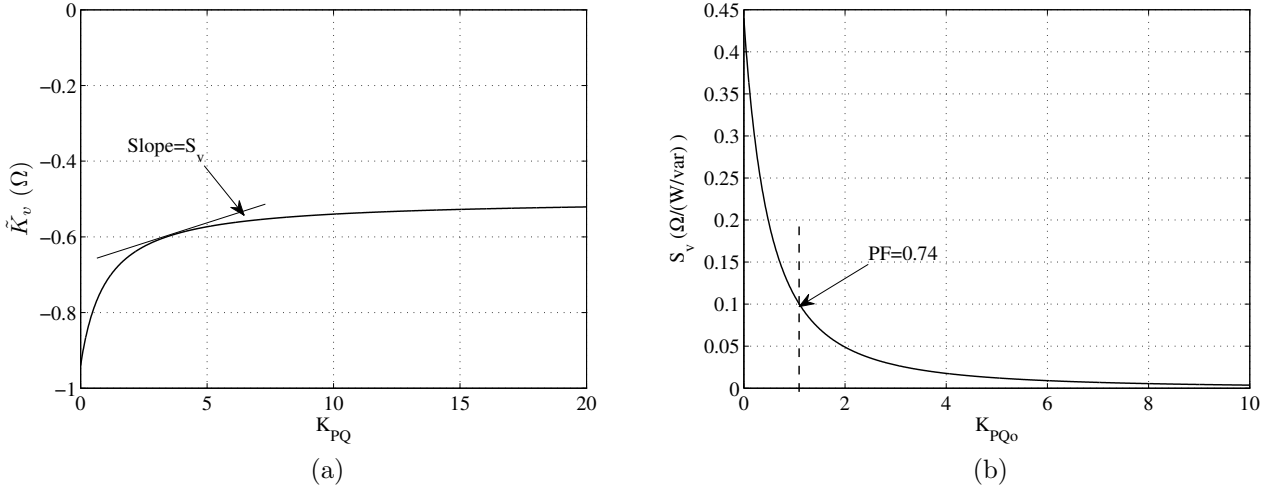


Figure 5.5: \tilde{K}_v sensitivity based on the parameters of DG units 1 and 2 from Table 5.1 ($\Delta X = 0.94\Omega$, $\Delta R = 0.5\Omega$). (a) \tilde{K}_v as a function of the load operating point. (b) S_v in the considered operating range.

section. If the operating point remains unchanged after the communication failure, the sharing error will remain zero since the controller is already tuned for that operating point. However, an operating point change will result in a sharing error because \tilde{K}_v can no longer adapt to the new operating point. The change needed in \tilde{K}_v to adapt to the new operating point defines the sensitivity of \tilde{K}_v with respect to the change in the operating point. To gain insight into the \tilde{K}_v sensitivity, the approximated relation in (5.26) is used. Rearranging the terms in (5.26)

$$\tilde{K}_v \approx -\frac{\Delta X + \Delta R(P/Q)}{1 + (P/Q)} \quad (5.27)$$

It is clear from (5.27) that \tilde{K}_v depends on the ratio P/Q rather than on the value of P or Q separately. Therefore, any new operating point with the same ratio P/Q (the same power factor) will result in the same \tilde{K}_v . Define the variable K_{PQ} as P/Q . The nonlinear relation in (5.27) can be linearized around the operating point as follows:

$$\tilde{K}_v \approx \tilde{K}_{v_o} + \left. \frac{\partial \tilde{K}_v}{\partial K_{PQ}} \right|_{K_{PQ_o}} \Delta K_{PQ} \quad (5.28)$$

where \tilde{K}_{v_o} is the virtual impedance variable tuned at the operating point and K_{PQ_o} is the associated P/Q ratio. The slope of \tilde{K}_v in (5.28) is defined as the sensitivity S_v around the operating point. Therefore S_v can be written as

$$\begin{aligned} S_v &= \left. \frac{\partial}{\partial K_{PQ}} \left(\frac{\Delta X + \Delta R K_{PQ}}{1 + K_{PQ}} \right) \right|_{K_{PQ_o}} \\ &= \frac{-(1 + K_{PQ_o})\Delta R + (\Delta X + \Delta R K_{PQ_o})}{(1 + K_{PQ_o})^2} \end{aligned} \quad (5.29)$$

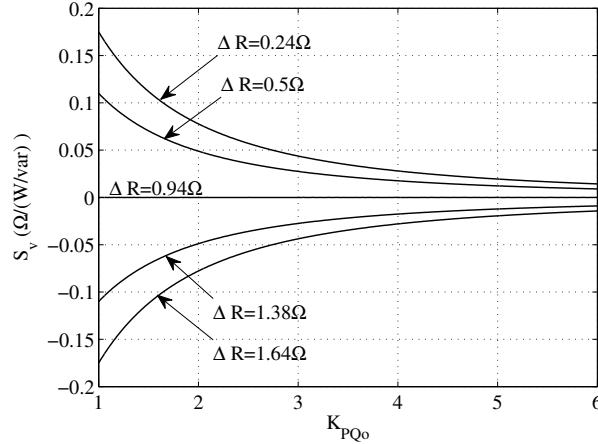
Figure 5.6: Sensitivity of \tilde{K}_v for different values of ΔR ($\Delta X = 0.94\Omega$).

Table 5.1: System Parameters

Description	Parameter	Value
DG Unit Rating	S	1 kVA
Nominal Voltage	V_o	208 V_{l-l}
Inverters Filter	L_f, C_f	5mH, 75 μ F
Switching Frequency	f_s	10 kHz
Frequency Droop Coefficient	m	0.00105 rad/(s·W)
Voltage Droop Coefficient	n	0.00250 V/var
Feeder 1 Impedance	$R_1 + jX_1$	1.6 + j 2.450 Ω
Feeder 2 Impedance	$R_2 + jX_2$	1.1 + j 1.508 Ω
Feeder 3 Impedance (simulation)	$R_3 + jX_3$	0.8 + j 1.130 Ω
Total Load (simulation)	P_L, Q_L	1215 W, 1030 var
Total Load (experimental)	P_L, Q_L	1170 W, 1330 var
Q* setpoint update rate	f_c	5 Hz
Integral Control gain	K_i	0.005 Ω /(s·var)
LPF Time Constant	T	0.032 s

To gain insight into the sensitivity of \tilde{K}_v to the operating point, feeders 1 and 2 from Table 5.1 are considered, where $\Delta X = 0.94\Omega$ and $\Delta R = 0.5\Omega$. As can be seen from Fig. 5.5a and equation (5.27), when K_{PQ} is zero (PF=0) then \tilde{K}_v equals $-\Delta X$. However, when K_{PQ} approaches infinity (PF=1) \tilde{K}_v equals $-\Delta R$. Consequently, for high K_{PQ} values (high power factors) the sensitivity of \tilde{K}_v is low as shown in Fig. 5.5b. From Fig. 5.5b, $|S_V|$ is less than 0.1 for power factors higher than 0.74 and \tilde{K}_V changes from -0.646Ω to -0.521Ω when K_{PQ} changes from 2 (PF=0.89) to 20 (PF=0.998). To examine the effect of different impedance pairs, ΔX is fixed at 0.94Ω and ΔR is changed as shown in Fig. 5.6. Again, Fig. 5.6 shows low sensitivity for high K_{PQ} (high PF), e.g., $|S_V|$ is less than 0.1 for K_{PQ} higher than 1.65 (PF=0.85).

5.3.3 Information Management Structure

The EMS periodically polls the inverters for their internally measured reactive power output. The update rate for the reactive power data can be chosen based on the specifications of the available communication link. The collected reactive power measurements

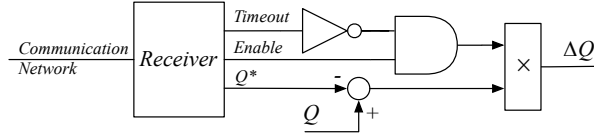


Figure 5.7: Reactive power setpoint enable logic in each local controller.

are then summed and weighted such that each inverter is responsible for sharing the reactive power in proportion to its rating. The resulting values are then passed back to the units as setpoints for the tuning control loop.

The receiver is capable of detecting a communication time-out, in which case the control loop is disabled and the integrator output will remain constant until a valid setpoint is again received. The timeout/enable logic is shown in Fig. 5.7. Note that when the EMS detects a communication timeout from one DG unit it blocks further setpoint updates to all the DG units until communication is restored. Since the updates are not sent to the remaining DG units their timeout/enable logic disables the tuning control loops until communication is restored. A binary enable signal is also sent along with the setpoint to allow for remote enabling and disabling of the tuning control loop.

5.4 Small-Signal Model of the Virtual Impedance Tuning Loop

The real and reactive power flow can be described as in [94]

$$P = \frac{1}{R_t^2 + X_t^2} (R_t V^{*2} - R_t V^* V_{pcc} \cos \delta + X_t V^* V_{pcc} \sin \delta) \quad (5.30)$$

$$Q = \frac{1}{R_t^2 + X_t^2} (X_t V^{*2} - X_t V^* V_{pcc} \cos \delta - R_t V^* V_{pcc} \sin \delta) \quad (5.31)$$

where the angle δ is the power angle. R_t and X_t represent the resistive and inductive components of the total feeder impedance, respectively, including the virtual impedances as follows:

$$R_t = R + \tilde{K}_v \quad (5.32)$$

$$X_t = X + \tilde{K}_v \quad (5.33)$$

where \tilde{K}_v is the virtual impedance variable generated by the controller as

$$\tilde{K}_v = \frac{K_i}{s} (Q - Q^*) \quad (5.34)$$

Linearizing equations (5.30), (5.31), (5.34), along with the frequency and voltage droop equations (5.1) and (5.2), around an operating point

$$\begin{aligned} \Delta P &= \left(\frac{\partial P}{\partial V^*} \right) \Delta V^* + \left(\frac{\partial P}{\partial \delta} \right) \Delta \delta + \left(\frac{\partial P}{\partial \tilde{K}_v} \right) \Delta \tilde{K}_v \\ &= K_{pv} \Delta V^* + K_{p\delta} \Delta \delta + K_{pk} \Delta \tilde{K}_v \end{aligned} \quad (5.35)$$

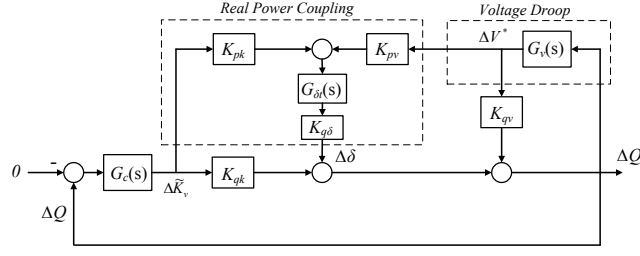


Figure 5.8: Linearized model.

$$\begin{aligned}\Delta Q &= \left(\frac{\partial Q}{\partial V^*}\right)\Delta V^* + \left(\frac{\partial Q}{\partial \delta}\right)\Delta\delta + \left(\frac{\partial Q}{\partial \tilde{K}_v}\right)\Delta\tilde{K}_v \\ &= K_{qv}\Delta V^* + K_{q\delta}\Delta\delta + K_{qk}\Delta\tilde{K}_v\end{aligned}\quad (5.36)$$

$$\Delta\tilde{K}_v = \frac{K_i}{s}\Delta Q = G_c(s)\Delta Q \quad (5.37)$$

$$\Delta\omega = \frac{-m}{Ts + 1}\Delta P \quad (5.38)$$

$$\Delta V^* = \frac{-n}{Ts + 1}\Delta Q = G_v(s)\Delta Q \quad (5.39)$$

where K_{pv} , $K_{p\delta}$, K_{pk} , K_{qv} , $K_{q\delta}$, K_{qk} are calculated around the operating point, and T is the time constant of the low-pass filter used in the P and Q measurement channels. Considering that $\Delta\omega = s\Delta\delta$, (5.38) can be rewritten as

$$\Delta\delta = \frac{-m}{s(Ts + 1)}\Delta P = G_\delta(s)\Delta P \quad (5.40)$$

Substituting for ΔP from (5.40) in (5.35), $\Delta\delta$ is given by

$$\Delta\delta = G_{\delta t}(s)[K_{pv}\Delta V^* + K_{pk}\Delta\tilde{K}_v] \quad (5.41)$$

where

$$G_{\delta t}(s) = \frac{G_\delta(s)}{1 - K_{p\delta}G_\delta(s)} \quad (5.42)$$

Equation (5.41) represents the coupling of the reactive power controller with the real power control dynamics. Using (5.36), (5.37), and (5.41), a block diagram of the system with the proposed controller can be realized as in Fig. 5.8. This model can be further simplified as in Fig. 5.9. Accordingly, the characteristic equation of the system is given by

$$1 - K_{qv}G_v(s) - K_{pv}K_{q\delta}G_v(s)G_{\delta t}(s) - K_{qk}G_c(s) - K_{pk}K_{q\delta}G_c(s)G_{\delta t}(s) = 0 \quad (5.43)$$

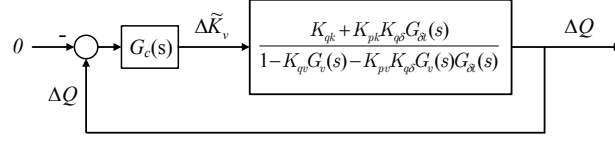
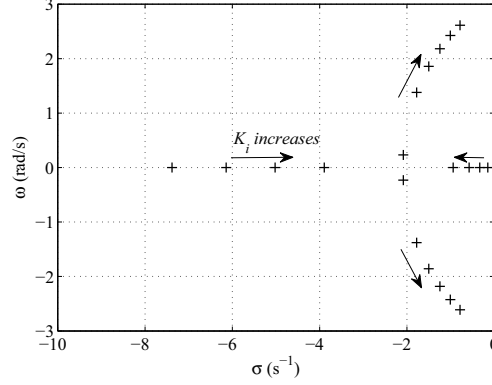


Figure 5.9: Simplified block diagram of the linearized model.

Figure 5.10: Dominant root trajectory when K_i increases.

Substituting for $G_c(s)$, $G_v(s)$, $G_δ(s)$ and $G_{δt}(s)$ from equations (5.37), (5.39), (5.40) and (5.42), respectively, the characteristic equation is given as

$$a_4 s^4 + a_3 s^3 + a_2 s^2 + a_1 s + a_0 = 0 \quad (5.44)$$

where

$$a_4 = T^2 \quad (5.45)$$

$$a_3 = 2T + nK_{qv}T - K_{qk}K_iT^2 \quad (5.46)$$

$$a_2 = 1 + mK_{pδ}T + nK_{qv} - 2K_{qk}K_iT \quad (5.47)$$

$$a_1 = mK_{pδ} + nmK_{qv}K_{pδ} - nmK_{pv}K_{qδ} - K_{qk}K_i(1 + mK_{pδ}T) + K_{pδ}K_i mTK_{qδ} \quad (5.48)$$

$$a_0 = -K_{qk}K_i mK_{pδ} + K_{pk}K_i mK_{qδ} \quad (5.49)$$

The characteristic equation (5.44) is used to calculate the poles of the system around the considered operating points for different values of K_i . Consequently, the integral gain K_i is chosen so that the dominant poles result in much slower dynamics in comparison to the reference Q^* update rate. Therefore, time delays in communication have a minor effect on the system transients when the total reactive load changes significantly (See Section 5.3.1). Considering the system parameters in Table 5.1, the dominant root trajectory, when K_i is changed from 0.001 to 0.01 with a step of 0.001 $\Omega/(s\text{-var})$, is shown in Fig. 5.10.

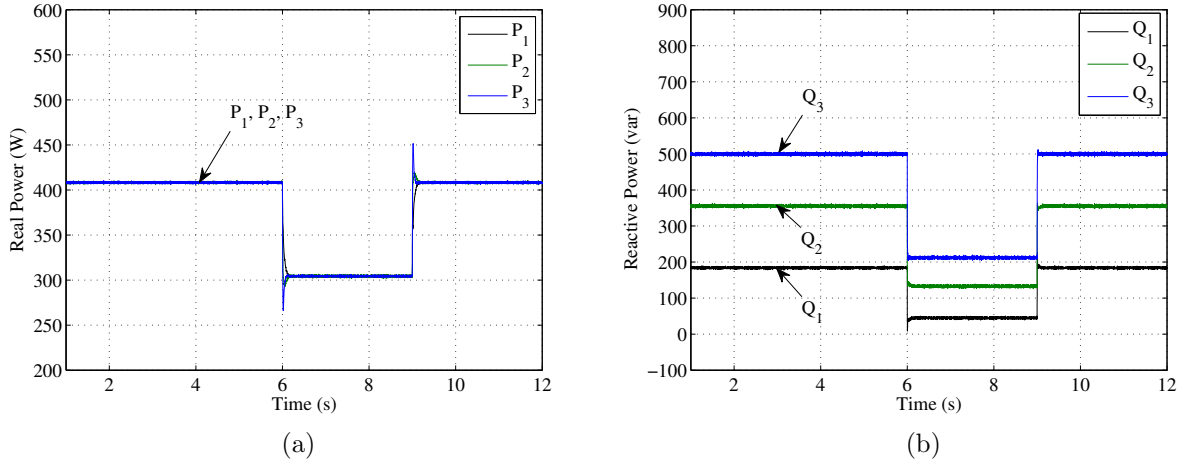


Figure 5.11: Simulated performance of conventional droop control. (a) Real power. (b) Reactive power.

5.5 Simulation Results

A microgrid with three DG units is simulated in the PSCAD/EMTDC environment to validate the proposed control strategy, and to demonstrate the feasibility of the proposed controller for microgrids with more than two units. The microgrid system parameters are shown in Table 5.1. The three DG units are identical in rating and filter parameters to highlight the accuracy of the proposed strategy in the presence of mismatched feeder impedances. The discrepancy in the feeder impedances is chosen to be significant in comparison to values used in the existing literature [72, 74, 78].

To evaluate the performance of the proposed system a percentage accuracy measure Q_{er} is defined as in [78]

$$Q_{er-i}\% = \frac{Q_i - Q_i^*}{Q_i^*} \times 100 \quad (5.50)$$

where Q_i is the reactive power measured at the output of unit i and Q_i^* is the desired reactive power share that unit i should ideally supply. Simulation scenarios that validate the performance of the proposed controller are presented in the following subsections.

Performance of Conventional Controller

The performance of the system using only conventional droop control is illustrated in Fig. 5.11 for two different loads. The total reactive power load is changed between 1030 var and 388 var while the real power load is changed between 1215 W and 910 W. These load settings represent a larger change in reactive power load as compared to the change in the real power load to show the low sensitivity of the tuned virtual impedance to the P/Q ratio factor (K_{PQ}) of the operating point, as discussed in Section 5.3.2. Also, this will help evaluate the control strategy for a wide range of load power factors, from 0.76 for the higher load to 0.92 for the lower load.

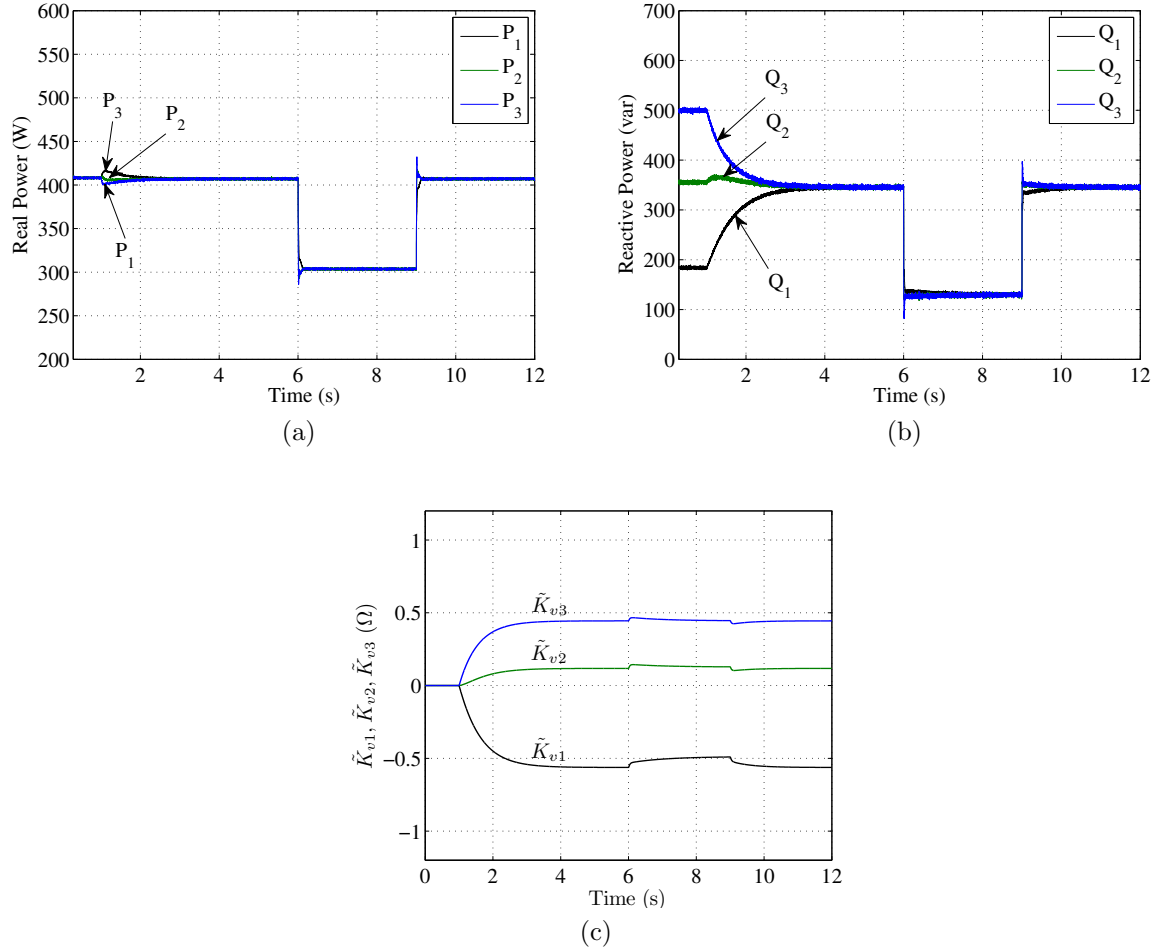


Figure 5.12: Simulated performance of the proposed controller (activated at $t = 1$ s). (a) Real Power. (b) Reactive Power. (c) Real-time tuning of the virtual impedance variables.

From Fig. 5.11, the reactive power sharing accuracy under conventional droop control is as poor as 45% for unit 3 and 44% for unit 1 while it is 2.9% for unit 2, calculated at the higher load operating point.

Performance of the Proposed Controller

The performance of the proposed controller is demonstrated in Fig. 5.12. The controller is enabled at $t = 1$ s which reduces the reactive power sharing error to zero in 2 seconds as can be seen in Fig. 5.12b. Also, Fig. 5.12a shows that the controller action has only a small transient effect on the real power supplied by each unit. Moreover, Fig. 5.12c illustrates the low sensitivity of the tuned virtual impedances to a change in the operating point.

The behavior of the microgrid bus voltage (V_{pcc}), when the controller is enabled at $t = 1$ s, is shown in Fig. 5.13. As can be seen, the voltage drop introduced by the proposed controller is negligible (0.0015 pu). This is due to the fact that controllers reduce the total

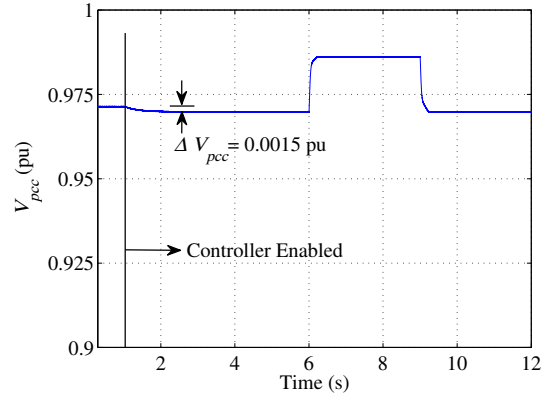


Figure 5.13: The behavior of the microgrid bus voltage (V_{pcc}) when the controller is enabled at $t=1$ s.

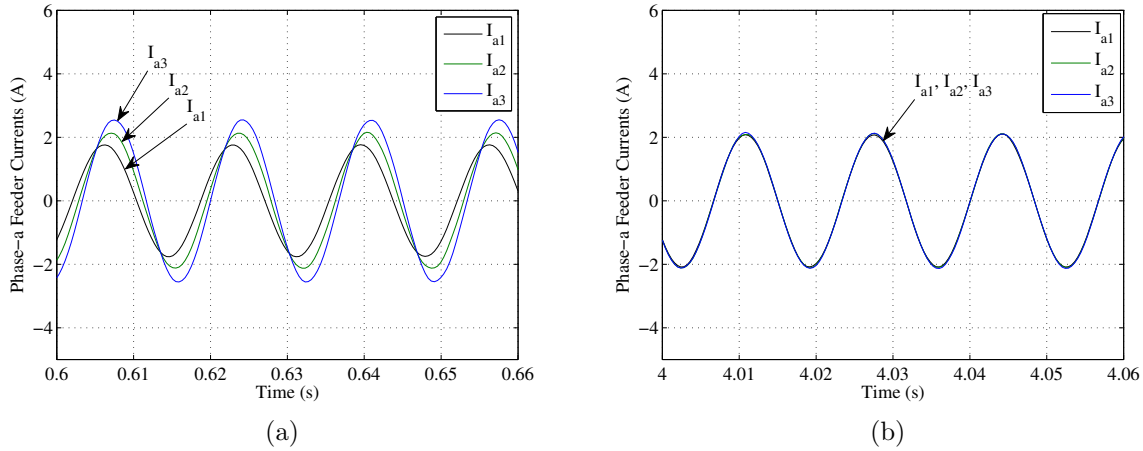


Figure 5.14: Simulated feeder currents. (a) Under conventional control (before enabling the controller). (b) Under the proposed control strategy.

feeder impedance for the unit with the higher physical impedance (Unit 1), and increase it for the unit with the lower physical impedance (Units 2 and 3), as can be noticed from Fig. 5.12c. The latter voltage change, when the load stepped down, is mainly due to the change in the voltage drop across the feeders and the conventional voltage droop action, since the virtual impedances did not change significantly (see Fig. 5.12c) when the load changed.

Fig. 5.14 demonstrates the enhancement in the current sharing accuracy provided by the proposed control strategy as compared to the conventional droop control.

The Effect of the Communication and Information Update Delays

To show the main concept of the controller, two factors were neglected in the simulation of Fig. 5.12. The first is the time delay mismatch among the communication channels, and the second is the information update delay. In Fig. 5.12, the load is intentionally

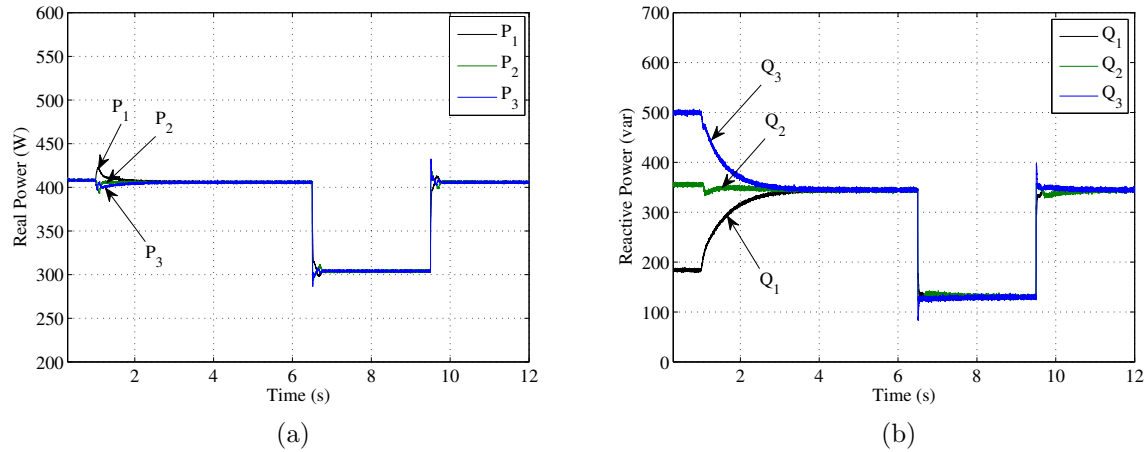


Figure 5.15: Simulated performance of the controller considering the effects time delay mismatches among the communication channels and the information update delay. (a) Real power. (b) Reactive Power.

changed at the same moment Q^* is updated so there is no information update delay. A second simulation is performed to include these effects. A delay of 0.1 s and 0.05 s has been included in the communication links of units 2 and 3, respectively, while no delay is considered for unit 1 to emphasize the delay time mismatch. Also, the load changes have been introduced exactly in the middle between the Q^* update times, which results in a 0.1 s information update delay. Note that the time delay is significant with respect to the 0.2 s update rate of Q^* . Taking into account these changes, the performance of the proposed control strategy is shown in Fig. 5.15. As can be seen the information update delay and the time delay mismatch has no effect on the sharing accuracy of the proposed controller. The same time delay in the communication channels will be used for the remainder of the simulation scenarios.

Controller Performance During a Communication Disruption

The scenario of a communication failure is illustrated in Fig. 5.16. A communication failure is sensed at $t=5$ s causing a timeout signal issued by the serial receiver block (Fig. 5.7) to disable the controller. The virtual impedance variables are held at the last value before the failure occurred due to the integral action of the controller. As can be seen in Fig. 5.16a when the load changes the sharing error is still acceptable. A noticeable change in the operating point power factor from 0.76 to 0.92 is considered here to give insight into the sensitivity of the virtual impedance to a change in the load. The sharing error accuracy ($Q_{er-i}\%$) is 6.2%, -1.87%, and 1.87% for DG units 1, 2, and 3, respectively, as compared to -46.8%, 2.92% and 45.48% when using conventional droop control only. Associated feeder current waveforms for the three DG units are shown in Fig. 5.16b which demonstrate accurate sharing compared to the current waveforms in Fig. 5.14a. Finally, Fig. 5.17 shows the system transient performance during the restoration of communication at $t=9$ s. The sharing mismatch is reduced once communication

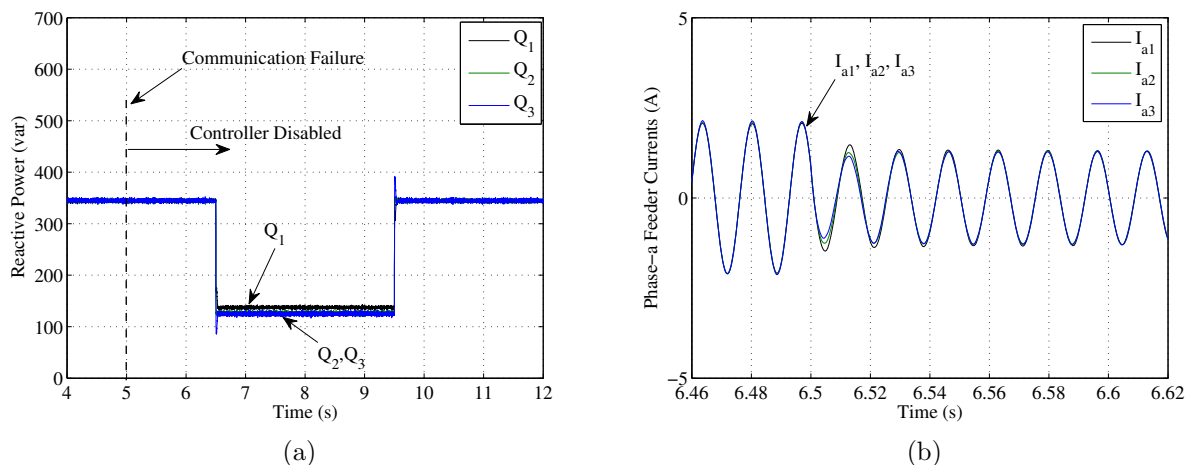


Figure 5.16: Simulated performance of the tuned controller in response to a load change after a communication failure. (a) Reactive Power. (b) Phase-a feeder currents.

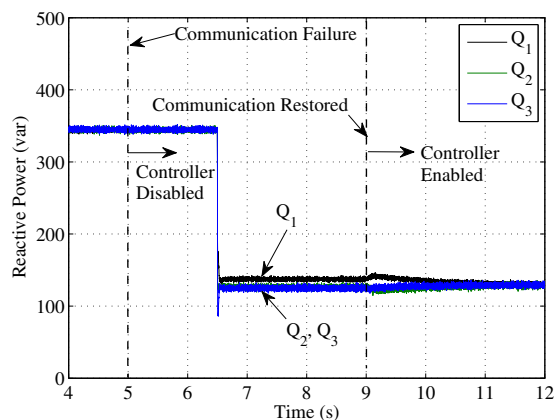


Figure 5.17: Simulated system performance during communication restoration.

is restored.

5.6 Experimental Evaluation

5.6.1 Experimental Setup

The experimental setup consists of two 3-phase inverters with Ethernet interfaces, a networked computer running the EMS software, and a load with adjustable real and reactive power levels. The primary power sources for the inverters are two Chroma 62050H power supplies. Other experimental system parameters including feeder impedances are shown in Table 5.1 for units 1 and 2.

As in the experimental work in Chapters 2-4, the inverter controllers are implemented in Simulink, compiled using the Embedded Coder toolchain, and run on Spectrum Dig-

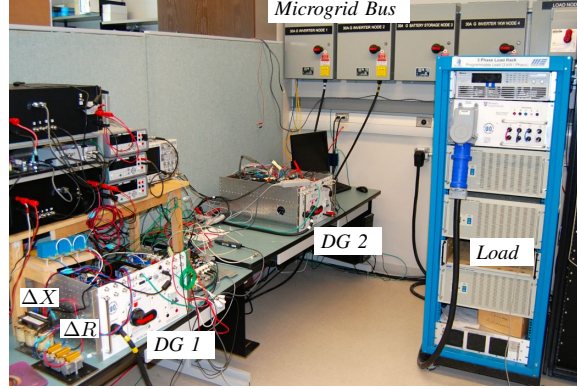


Figure 5.18: The experimental apparatus.

ital eZdsp boards containing Texas Instruments TMS320-F28335 32-bit floating-point microcontrollers. The network interfaces are implemented with Texas Instruments serial-to-Ethernet modules connected to the serial communication port of the eZdsp boards. The EMS software that receives the measured reactive powers and calculates the reactive power setpoints is programmed in the Python language and hosted on a PC running Ubuntu Linux.

A photograph of the experimental apparatus is shown in Fig. 5.18. Each unit in the prototype microgrid is connected to the bus through a 3 mH interface inductor, an isolating transformer with a leakage inductance of 1 mH and a resistance of 1.1 Ω . Moreover, an additional 2.5 mH (0.94 Ω) inductor and 0.5 Ω resistor are added in line with Unit 1 to generate the mismatch ΔR and ΔX in the feeder impedances (see Fig. 5.18).

Two load operating points are considered to validate the proposed controller. At the high load point P_{load} is chosen as 1170 W and Q_{load} as 1330 var which results in a PF of 0.66. At the low load point Q_{load} is stepped down to 890 var while P_{load} is stepped down only by 32 W to 1136 W (PF=0.79) to emphasize the change in P/Q ratio. Moreover, the power factor is deliberately chosen to be low at both operating points to validate the proposed controller in the lower power factor region where sensitivity S_v is higher as discussed in Section 5.3.2.

5.6.2 Experimental Results

Experiments were performed to evaluate the effectiveness of the proposed controller. The results for a conventional controller, the proposed controller, and the enhanced controller in the presence of communication failures and time delays are presented and discussed.

The real power and reactive power are measured internally in the controller platform and are output as analog signals using PWM-DACs. The scaled P and Q values are then captured by the oscilloscope and displayed. The traces are scaled and shifted down on the oscilloscope screen to emphasize the real and reactive power behavior. Therefore, the scale “VA/div” is used here only to indicate the relative change in the power flow and the mismatch in the power sharing. The exact values of P and Q, that are calculated internally in the microcontroller, are collected through the serial-to-Ethernet module and

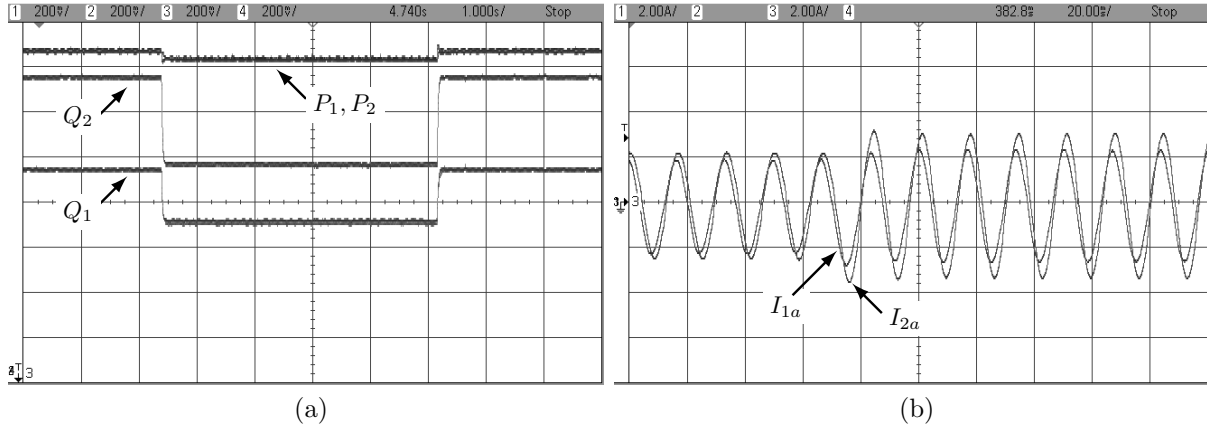


Figure 5.19: Power and current sharing under conventional droop control. (a) Real and reactive power from each inverter for step changes in the load. P_1, P_2 start at 584 W and drop to 568 W; Q_1 starts at 498 var and drops to 298 var; Q_2 starts at 825 var and drops to 522 var. (Vert: 150 VA/div; Horiz: 1 s/div) (b) Phase-a currents from each inverter for two different load operating points. (Vert: 2 A/div; Horiz: 20 ms/div)

stated in the description of the experiments and the captions of the corresponding figures.

Performance of the Conventional Controller

In Fig. 5.19a the real and reactive powers from each inverter operating under a conventional droop control scheme are shown. While the droop mechanism ensures that the real power is shared evenly between the inverters, the different output impedances of the units result in reactive power being shared unevenly. At the higher reactive load the sharing accuracy errors are $Q_{er-1} = -25\%$ and $Q_{er-2} = 25\%$.

The currents are shown in Fig. 5.19b and clearly demonstrate the mismatch between the inverters. Each current is measured at the transformer secondary and therefore does not include the portion of the associated reactive power absorbed by the transformer, which is approximately 200 var.

Performance of the Proposed Controller

When the proposed controller is enabled the virtual impedances for the two inverters are adjusted so that they share Q_{load} evenly as shown in Fig. 5.20a. The system behaviour when there is a step change in the load power is shown in Fig. 5.20b, demonstrating that the controller is effective at different load operating points. Immediately after the step there is a slight reactive power mismatch while the virtual impedances are adapted to the new operating point.

The currents before and after the enhanced control loop is enabled are shown in Fig. 5.21a and Fig. 5.21b, respectively, and show accurate steady-state sharing after the controller is enabled.

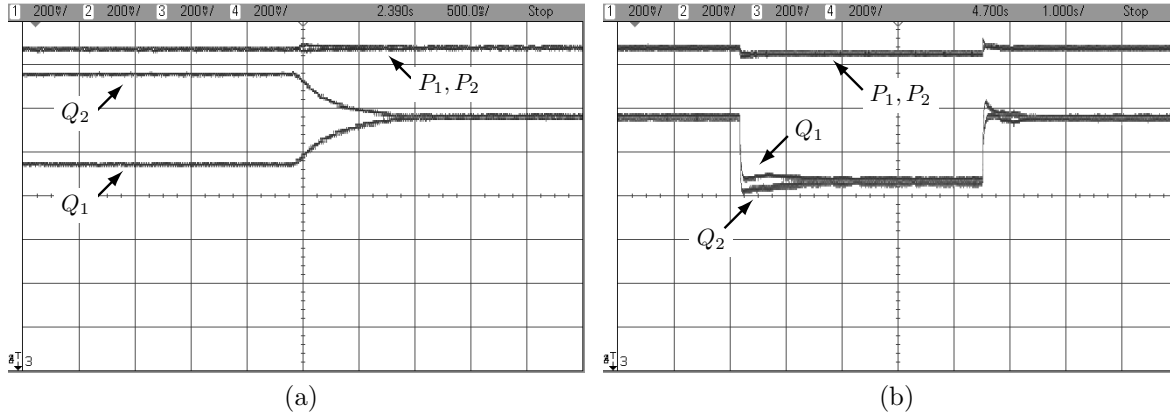


Figure 5.20: Real and reactive power sharing. (Vert: 150 VA/div) (a) As the proposed control loop is enabled. P_1, P_2 are each 584 W. Q_1 and Q_2 are initially 498 var and 825 var, respectively, and each converge to 665 var when the controller is enabled. (b) A step change in the load operating point with the controller enabled. The steady-state reactive power for each inverter steps from 665 var to 445 var and back.

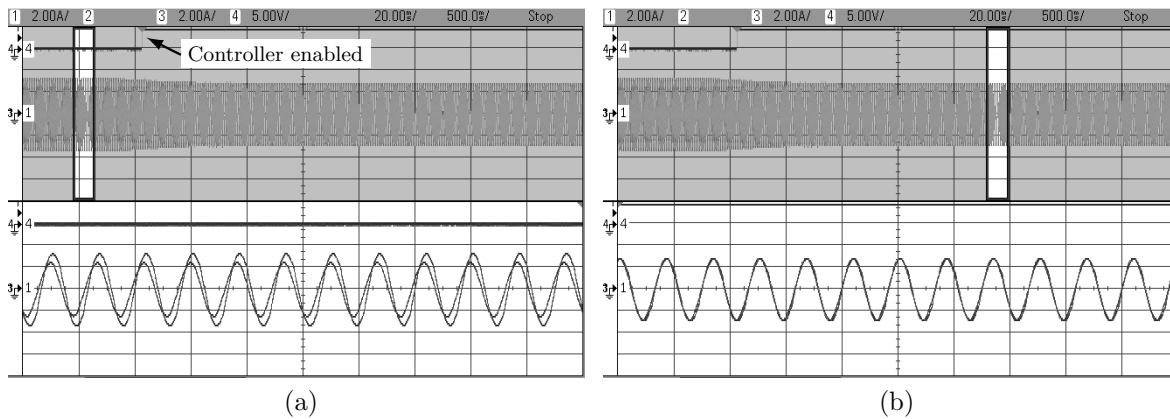


Figure 5.21: Improvement in current sharing accuracy (phase a). (a) Conventional controller (before enabling the proposed controller). (b) Proposed controller enabled. (Vert: 2 A/div; Horiz : upper 500 ms/div, lower 20 ms/div)

Performance during a Communication Failure

Fig. 5.22 shows the reactive power from each inverter along with an active-high signal that indicates whether the enhanced controller is enabled. To create a realistic failure scenario the Ethernet cable is unplugged from one of the DG units. The virtual impedance has adapted for the higher level of reactive power prior to the communication failure. When the Ethernet cable is unplugged the receive block detects the timeout and disables the control loop as shown in Fig. 5.7, thus holding \tilde{K}_v at its last tuned value. When the reactive load drops this results in some mismatch between the shared Q due to the inactive enhanced control loop. The sharing accuracy errors are $Q_{er-1} = 4.0\%$ and $Q_{er-2} = -4.0\%$. When Q increases back to its original level the reactive power is again

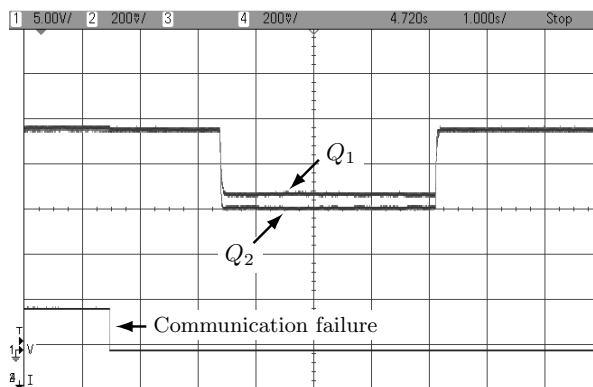


Figure 5.22: Performance of the tuned controller in response to a load change after a communication failure. The lower trace shows the controller enable signal. Q_1, Q_2 are even at 665 var each and continue at this level after communication is lost. When the reactive load is changed Q_1 drops to 439 var and Q_2 drops to 405 var. (Vert: 150 var/div; Horiz: 1 s/div)

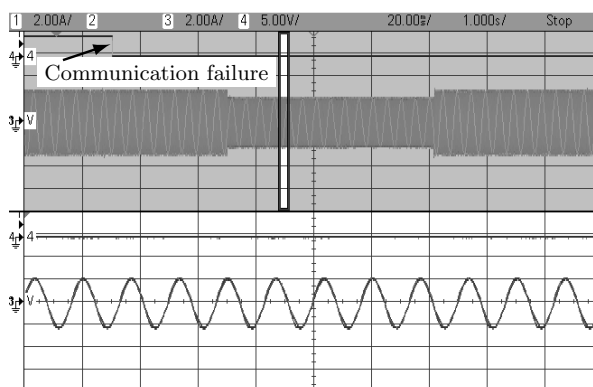


Figure 5.23: Phase-a current sharing during a communication failure with a change in reactive power load. (Vert: 2 A/div; Horiz : upper 1 s/div, lower 20 ms/div)

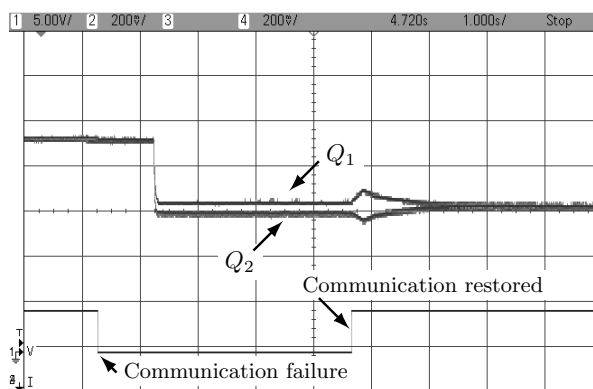


Figure 5.24: Reactive power from each inverter when communication is lost and restored (upper traces). The lower trace shows the controller enable signal. (Vert: 150 var/div; Horiz: 1 s/div)

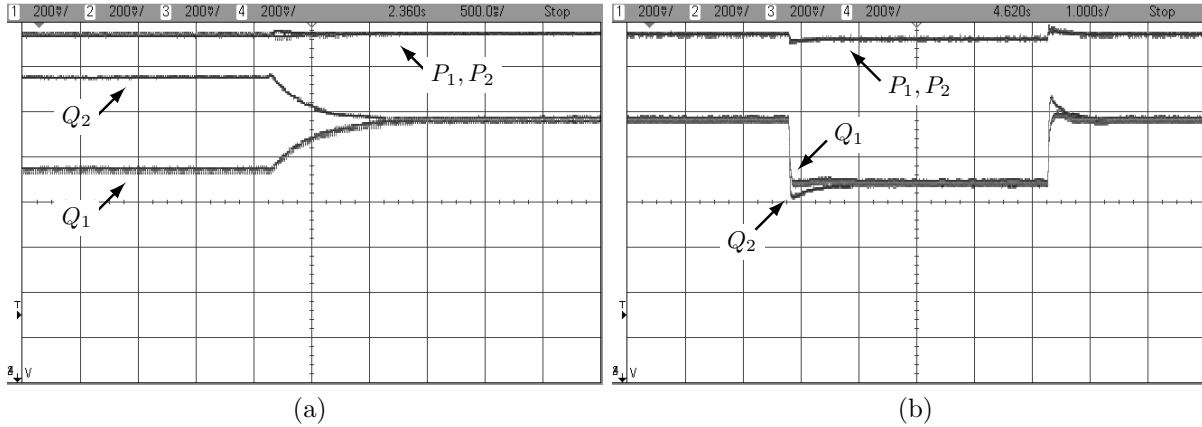


Figure 5.25: Real and reactive power sharing with a time delay mismatch in the communication channels. (a) As the proposed control loop is enabled. (Vert: 150 var/div; Horiz: 500 ms/div) (b) A step change in the load with the controller enabled. (Vert: 150 var/div; Horiz: 1 s/div)

shared accurately. Fig. 5.23 shows the phase-a current sharing during a communication failure with a change in reactive power load.

In Fig. 5.24 the effect of restoring communication is illustrated. When communication with the EMS is restored the enhanced controller is re-enabled and the error between the two reactive power outputs is rolled up as the virtual impedance is adapted to the lower reactive power level.

Performance in the presence of Delays in Communication

The effects of a delay of 0.1 s in the communication channel to *DG 1* and 0.05 s in the communication channel to *DG 2* are shown in Fig. 5.25a and Fig. 5.25b. As can be seen the time delay does not affect the sharing accuracy and the difference in the transient behaviour is negligible in comparison to the case shown in Fig. 5.20a.

5.7 Summery and Conclusion

A control strategy to improve reactive power sharing in an islanded microgrid has been proposed and validated in this chapter. The strategy employs communication to exchange the information needed to tune adaptive virtual impedances in order to compensate for the mismatch in feeder impedances. The control strategy does not require knowledge of the feeder impedances, and is straightforward to implement in practice. It is also insensitive to time delays in the communication channels. It has been shown that the proposed technique is tolerant of disruptions in the communication links while still outperforming the conventional droop control method. The sensitivity of the tuned controller parameters to changes in the system operating point has also been investigated. It has been shown that the system operating point is mainly determined by the power factor, and the higher the load power factor, the less sensitive the parameters are to the operating

point. The control strategy has been simulated and implemented in a 2 kVA experimental system and has been verified to be effective under operating point changes and realistic communication failures.

Enhanced Reactive Power Sharing in Droop Controlled Microgrids – Part II: Adaptive Voltage Droop

6.1 Introduction

An alternative technique is proposed in this chapter to improve reactive power sharing using adaptive voltage droop control. Instead of controlling the output voltage of the inverter directly, the voltage droop slope is tuned to compensate for the mismatch in the voltage drops across feeders by using communication links. A linearized small-signal model of the adaptive voltage droop is presented, and the strategy is validated using experimental results from a prototype microgrid.

The proposed control strategy is discussed in Section 6.2. A small-signal model of the tuning control loop is developed in Section 6.3. The experimental results are presented in Section 6.4, followed by the summery and the concluding remarks.

6.2 Proposed Control Strategy

As in Chapter 5, a two-unit droop controlled microgrid is used to introduce the proposed control strategy. A simplified diagram of the two-unit microgrid is shown in Fig. 6.1. Instead of directly modifying the output voltage reference to achieve accurate reactive power sharing [79–81], the slope of the voltage droop is tuned to compensate for the effect of the mismatch in the voltage drop across the feeders. Accordingly, the tuned voltage droop can still outperform the conventional fixed droop approach, even when the communication link is interrupted, as will be shown in Section 6.4.

Using (5.2), (5.18) can be rewritten as

$$V_o - n_1 Q_1 = V_{pcc} + \overline{\Delta V}_1 + \delta V_1 \quad (6.1)$$

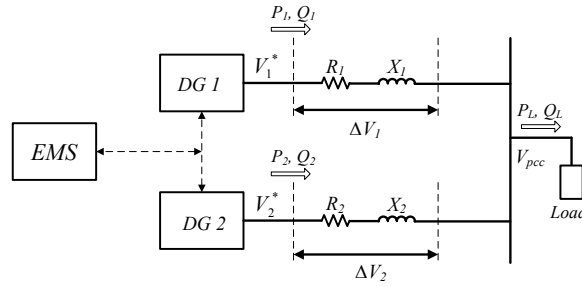


Figure 6.1: Simplified model of the microgrid with two inverters.

The voltage droop coefficient n_1 can be modified by utilizing an adaptive term \tilde{n}_1 as in

$$V_o - (n_1 + \tilde{n}_1)Q_1 = V_{pcc} + \overline{\Delta V_1} + \delta V_1 \quad (6.2)$$

If \tilde{n}_1 can be tuned at any load condition such that

$$\tilde{n}_1 Q_1 = -\delta V_1 \quad (6.3)$$

then equation (6.2) can be reduced to

$$V_o - n_1 Q_1 = V_{pcc} + \overline{\Delta V_1} \quad (6.4)$$

Therefore, the mismatch in the voltage drop across the feeders is essentially eliminated in (6.4). The controller proposed to tune the voltage droop and achieve accurate reactive power sharing is shown in Fig. 6.2. Tuning of the voltage droop slope is facilitated by utilizing the reactive power share reference Q^* , which is made available by the EMS over a communication link. As in Chapter 5, each unit sends its measured reactive power, periodically, to the EMS which calculates the proper share for each unit based on the unit rating and the total load. Accordingly, each unit receives its share reference back from the EMS.

The reference Q^* is used to tune the droop coefficient \tilde{n} using an integral controller that is implemented locally in the DG unit, as shown in Fig. 6.2. The reference Q^* is calculated based on the total reactive power demand in the microgrid. Therefore, as discussed in Chapter 5, even when Q_1 and Q_2 change individually during the tuning process action, $Q_1 + Q_2$ remains unchanged unless the total load changes. Since communication is not used in the tuning control loop, the accuracy of the reactive power sharing is unaffected by any communication delays, which is not the case with the techniques in [72, 73, 77].

The same time-out/enable logic introduced in Chapter 5 is utilized here at the receiver end, as shown in Fig. 6.2. When a communication time-out is detected, the binary signal “*Timeout*” will disable the controller ($\Delta Q = 0$). Therefore, the integrator output (\tilde{n}) will be held at the last value until the communication link is restored. In addition, when the EMS experiences a time-out in communication with any DG unit, it will stop sending

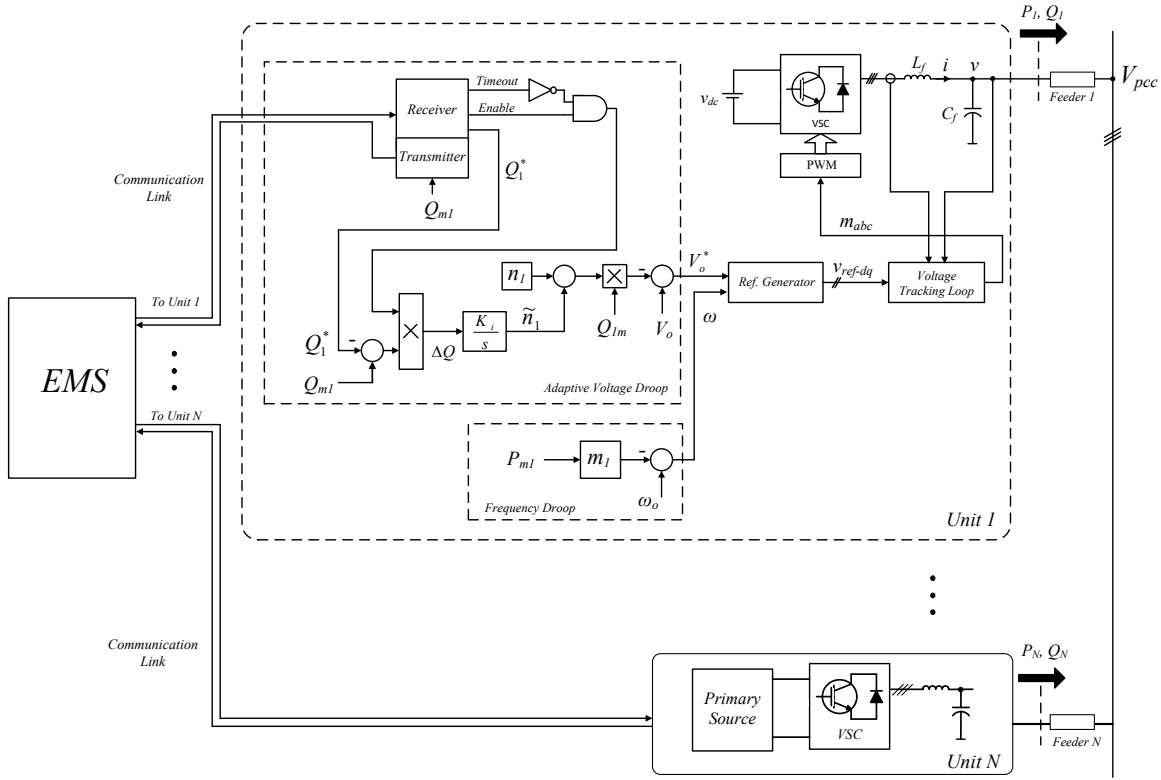


Figure 6.2: Proposed adaptive droop control for a single unit.

the references Q^* to all the units. Consequently, the tuning process will be disabled in all units, which will continue operating at the most recent droop slope.

The effect of the added adaptive droop term (\tilde{n}) will result in a negligible effect on the voltage of the microgrid bus (load voltage). This is due to the fact that under the proposed controller, the unit with a higher voltage drop across its feeder (lower reactive power) will try to reduce the voltage droop slope, and the unit with a lower voltage drop across its feeder (higher reactive power) will try to increase the voltage droop slope. Therefore, the net effect on the bus voltage will be negligible as will be shown in Section 6.4.

The integral controller gain K_i is chosen such that the controller dynamics are much slower than the reference update rate. For example, K_i is chosen as $0.00005 \text{ V}/(\text{s} \cdot \text{var}^2)$ (Table 6.1), which results in a settling time of approximately 1.45 s (see Section 6.3), in comparison to the reference update period of 0.2 s. Therefore, the time delay in the received reference will not induce any significant control action by the time the correct updated reference is received, which is within one sampling period. A time delay of longer than the update period causes the receiver to timeout until the next updated reference is received. Note that the delay in the received Q^* is composed of both the time between the instant of a reactive power load change and the subsequent sampling instant for Q^* , and any additional delays introduced by the communication channel.

Note that, as with the fixed droop slope, the integral gains are chosen to be inversely

proportional to the power ratings of each unit, $K_{i-1}Q_1 = K_{i-2}Q_2$. In this case, the controller action results in a proportional effect on the total droop slope ($n + \tilde{n}$).

When the desired slope is obtained through the control action, the system will operate as a conventional droop controller with a droop slope of $n_o = n + \tilde{n}_o$, where \tilde{n}_o is the tuned slope, until the next load change. Considering an arbitrary unit in the microgrid, from (6.3) and (5.8),

$$\tilde{n}_o Q_o \approx -\frac{\Delta X Q_o + \Delta R P_o}{V_o} \quad (6.5)$$

where Q_o and P_o are the reactive and real power at the considered operating point, respectively. Dividing both sides of (6.5) by Q_o and rearranging terms

$$\tilde{n}_o \approx -(K_x + K_r \frac{P_o}{Q_o}) \quad (6.6)$$

where $K_x = \frac{\Delta X}{V_o}$, and $K_r = \frac{\Delta R}{V_o}$. As can be concluded from (6.6), the change in \tilde{n}_o depends on the change in the ratio P_o/Q_o , as well as on ΔR as follows:

1. The smaller the ΔR , the less sensitive the tuned controller is to changes in the ratio P_o/Q_o . Accordingly, this will result in a smaller sharing error when the operating point changes during communication failures. If $\Delta R = 0$, then from (6.6), $\tilde{n}_o \approx -K_x$, which means that \tilde{n}_o is insensitive to changes in the operating point.
2. The change in \tilde{n}_o is linearly proportional to the ratio P_o/Q_o , which is uniquely related to the load power factor. Hence, the smaller the change in the power factor, the less the need for controller re-tuning, and the less the sharing error in the event of a communication interruption.

Considering the above discussion and equation (6.6), the adaptive voltage droop is more sensitive to changes in the ratio P_o/Q_o in comparison to the adaptive virtual impedances proposed in Chapter 5. In other words, using adaptive virtual impedances results in superior performance during communication failures, in comparison to the use of the adaptive voltage droop. The reason for this is explained using the following comparison:

- *Adaptive voltage droop control:* During a communication failure, the controller operates as a conventional droop controller but with the most recent tuned slope. Accordingly, any change in P_o results in changing the voltage drop mismatch across feeders (δV), as can be seen from (5.8). However, P_o has no direct effect on the control action of the voltage droop controller given by $-n_o Q$.
- *Adaptive virtual impedances:* In this case, even during communication failures, the controller directly reacts to any change in P_o . This is due to the resistive virtual impedance component, as can be observed from (5.23), (5.24), and (5.25), and summarized by

$$\delta V^* \approx -\left(\frac{\tilde{K}_{vo}Q + \tilde{K}_{vo}P}{V_o}\right) \quad (6.7)$$

6.3 Small Signal Stability Analysis

In the proposed strategy, the voltage droop coefficient is considered as the controlled variable. To gain insight into the stability of the adaptive droop control, a small-signal model is developed. The real and reactive power flows at the output of the DG unit are given as [94]

$$P = \frac{(RV^{*2} - RV^*V_{pcc} \cos \delta + XV^*V_{pcc} \sin \delta)}{R^2 + X^2} \quad (6.8)$$

$$Q = \frac{(XV^{*2} - XV^*V_{pcc} \cos \delta - RV^*V_{pcc} \sin \delta)}{R^2 + X^2} \quad (6.9)$$

where R and X are the resistive and inductive components of the feeder impedance of the unit under consideration, δ is the power angle, and V_{pcc} is the microgrid bus voltage. The integral control in Fig. 6.2, and the modified voltage droop can be written as

$$\tilde{n} = \frac{K_i}{s}(Q_m - Q^*) \quad (6.10)$$

$$V^* = V_o - (n + \tilde{n})Q_m \quad (6.11)$$

Linearizing equations (6.8),(6.9),(6.10),(6.11), along with the frequency droop equation in (5.1), around an operating point,

$$\begin{aligned} \Delta P &= \left(\frac{\partial P}{\partial V^*}\right)\Delta V^* + \left(\frac{\partial P}{\partial \delta}\right)\Delta \delta \\ &= K_{pv}\Delta V^* + K_{p\delta}\Delta \delta \end{aligned} \quad (6.12)$$

$$\begin{aligned} \Delta Q &= \left(\frac{\partial Q}{\partial V^*}\right)\Delta V^* + \left(\frac{\partial Q}{\partial \delta}\right)\Delta \delta \\ &= K_{qv}\Delta V^* + K_{q\delta}\Delta \delta \end{aligned} \quad (6.13)$$

$$\Delta \tilde{n} = \frac{K_i}{s}\Delta Q_m \quad (6.14)$$

$$\Delta V^* = -n_o\Delta Q_m - Q_o\Delta \tilde{n} \quad (6.15)$$

$$\Delta \omega = -m\Delta P_m \quad (6.16)$$

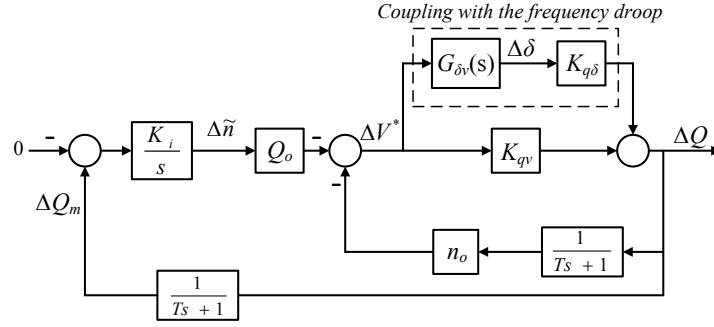


Figure 6.3: Small-signal model of the droop tuning controller.

where $n_o = n + \tilde{n}_o$. K_{pv} , $K_{p\delta}$, K_{qv} , and $K_{q\delta}$ are evaluated at the same considered operating point. Considering the first-order low-pass filter used in the measurement channel, and that $\Delta\omega = s\Delta\delta$, (6.16) can be written as

$$\Delta\delta = \frac{-m}{s(Ts + 1)}\Delta P = G_\delta(s)\Delta P \quad (6.17)$$

Substituting for ΔP from (6.17) in (6.12),

$$\Delta\delta = \frac{K_{pv}G_\delta(s)}{1 - K_{p\delta}G_\delta(s)}\Delta V^* = G_{\delta v}(s)\Delta V^* \quad (6.18)$$

Equation (6.18) represents the coupling between the reactive power controller and the real power/frequency droop control. Using (6.13), (6.14), (6.15), and (6.18), a block diagram of the system can be realized as in Fig. 6.3. Simplifying the block diagram, the system characteristic equation is given by

$$a_5s^5 + a_4s^4 + a_3s^3 + a_2s^2 + a_1s + a_0 = 0 \quad (6.19)$$

where

$$a_5 = T^3 \quad (6.20)$$

$$a_4 = n_o K_{qv} T^2 + 3T^2 \quad (6.21)$$

$$a_3 = 2n_o K_{qv} T + 3T + K_{p\delta} m T^2 + K_i Q_o K_{qv} T^2 \quad (6.22)$$

$$a_2 = -n_o m K_{q\delta} K_{pv} T + n_o m K_{qv} K_{p\delta} T + 2m K_{p\delta} T + 2K_i Q_o T K_{qv} + n_o K_{qv} + 1 \quad (6.23)$$

$$a_1 = -m K_i Q_o K_{q\delta} K_{pv} T + m K_i Q_o K_{qv} K_{p\delta} T + K_i Q_o K_{qv} - n_o m K_{q\delta} K_{pv} + n_o m K_{qv} K_{p\delta} + K_{p\delta} m \quad (6.24)$$

$$a_0 = -m K_i Q_o K_{q\delta} K_{pv} + m K_i Q_o K_{qv} K_{p\delta} \quad (6.25)$$

Considering the system parameters in Table 6.1, based on (6.19), the pole trajectories when the integral controller gain is changed from 0.00001 to 0.00025 with a step of 0.00001, are shown in Fig. 6.4. Note that four poles are affected by the change in K_i , whereas the pole at $\sigma = -31.25 \text{ s}^{-1}$ is insensitive to K_i .

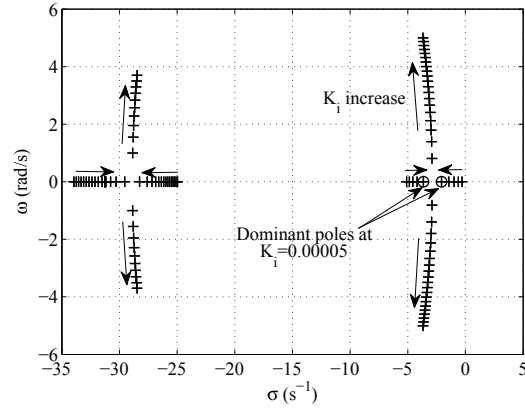
Figure 6.4: Root trajectories when K_i is varied from 0.00001 to 0.00025.

Table 6.1: System Parameters

Description	Parameter	Value
Nominal Voltage (line-line)	V_o	208 V _{l-l}
Nominal Frequency	ω_o	377 rad/s
Unit 1:		
Feeder 1 Impedance	$R_1 + jX_1$	1.6 + j2.450 Ω
Frequency Droop	m_1	0.00105 rad/(s · W)
Voltage Droop	n_1	0.005 V/var
Integral Gain	K_{i-1}	0.00005 V/(s · var ²)
Unit 2:		
Feeder 2 Impedance	$R_2 + jX_2$	1.1 + j1.508 Ω
Frequency Droop - Case 1	m_2	0.00105 rad/(s · W)
Frequency Droop - Case 2	m_2	0.00210 rad/(s · W)
Voltage Droop - Case 1	n_2	0.005 V/var
Voltage Droop - Case 2	n_2	0.010 V/var
Integral Gain - Case 1	K_{i-2}	0.00005 V/(s · var ²)
Integral Gain - Case 2	K_{i-2}	0.00010 V/(s · var ²)
Total Test Load	P_L, Q_L	800 W, 900 var
Q^* Setpoint Update Rate	f_c	5 Hz
LPF Time Constant	T	0.032 s

6.4 Experimental Evaluation

The performance of the proposed control strategy is examined on the same two-unit experimental microgrid presented in Chapter 5. The parameters of the system are included in Table 6.1. Two cases are considered to validate the performance of the proposed strategy. In *Case 1*, the strategy is first validated for units with the same power rating as in [66, 70, 71, 74, 78], to provide an intuitive visual measure of the sharing accuracy, since the units are expected to share both the real and the reactive power equally in this case.

In *Case 2*, a mismatch in both the power ratings and the feeder impedances is considered. As shown in Table 6.1, the droop coefficients of Unit 2 are set such that it appears to have half the rating of Unit 1, i.e., $m_2 = 2m_1$ and $n_2 = 2n_1$. As in Chapter 5, to evaluate the performance of the proposed controller, the reactive sharing error Q_{err-i} given by (5.50) is used [78].

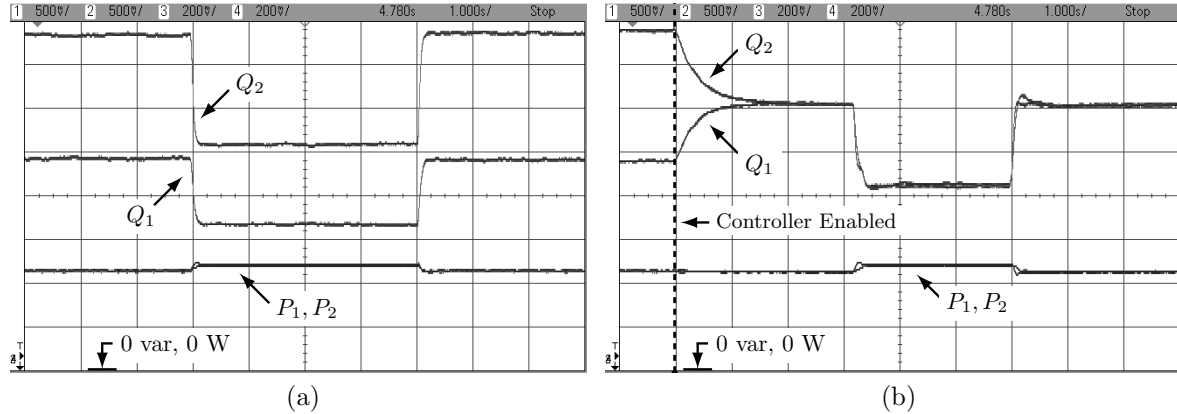


Figure 6.5: Performance of the proposed controller vs. the conventional voltage droop control - *Case 1* (Q : 72.4 var/div, P : 181 W/div, Time: 1 s/div). (a) The conventional control. (b) The proposed control strategy.

6.4.1 Case 1: Units with the Same Power Rating and Different Feeder Impedances

The performance of the proposed controller is validated in the following experimental scenarios.

Conventional vs. Adaptive Droop

The performance of the conventional voltage droop is shown in Fig. 6.5a. The load is changed between 900 var and 809 W, and 609 var and 878 W. This represents a change of 291 var in the reactive power vs. -69 W in the real power, which is selected to examine the tuning control performance under a considerable change in the ratio P/Q . From Fig. 6.5a, the sharing errors are -26.7% and 26.7% for Units 1 and 2, respectively, at the higher reactive load.

The performance of the system when the proposed controller is enabled and during a load change is shown in Fig. 6.5b. As can be seen, the tuning process takes about 1.5 s, and results in accurate power sharing with tolerable transients.

Performance during a Communication Interruption

The performance of the system during a communication interruption is shown in Fig. 6.6. In this experiment, the Ethernet cable connected to Unit 2 is physically unplugged to break the communication channel. In Fig. 6.6a, the voltage droop slope has been tuned for the load conditions when the communication is lost as marked by the controller *Timeout* signal. The units share the reactive power accurately until the reactive power is stepped up by 291 var, whereas the real power is decreased by 69 W. In this case, the sharing error increases to 1.47% which is still lower than the error in the conventional droop case (26.6%).

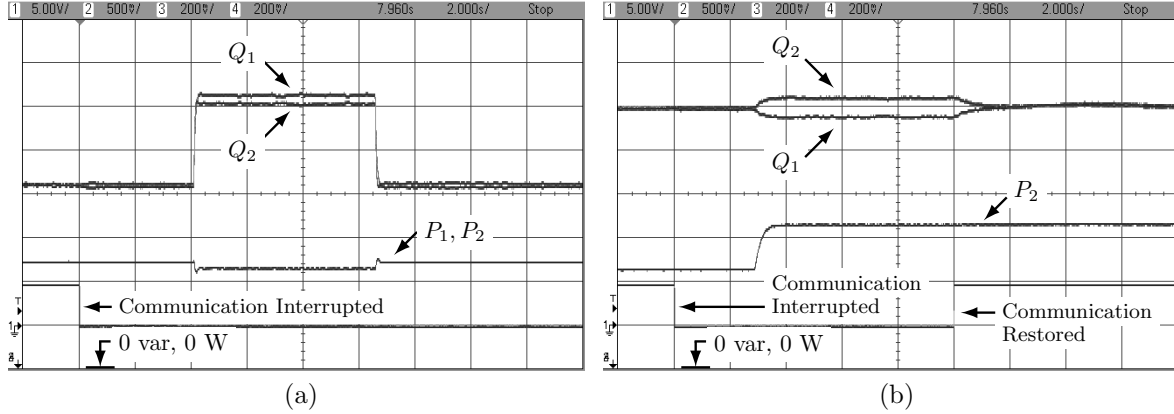


Figure 6.6: Performance of the proposed controller during a communication interruption - *Case 1* (Q : 72.4 var/div, P : 181 W/div, Time: 2 s/div). (a) During a reactive power change. (b) During a real power change.

On the other hand, the system has been tuned for the higher reactive load in Fig. 6.6b, and then the real power load is stepped up by 385 W to show the performance of the system under a considerable change in the ratio P/Q , and also in the real power. The sharing error in this case is 3.8%. Communication restoration is also shown in Fig. 6.6b, when the Ethernet cable is plugged back in.

Effect of Communication Time Delay

The effect of time delays in communication is investigated by introducing a delay in the signal sent to Unit 1. In this case, the Unit 2 controller receives the reactive power reference (Q^*) and starts acting before Unit 1 does, which has more effect on the transients in comparison to the case when the delays are identical. The introduced time delay is chosen as 0.1 s, which is significant given that the reference update period is 0.2 s (see Table 6.1). The system performance when the controller is enabled, and during a load change, is shown in Fig. 6.7. As shown, the time delay has little effect on the system transients. Most importantly, the time delay does not affect the sharing accuracy, unlike the method in [77], or in the techniques that require the availability of instantaneous control interconnections [72, 73]. It is worth mentioning that if the delay increases beyond the reference update period (0.2 s in this case), the controller will time out until the next reference is received, similar to the time out and restoration shown in Fig. 6.6b. The time delay of 0.1 s will still be used for the rest of the experiments.

Proposed Controller Effect on the Voltage of the Microgrid Bus

To show the effect of the added adaptive droop term on the voltage of the microgrid bus (load voltage), the upper peaks of the phase-a bus voltage, zoomed to 5 V/div, are shown in Fig. 6.8 to indicate the voltage amplitude when the controller is enabled. As explained in Section 6.2, the controller has a negligible effect on the bus voltage.

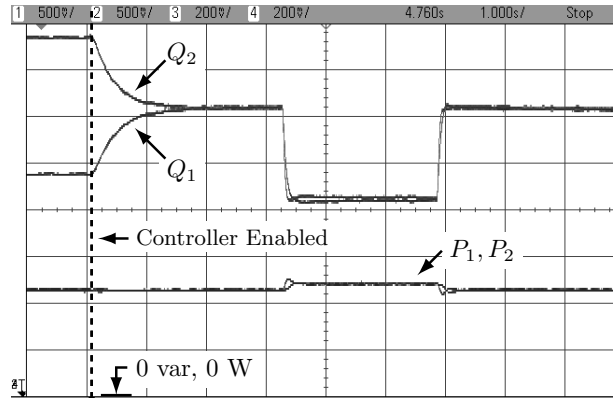


Figure 6.7: Performance of the proposed controller with a communication delay - *Case 1* (Q : 72.4 var/div, P : 181 W/div).

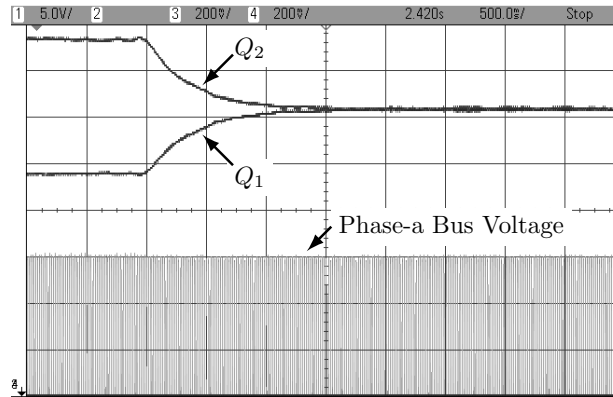


Figure 6.8: The effect of the proposed controller on the voltage of the microgrid bus (load voltage) (Q : 72.4 var/div, V_{pcc} : 5 V/div, Time: 0.5 s/div).

6.4.2 Case 2: Units with Different Power Ratings and Different Feeder Impedances

The performance of the conventional voltage droop in this case is shown in Fig. 6.9. The load is changed between 736 var and 757 W, and 572 var and 830 W. Conventional droop results in maximum sharing errors of $Q_{err-2} = 70.3\%$ at the low reactive power load, and $Q_{err-2} = 63.0\%$ at the high reactive power load. Under the low reactive power load condition, Unit 2 is supplying 324 var, while Unit 1 is supplying 248 var. Ideally, Unit 2 should supply half the reactive power share of Unit 1.

The performance of the proposed controller is shown in Fig. 6.10. It shown that after activating the controller, Unit 2 supplies half the reactive power share of Unit 1, 190 var vs. 380 var, respectively. Also, the performance of the controller after a communication disruption and a load change is shown in Fig. 6.10. The sharing errors under this condition are calculated as -2.7% and 5.4%, in comparison to 63.0% and 70.3% when using conventional droop control. The performance of the proposed control strategy, measured in terms of the sharing error Q_{err} , is summarized in Table 6.2 for selected operating points.

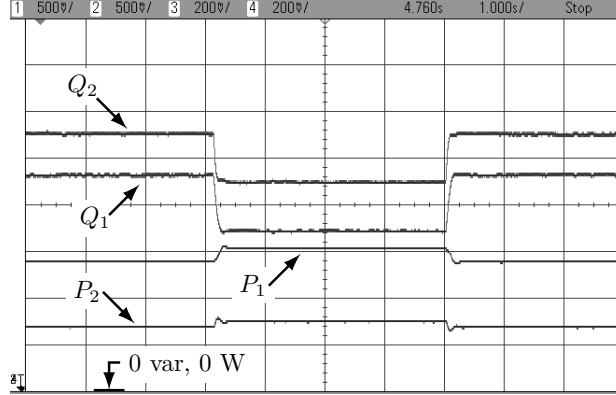


Figure 6.9: Performance of the conventional voltage droop control - *Case 2* (Q : 72.4 var/div, P : 181 W/div, Time: 1 s/div).

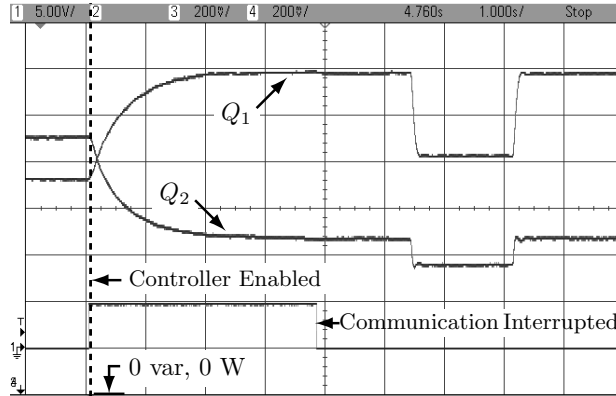


Figure 6.10: Performance of the proposed controller before and after losing communications - *Case 2* (Q : 72.4 var/div, P : 181 W/div, Time: 1 s/div).

Table 6.2: Reactive Power Sharing Error for Selected Operating Points

Case	Conventional $Q_{err-1,2}$	Proposed	
		Comm. available $Q_{err-1,2}$	Comm. Interrupted $Q_{err-1,2}$
<i>Case 1</i>	-26.0%, 26.0%	0.0, 0.0%	1.47%, -1.47%
<i>Case 2</i>	-34.8%, 70.3%	0.0, 0.0%	-2.7%, 5.4%

6.5 Summery and Conclusion

In this chapter, an alternative control strategy to improve reactive power sharing in an islanded microgrid is developed and validated experimentally. It is shown that communications can facilitate tuning the voltage droop coefficient to compensate for the effect of the mismatch in the feeder voltage drops on the reactive power sharing. A small-signal model has been developed and the stability of the proposed control loop has been analyzed. Experimental results show that the reactive power sharing using the proposed strategy is unaffected by time delays in the communication channels. Even when the communication is interrupted, the proposed control strategy can still outperform the

conventional droop control. Finally, it is shown that the added voltage droop adaptive term has negligible effect on the microgrid bus voltage.

Summary, Contributions, and Future Work

7.1 Summary and Contribution

The focus of this thesis is on developing power management strategies for islanded microgrids. The control strategies developed in this thesis can be summarized based on the hierarchal control structure, as follows:

PRIMARY CONTROL LAYER: The main objective of the strategies developed at this layer is to achieve decentralized power management of renewable energy sources and battery storage in droop controlled microgrids. More specifically, the strategies are developed for Photovoltaic (PV) as an example of one of the common renewable energy sources. The control problem of PV and battery storage in islanded microgrids, along with the literature review, are introduced in Chapter 1. Two structural configurations of the PV and the battery storage are considered. In the first configuration, the PV and the battery storage are deployed as a single PV/battery hybrid unit in the droop controlled microgrid. Two decentralized power management strategies are proposed for this configuration in Chapter 2 and Chapter 3. In the second configuration, the PV and the battery storage are deployed as separate units. The decentralized power management strategies for the PV unit and the battery storage unit, in a droop controlled microgrid, are proposed in Chapter 4.

SECONDARY CONTROL LAYER: At this layer, strategies are developed in this thesis to improve the accuracy of reactive power sharing in islanded microgrids. The problem of reactive power sharing in islanded microgrids is introduced in Chapter 1, along with the literature review. Two control strategies are proposed Chapter 5 and Chapter 6. The considered system structure, and the mathematical analysis of the problem are presented in detail in Chapter 5. In this chapter, a secondary control strategy that employs adaptive virtual impedances has been proposed to enhance the accuracy of the reactive power sharing. An alternative strategy that employs adaptive voltage droop control to improve reactive power sharing is introduced in Chapter 6. Both of the strategies developed in Chapter 5 and 6 can be implemented

in real-world microgrid systems regardless of the X/R ratio of the distribution feeders. However, the virtual impedance based strategy is expected to achieve more accurate sharing during communication failures, as discussed in Chapter 6 (Section 6.2).

The summary and the contributions of the control strategies proposed in each chapter are presented in the following:

CHAPTER 1: In this chapter, the control problem of islanded microgrids is presented. Control strategies of islanded microgrid are classified hierarchically into primary and secondary control layers, and accordingly the scope of the thesis is defined. Literature reviews of the considered control problems have been presented in this chapter.

CHAPTER 2: In this chapter, a power management strategy for PV/battery hybrid units in an islanded microgrid has been proposed. The PV/battery unit is controlled to operate as a voltage source that employs an adaptive droop control strategy, in contrast to the PV control strategies in the literature where the PV units are controlled to operate as current controlled sources (the PQ control). It has been shown that controlling the PV/battery unit as a voltage source with the proposed adaptive droop provides the PV/battery hybrid unit with several unique features. First, the hybrid unit has the ability to share the load power with other sources while storing any excess energy in the battery. Second, it can track and supply the maximum PV power to the microgrid provided that there is sufficient load demand in the microgrid. Otherwise, the hybrid unit will autonomously match the available load while charging the battery with the excess energy as in standalone strategies. Third, the control strategy modifies the PV operating point to follow the load when the total microgrid load is less than the available PV power and the battery is fully charged. Moreover, the battery may also provide the operational functions that a separate storage unit may provide in an islanded microgrid, such as regulating voltage and frequency, and supplying the deficit power in the microgrid.

CHAPTER 3: An alternative power management strategy that enables controlling a PV/battery unit as a voltage source in an islanded microgrid is proposed in this chapter. In contrast to the common way of controlling the PV unit as a current source in the literature, it is shown that controlling the hybrid unit as a voltage source that follows the proposed adaptive power/frequency characteristics, can achieve decentralized control of the hybrid unit in the islanded microgrid without relying on a central EMS and communications. This strategy eliminates the operational limitations of former technique that presented in Chapter 2. It is demonstrated experimentally that the proposed power/frequency characteristics can adapt autonomously to the microgrid operating conditions so that the hybrid unit may supply the maximum PV power, match the load, and/or charge the battery, while maintaining the power balance in the microgrid and respecting the battery SOC limits. Also, small-signal stability of the proposed control loops is investigated to gain insight into the dynamics of these loops.

CHAPTER 4: It is shown in this chapter that decentralized power management of PV and battery units can be achieved in a droop controlled microgrid, by employing the proposed multi-segment adaptive P/f characteristic curves at each of these units, without relying on a central management algorithm and communications. It has been demonstrated that the P/f characteristic can be shaped and adjusted locally in real time so that it either supplies the available PV power to the microgrid, or autonomously matches the varying load, and the battery charging power. On the other hand, the P/f characteristic curve at the battery unit is shaped and adjusted locally in real time, so that battery supplies power to the microgrid only when the load demand exceeds the total generation in the microgrid. Otherwise, the battery unit either stays floating, or charges the battery at a certain rate that is determined locally based on the battery SOC and the load/generation conditions. The decentralized power management has been demonstrated using simulation and, also, with experimental results from a prototype microgrid.

CHAPTER 5: A control strategy to improve reactive power sharing in an islanded microgrid has been proposed and validated in this chapter. The strategy employs communication to exchange the information needed to tune adaptive virtual impedances in order to compensate for the mismatch in feeder impedances. The control strategy does not require knowledge of the feeder impedances, and is straightforward to implement in practice. It is also insensitive to time delays in the communication channels. It has been shown that the proposed technique is tolerant of disruptions in the communication links while still outperforming the conventional droop control method. The sensitivity of the tuned controller parameters to changes in the system operating point has also been investigated. It has been shown that the system operating point is mainly determined by the power factor, and the higher the load power factor, the less sensitive the parameters are to the operating point. The control strategy has been simulated and implemented in an experimental system and has been verified to be effective under operating point changes and realistic communication failures.

CHAPTER 6: In this chapter, an alternative control strategy to improve reactive power sharing in an islanded microgrid is developed and validated experimentally. It is shown that communications can facilitate tuning the voltage droop coefficient to compensate for the effect of the mismatch in the feeder voltage drops on the reactive power sharing. A small-signal model has been developed and the stability of the additional control loop has been analyzed. Experimental results show that the reactive power sharing using the proposed strategy is unaffected by time delays in the communication channels. Even when the communication is interrupted, the proposed control strategy can still outperform the conventional droop control. Finally, it is shown that the added voltage droop adaptive term has negligible effect on the microgrid bus voltage.

7.2 Future Work

Potential future work is suggested in the following:

- Only a single PV, battery, or hybrid PV/battery unit is considered in the thesis to introduce the concept of the multi-segment adaptive P/f characteristics. The next step is to modify the presented P/f characteristic curves to include multiple PV, battery, or hybrid units.
- Applying the concept of the proposed multi-segment adaptive P/f characteristics to develop power management strategies for wind based DG units in islanded microgrids. Wind power has intermittent characteristics similar to that of the PV power, and therefore can be considered as a potential application for the proposed multi-segment adaptive P/f based strategy. However, wind turbines, by their nature, have more dynamics, in comparison to the static nature of the PV array where the dynamics are mainly introduced by the power electronic converters.
- Modifying the proposed decentralized control strategies to be applicable to hybrid DG units that include controllable resources, such as fuel cells or microturbines, in addition to the PV and the battery storage. The modified control strategies must consider the slow dynamics of these resources, and coordinate the power flow within the hybrid unit, and with the other DG units in the microgrid, to maintain the power balance in the islanded microgrid.
- Investigating the possibility of utilizing the proposed reactive power sharing strategy to improve harmonic power sharing in an islanded microgrid.
- Employing the concept of the developed strategies in DC islanded microgrids, in order to achieve accurate real power sharing and decentralized power management of PV and battery storage.

Bibliography

- [1] M. Montoya, R. Sherick, P. Haralson, R. Neal, and R. Yinger, “Islands in the storm: Integrating microgrids into the larger grid,” *IEEE Power and Energy Magazine*, vol. 11, no. 4, pp. 33–39, Jul. 2013.
- [2] A. Vaccaro, M. Popov, D. Villacci, and V. Terzija, “An integrated framework for smart microgrids modeling, monitoring, control, communication, and verification,” *Proceedings of the IEEE*, vol. 99, no. 1, pp. 119–132, Jan. 2011.
- [3] F. Katiraei, R. Iravani, and P. Lehn, “Micro-grid autonomous operation during and subsequent to islanding process,” *IEEE Trans. Power Del.*, vol. 20, no. 1, pp. 248–257, Jan. 2005.
- [4] B. Kroposki, R. Lasseter, T. Ise, S. Morozumi, S. Papatlianassiou, and N. Hatziargyriou, “Making microgrids work,” *IEEE Power and Energy Magazine*, vol. 6, no. 6, pp. 40–53, May 2008.
- [5] F. Blaabjerg, Z. Chen, and S. B. Kajaer, “Power electronics as efficient interface in dispersed power generation systems,” *IEEE Trans. Power Electron.*, vol. 19, no. 5, pp. 1184–1194, Dec. 2004.
- [6] J. Rocabert, A. Luna, F. Blaabjerg, and P. Rodríguez, “Control of power converters in AC microgrids,” *IEEE Trans. Power Electron.*, vol. 27, no. 11, pp. 4734–4749, Nov. 2012.
- [7] F. Katiraei, R. Iravani, N. Hatziargyriou, and A. Dimeas, “Microgrids management, control and operation aspects of microgrids,” *IEEE Power Energy Mag.*, vol. 6, no. 3, pp. 54–65, 2008.
- [8] J. A. P. Lopes, C. L. Moreira, and A. G. Madureira, “Defining control strategies for microgrids islanded operation,” *IEEE Trans. Power Syst.*, vol. 21, no. 2, pp. 439–449, May 2006.
- [9] D. Olivares, A. Mehrizi-Sani, A. H. Etemadi, C. A. Cañizares, R. Iravani, M. Kazerani, A. H. Hajimiragha, O. Gomis-Bellmunt, M. Saeedifard, R. Palma-Behnke, G. A. Jiménez-Estévez, and N. D. Hatziargyriou, “Trends in microgrid control,” *IEEE Trans. Smart Grid*, vol. 5, no. 4, pp. 1905–1919, Jul. 2014.

- [10] F. A. Inthamoussou, J. Pegueroles-Queralt, and F. D. Bianchi, "Control of a super-capacitor energy storage system for microgrid applications," *IEEE Trans. Energy Convers.*, vol. 28, no. 3, pp. 690–697, 2013.
- [11] J. M. Guerrero, J. C. Vasquez, J. Matas, L. G. de Vicuña, and M. Castilla, "Hierarchical control of droop-controlled ac and dc microgrids—A general approach toward standardization," *IEEE Trans. Ind. Electron.*, vol. 58, no. 1, pp. 158–172, Jan. 2011.
- [12] J. M. Guerrero, M. Chandorkar, T.-L. Lee, and P. C. Loh, "Advanced control architecture for intelligent microgrids—Part I: Decentralized and hierarchical control," *IEEE Trans. Power Electron.*, vol. 60, no. 4, pp. 1254–1262, Apr. 2013.
- [13] A. Yazdani and R. Iravani, *Voltage-sourced converters in power systems*. New Jersey, NJ: John Wiley, 2010.
- [14] M. B. Delghavi and A. Yazdani, "A control strategy for islanded operation of a distributed resource (DR) unit," in *IEEE Power and Energy Society General Meeting*, 2009, pp. 1 – 8.
- [15] —, "A unified control strategy for electronically interfaced distributed energy resources," *IEEE Trans. Power Del.*, vol. 27, no. 2, pp. 803–812, Apr. 2012.
- [16] —, "Islanded-mode control of electronically coupled distributed-resource units under unbalanced and nonlinear loads," *IEEE Trans. Power Del.*, vol. 26, no. 2, pp. 661–673, Apr. 2011.
- [17] A. J. W. B. F. Wollenberg, *Power Generation, Operation and Control*. New York, NY: John Wiley, 1984.
- [18] R. H. Lasseter, J. H. Eto, B. Schenkman, J. Stevens, H. Vollkommer, D. Klapp, E. Linton, H. Hurtado, and J. Roy, "CERTS microgrid laboratory test bed," *IEEE Trans. Power Del.*, vol. 26, no. 1, pp. 325–332, Jan. 2011.
- [19] C. N. Rowe, T. J. Summers, R. E. Betz, D. J. Cornforth, and T. G. Moore, "Arc-tan power–frequency droop for improved microgrid stability," *IEEE Trans. Power Electron.*, vol. 28, no. 8, pp. 3747–3759, Aug. 2013.
- [20] K. Brabandere, B. Bolsens, J. V. Keybus, A. Woyte, J. Driesen, and R. Belmans, "A voltage and frequency droop control method for parallel inverters," *IEEE Trans. Power Electron.*, vol. 22, no. 4, pp. 1107–1115, Jul. 2007.
- [21] M. Savaghebi, A. Jalilian, J. C. Vasquez, and J. M. Guerrero, "Autonomous voltage unbalance compensation in an islanded droop-controlled microgrid," *IEEE Trans. Ind. Electron.*, vol. 60, no. 4, pp. 1390–1402, Apr. 2013.
- [22] D. De and V. Ramanarayanan, "Decentralized parallel operation of inverters sharing unbalanced and nonlinear loads," *IEEE Trans. Power Electron.*, vol. 25, no. 12, pp. 3015–3025, Dec. 2010.

- [23] M. B. Delghavi and A. Yazdani, "An adaptive feedforward compensation for stability enhancement in droop-controlled inverter based microgrids," *IEEE Trans. Power Del.*, vol. 26, no. 3, pp. 1764–1773, Jul. 2011.
- [24] A. Haddadi, A. Yazdani, and G. Joos, "A gain-scheduled decoupling control strategy for enhanced transient performance and stability of an islanded active distribution network," *IEEE Trans. Power Del.*, vol. 29, no. 2, pp. 560–569, Apr. 2014.
- [25] W. Jiang and B. Fahimi, "Active current sharing and source management in fuel cell–battery hybrid power system," *IEEE Trans. Ind. Electron.*, vol. 57, no. 2, pp. 752–761, Feb. 2010.
- [26] P. Thounthong, S. Pierfederici, J.-P. Martin, M. Hinaje, and B. Davat, "Modeling and control of fuel cell/supercapacitor hybrid source based on differential flatness control," *IEEE Trans. Veh. Technol.*, vol. 59, no. 6, pp. 2700–2710, Jul. 2010.
- [27] K. Jin, X. Ruan, M. Yang, and M. Xu, "A hybrid fuel cell power system," *IEEE Trans. Ind. Electron.*, vol. 56, no. 4, pp. 1212–1222, Apr. 2009.
- [28] P. Thounthong, S. Rael, and B. Davat, "Analysis of supercapacitor as second source based on fuel cell power generation," *IEEE Trans. Energy Convers.*, vol. 24, no. 1, pp. 247–255, Mar. 2009.
- [29] ———, "Control algorithm of fuel cell and batteries for distributed generation system," *IEEE Trans. Energy Convers.*, vol. 23, no. 1, pp. 148–155, Mar. 2008.
- [30] H. Tao, J. L. Duarte, and M. A. M. Hendrix, "Line-interactive ups using a fuel cell as the primary source," *IEEE Trans. Ind. Electron.*, vol. 55, no. 8, pp. 3012–3021, Aug. 2008.
- [31] A. Khaligh, A. M. Rahimi, Y. Lee, J. Cao, A. Emadi, S. D. Andrews, C. Robinson, and C. Finnerty, "Digital control of an isolated active hybrid fuel cell/li-ion battery power supply," *IEEE Trans. Veh. Technol.*, vol. 56, no. 6, pp. 3709–3721, Nov. 2007.
- [32] Z. Jiang, L. Gao, and R. A. Dougal, "Control algorithm of fuel cell and batteries for distributed generation system," *IEEE Trans. Energy Convers.*, vol. 22, no. 2, pp. 507–515, Jun. 2007.
- [33] Z. Jiang and R. A. Dougal, "A compact digitally controlled fuel cell/battery hybrid power source," *IEEE Trans. Ind. Electron.*, vol. 53, no. 4, pp. 1094–1104, Aug. 2006.
- [34] L. Solero, A. Lidozzi, and J. A. Pomilio, "Design of multiple-input power converter for hybrid vehicles," *IEEE Trans. Power Electron.*, vol. 20, no. 5, pp. 1007–1016, 2005.
- [35] L. Gao, Z. Jiang, and R. A. Dougal, "Evaluation of active hybrid fuel cell/battery power sources," *IEEE Trans. Aerosp. Electron. Syst.*, vol. 41, no. 1, pp. 346–355, Jan. 2005.

- [36] M. Dai, M. N. Marwali, J.-W. Jung, and A. Keyhani, "Power flow control of a single distributed generation unit," *IEEE Trans. Power Electron.*, vol. 23, no. 1, pp. 343–352, Jan. 2008.
- [37] M. N. Marwali, J.-W. Jung, and A. Keyhani, "Control of distributed generation systems—Part II: Load sharing control," *IEEE Trans. Power Electron.*, vol. 19, no. 6, pp. 1551–1561, Nov. 2004.
- [38] J. C. Vasquez, J. M. Guerrero, M. Savaghebi, J. Eloy-Garcia, and R. Teodorescu, "Modeling, analysis, and design of stationary-reference-frame droop-controlled parallel three-phase voltage source inverters," *IEEE Trans. Ind. Electron.*, vol. 60, no. 4, pp. 1271–1280, Apr. 2013.
- [39] M. Savaghebi, A. Jalilian, J. C. Vasquez, and J. M. Guerrero, "Secondary control scheme for voltage unbalanced compensation in an islanded droop-controlled microgrid," *IEEE Trans. Smart Grid*, vol. 3, no. 2, pp. 797–807, Jun. 2012.
- [40] —, "Secondary control for voltage quality enhancement in microgrids," *IEEE Trans. Smart Grid*, vol. 3, no. 4, pp. 1893–1902, Dec. 2012.
- [41] I. U. Nutkani, P. C. Loh, and F. Blaabjerg, "Droop scheme with considering of operating cost," *IEEE Trans. Power Electron.*, vol. 29, no. 3, pp. 1047–1052, Mar. 2014.
- [42] A. A. Bidram, A. Davoudi, F. L. Lewis, and J. M. Guerrero, "Distributed cooperative secondary control of microgrids using feedback linearization," *IEEE Trans. Power Syst.*, vol. 28, no. 3, pp. 3462–3470, Aug. 2013.
- [43] M. A. Abusara, J. M. Guerrero, and S. M. Sharkh, "Line interactive UPS for microgrids," *IEEE Trans. Ind. Electron.*, vol. 61, no. 3, pp. 1292–1300, Mar. 2014.
- [44] Q. Jiang, M. Xue, and G. Geng, "Energy management of microgrid in grid-connected and stand-alone modes," *IEEE Trans. Power Syst.*, vol. 28, no. 3, pp. 3380–3389, Aug. 2013.
- [45] D. Olivares, C. A. Cañizares, and M. Kazerani, "A centralized energy management system for isolated microgrids," *IEEE Trans. Smart Grid*, vol. 5, no. 4, pp. 1864–1875, Jul. 2014.
- [46] M. M. A. Abdelaziz, M. F. Shaaban, H. E. Farag, and E. F. El-Saadany, "A multi-stage centralized control scheme for islanded microgrids with PEVs," *IEEE Trans. Sustain. Energy*, vol. 5, no. 3, pp. 927–937, Jul. 2012.
- [47] S. J. Chiang, H.-J. Shieh, and M.-C. Chen, "Modeling and control of a PV charger system with SEPIC converter," *IEEE Trans. Ind. Electron.*, vol. 56, no. 11, pp. 4344–4353, Nov. 2009.

- [48] F. Locment, M. Sechilariu, and I. Houssamo, "DC load and batteries control limitations for photovoltaic systems. Experimental validation," *IEEE Trans. Power Electron.*, vol. 27, no. 9, pp. 4030–4038, Sep. 2012.
- [49] F. Ongaro, S. Saggini, and P. Mattavelli, "Li-ion battery-supercapacitor hybrid storage system for a long lifetime, photovoltaic-based wireless sensor network," *IEEE Trans. Power Electron.*, vol. 27, no. 9, pp. 3944–3952, Sep. 2012.
- [50] H. Mahmood, D. Michaelson, and J. Jiang, "Control strategy for a standalone PV/battery hybrid system," in *In Conf. Proc. IEEE Industrial Electronics Conference*, 2012, pp. 3412–3418.
- [51] C. Wang and M. H. Nehrir, "Power management of a stand-alone wind/photovoltaic/fuel cell energy system," *IEEE Trans. Energy Convers.*, vol. 23, no. 3, pp. 957–967, Sep. 2008.
- [52] B. Belvedere, M. Bianchi, A. Borghetti, C. A. Nucci, M. Paolone, and A. Peretto, "A microcontroller-based power management system for a standalone microgrids with hybrid power supply," *IEEE Trans. Sustain. Energy*, vol. 3, no. 3, pp. 422–431, Jul. 2012.
- [53] K. T. Tan, X. Y. Peng, P. L. So, Y. C. Chu, and M. Z. Q. Chen, "Centralized control for parallel operation of distributed generation inverters in microgrids," *IEEE Trans. Smart Grid*, vol. 3, no. 4, pp. 1977–1987, Dec. 2012.
- [54] B. Wang, M. Sechilariu, and F. Locment, "Intelligent DC microgrid with smart grid communications: control strategy consideration and control," *IEEE Trans. Smart Grid*, vol. 3, no. 4, pp. 2148–2156, Dec. 2012.
- [55] K. T. Tan, P. L. So, Y. C. Chu, and M. Z. Q. Chen, "Coordinated control and energy management of distributed generation inverters in microgrid," *IEEE Trans. Power Del.*, vol. 28, no. 2, pp. 704–713, Apr. 2013.
- [56] J. Kim, J. Jeon, S. Kim, C. Cho, J. Park, H. Kim, and K. Nam, "Cooperative control strategy of energy storage system and microsourses for stabilizing the microgrid during islanded operation," *IEEE Trans. Power Electron.*, vol. 25, no. 12, pp. 3037–3048, Dec. 2010.
- [57] Y.-K. Chen, Y.-C. Wu, C.-C. Song, and Y.-S. Chen, "Design and implementation of energy management system with fuzzy control for dc microgrid systems," *IEEE Trans. Power Electron.*, vol. 28, no. 4, pp. 1563–1570, Apr. 2013.
- [58] J. Han, S. K. Solanki, and J. Solanki, "Coordinated predictive control of a wind/battery microgrid system," *IEEE Journal of Emerging and Selected Topics in Power Electronics*, vol. 1, no. 4, pp. 296–305, Dec. 2013.
- [59] E. Serban and H. Serban, "A control strategy for a distributed power generation microgrid application with voltage- and current controlled source converter," *IEEE Trans. Power Electron.*, vol. 25, no. 12, pp. 2981–2992, Dec. 2010.

- [60] D. Wu, F. Tang, T. Dragicevic, J. C. Vasquez, and J. M. Guerrero, "Autonomous active power control for islanded ac microgrids with photovoltaic generation and energy storage system," *IEEE Trans. Energy Convers.*, vol. PP, no. 99, pp. 1–11, Mar. 2014.
- [61] S. Bae and A. Kwasinski, "Dynamic modeling and operation strategy for a microgrid with wind and photovoltaic resources," *IEEE Trans. Smart Grid*, vol. 3, no. 4, pp. 1867–1876, Dec. 2014.
- [62] L. Valverde, F. Rosa, and C. Bordons, "Design, planning and management of a hydrogen-based microgrid," *IEEE Trans. Ind. Informat.*, vol. 9, no. 3, pp. 1398–1404, Aug. 2013.
- [63] H. Ghoddami, M. B. Delghavi, and A. Yazdani, "An integrated wind-photovoltaic-battery system with reduced power-electronic interface and fast control for grid-tied and off-grid applications," *Renewable Energy*, vol. 45, pp. 128–137, 2012.
- [64] S. Adhikari and F. Li, "Coordinated V-f and P-Q control of solar photovoltaic generators with MPPT and battery storage in microgrids," *IEEE Trans. Smart Grid*, vol. 5, no. 3, pp. 1270–1281, May 2014.
- [65] J. Kim, J. Guerrero, P. Rodriguez, R. Teodorescu, and K. Nam, "Mode adaptive droop control with virtual output impedances for an inverter-based flexible AC microgrid," *IEEE Trans. Power Electron.*, vol. 26, no. 3, pp. 689–700, Mar. 2011.
- [66] W. Yao, M. Chen, J. Matas, J. M. Guerrero, and Z.-M. Qian, "Design and analysis of the droop control method for parallel inverters considering the impact of the complex impedance on the power sharing," *IEEE Trans. Ind. Electron.*, vol. 58, no. 2, pp. 576–588, Feb. 2011.
- [67] J. M. Guerrero, J. Matas, L. G. de Vicuña, M. Castilla, and J. Miret, "Decentralized control for parallel operation of distributed generation inverters using resistive output impedance," *IEEE Trans. Ind. Electron.*, vol. 54, no. 2, pp. 994–1004, Apr. 2007.
- [68] J. M. Guerrero, L. G. de Vicuña, J. Matas, M. Castilla, and J. Miret, "Output impedance design of parallel-connected UPS inverters with wireless load-sharing control," *IEEE Trans. Ind. Electron.*, vol. 52, no. 4, pp. 1126–1135, Aug. 2005.
- [69] A. Tuladhar, H. Jin, T. Unger, and K. Mauch, "Control of parallel inverters in distributed AC power systems with consideration of line impedance effect," *IEEE Trans. Ind. Appl.*, vol. 36, no. 1, pp. 131–138, Jan./Feb. 2000.
- [70] Y. W. Li and C.-N. Kao, "An accurate power control strategy for power-electronics-interfaced distributed generation units operating in a low-voltage multibus microgrid," *IEEE Trans. Power Electron.*, vol. 24, no. 12, pp. 2977–2988, Dec. 2009.

- [71] Q.-C. Zhong, "Robust droop controller for accurate proportional load sharing among inverters operated in parallel," *IEEE Trans. Ind. Electron.*, vol. 60, no. 4, pp. 1281–1290, Apr. 2013.
- [72] X. Yu, A. M. Khambadkone, H. Wang, and S. T. S. Terence, "Control of parallel-connected power converters for low-voltage microgrid- part i: a hybrid control architecture," *IEEE Trans. Power Electron.*, vol. 25, no. 12, pp. 2962–2970, Dec. 2010.
- [73] A. M. Roslan, K. H. Ahmed, S. J. Finney, and B. W. Williams, "Improved instantaneous average current-sharing control scheme for parallel-connected inverter considering line impedance impact in microgrid networks," *IEEE Trans. Power Electron.*, vol. 26, no. 3, pp. 702–716, Mar. 2011.
- [74] J. He and Y. W. Li, "An enhanced microgrid load demand sharing strategy," *IEEE Trans. Power Electron.*, vol. 27, no. 9, pp. 3984–3995, Sep. 2012.
- [75] J. He, Y. W. Li, J. M. Guerrero, J. C. Vasquez, and F. Blaabjerg, "An islanded microgrid reactive power sharing scheme enhanced by programmed virtual impedances," in *Proc. IEEE International Symposium on Power Electronics for Distributed Generation Systems*, 2012, pp. 229–235.
- [76] J. He, Y. W. Li, J. M. Guerrero, F. Blaabjerg, and J. C. Vasquez, "An islanding microgrid power sharing approach using enhanced virtual impedance control scheme," *IEEE Trans. Power Electron.*, vol. 28, no. 11, pp. 5272–5282, Nov. 2013.
- [77] Y. Zhang and H. Ma, "Theoretical and experimental investigation of networked control for parallel operation of inverters," *IEEE Trans. Ind. Electron.*, vol. 59, no. 4, pp. 1961–1970, Apr. 2012.
- [78] C.-T. Lee, C.-C. Chu, and P.-T. Cheng, "A new droop control method for the autonomous operation of distributed energy resources interface converters," *IEEE Trans. Power Electron.*, vol. 28, no. 4, pp. 1980–1993, Apr. 2013.
- [79] Q. Shafiee, J. M. Guerrero, and J. C. Vasquez, "Distributed secondary control for islanded microgrids—a novel approach," *IEEE Trans. Power Electron.*, vol. 29, no. 2, pp. 1018–1031, Feb. 2014.
- [80] Q. Shafiee, C. Stefanovic, T. Dragicevic, P. Popovski, J. C. Vasquez, and J. M. Guerrero, "Robust networked control scheme for distributed secondary control of islanded microgrids," *IEEE Trans. Ind. Electron.*, vol. 61, no. 10, pp. 5363–5374, Oct. 2014.
- [81] A. Micallef, M. Apap, C. Spiteri-Staines, J. M. Guerrero, and J. C. Vasquez, "Reactive power sharing and voltage harmonic distortion compensation of droop controlled single phase islanded microgrids," *IEEE Trans. Smart Grid*, vol. 5, no. 3, pp. 1149–1158, May 2014.

- [82] E. Barklund, N. Pogaku, M. Prodanović, C. Hernandez-Aramburo, and T. C. Green, “Energy management in autonomous microgrid using stability-constrained droop control of inverters,” *IEEE Trans. Power Electron.*, vol. 23, no. 5, pp. 2346–2352, Sep. 2008.
- [83] S. X. Chen, H. B. Gooi, and M. Q. Wang, “Sizing of energy storage for microgrids,” *IEEE Trans. Smart Grid*, vol. 3, no. 1, pp. 142–151, Mar. 2012.
- [84] N. Pogaku, M. Prodanović, and T. C. Green, “Modeling, analysis and testing of autonomous operation of an inverter-based microgrid,” *IEEE Trans. Power Electron.*, vol. 22, no. 2, pp. 613–625, Mar. 2007.
- [85] E. A. A. Coelho, P. C. Cortizo, and P. F. D. Garcia, “Small-signal stability for parallel-connected inverters in stand-alone AC supply systems,” *IEEE Trans. Ind. Appl.*, vol. 38, no. 2, pp. 533–542, Mar./Apr. 2002.
- [86] N. Kakimoto, H. Satoh, S. Takayama, and K. Nakamura, “Ramp-rate control of photovoltaic generator with electric double-layer capacitor,” *IEEE Trans. Energy Convers.*, vol. 24, no. 2, pp. 465–473, Jun. 2009.
- [87] E. Koutroulis and K. Kalaitzakis, “Novel battery charging regulation system for photovoltaic applications,” *IEE Proc.-Electr. Power Appl.*, vol. 151, no. 2, pp. 191–197, Mar. 2004.
- [88] Y. Cao, S. Tang, C. Li, P. Zhang, Y. Tan, Z. Zhang, and J. Li, “An optimized EV charging model considering tou price and soc curve,” *IEEE Trans. Smart Grid*, vol. 3, no. 1, pp. 388–393, Mar. 2012.
- [89] H. Fakham, D. Lu, and B. Francois, “Power control design of a battery charger in a hybrid active PV generator for load-following applications,” *IEEE Trans. Ind. Electron.*, vol. 58, no. 1, pp. 85–94, Jan. 2011.
- [90] Z. Miao, L. Xu, V. R. Disfani, and L. Fam, “An SOC-based battery management system for microgrids,” *IEEE Trans. Smart Grid*, vol. 5, no. 2, pp. 966–973, Mar. 2014.
- [91] R. F. Nelson, “Power requirements for batteries in hybrid electric vehicles,” *J. Power Sources*, vol. 91, no. 1, pp. 2–26, Aug. 2000.
- [92] Q.-C. Zhong, “Robust droop controller for accurate proportional load sharing among inverters operated in parallel,” *IEEE Trans. Ind. Electron.*, vol. 60, no. 4, pp. 1281–1290, Apr. 2013.
- [93] R. H. Lasseter and P. Piagi, “Control and design of microgrid components, Final project report,” Power System Engineering Research Center (PSERC), Madison, WI, Tech. Rep. 06-03, Jan. 2006.

- [94] E. A. A. Coelho, P. C. Cortizo, and P. F. D. Garcia, "Small signal stability for single phase inverter connected to a stiff AC system," in *IEEE 34th Industry Application Conf.*, 1999, pp. 2180 – 2187.
- [95] T. Dragičević, J. M. Guerrero, J. C. Vasquez, and D. Škrlec, "Supervisory control of an adaptive regulated DC microgrid with battery management capability," *IEEE Trans. Power Electron.*, vol. 29, no. 2, pp. 695–706, Feb. 2014.
- [96] H. Mahmood, D. Michaelson, and J. Jiang, "Accurate reactive power sharing in an islanded microgrid using adaptive virtual impedances," *IEEE Trans. Power Electron.*, vol. PP, no. 99, pp. 1–1, 2014.
- [97] T. L. Vandoorn, J. C. Vasquez, J. D. Kooning, J. M. Guerrero, and L. Vandeveld, "Microgrids: Hierarchical control and an overview of the control and reserve management strategies," *IEEE Industrial Electronics Magazine*, vol. 7, no. 4, pp. 42–55, dec 2013.
- [98] H. J. Avelar, W. A. Parreira, J. B. Vieira, L. de Freitas, and E. A. A. Coelho, "A state equation model of a single-phase grid-connected inverter using a droop control scheme with extra phase shift control action," *IEEE Trans. Ind. Electron.*, vol. 59, no. 3, pp. 1527–1537, Mar. 2012.

©2014 IEEE. Reprinted, with permission, from H. Mahmood, D. Michaelson, J. Jiang, "Accurate reactive power sharing in an islanded microgrid using adaptive virtual impedances," *IEEE Transactions on Power Electronics*, Oct. 2014.

©2014 IEEE. Reprinted, with permission, from H. Mahmood, D. Michaelson, J. Jiang, "A power management strategy for PV/battery hybrid systems in islanded microgrids," *IEEE Journal of Emerging and Selected Topics in Power Electronics*, Oct. 2014.

©2012 IEEE. Reprinted, with permission, from H. Mahmood, D. Michaelson, J. Jiang, "Control strategy for a standalone PV/battery hybrid system," in *Proc. IEEE Ind. Electron. Conf.*, Oct. 2012.

Control Structures and Parameters of the Power Electronic Converters

A.1 Internal Controllers of the DC-DC Converters

The schematic diagram of the PV and the battery DC-DC converters, as connected in the hybrid system, is shown in Fig. A.1. The key parameters of the system are presented in Table A.1. The controllers of the DC-DC converters are shown in Fig. A.2. Both voltage controllers employ an averaged current control loop to damp the LC resonance, and to provide stiff voltage regulation. LPF_i and LPF_v are first order low-pass filters used to reduce switching noise and current ripple. The controllers $\text{PI}_{\text{pv-i}}$, $\text{PI}_{\text{pv-v}}$, $\text{PI}_{\text{B-i}}$, and $\text{PI}_{\text{B-v}}$ are designed as in [50], and given by

$$G_{\text{PI-pv-i}}(s) = \frac{0.5s + 250}{s} \quad (\text{A.1})$$

$$G_{\text{PI-pv-v}}(s) = \frac{0.01s + 40}{s} \quad (\text{A.2})$$

$$G_{\text{PI-B-i}}(s) = \frac{1s + 250}{s} \quad (\text{A.3})$$

$$G_{\text{PI-B-v}}(s) = \frac{0.03s + 30}{s} \quad (\text{A.4})$$

Note that, the same controllers are used for the PV and the battery when connected separately in Chapter 4. The oscilloscope traces shown in Fig. A.3 demonstrate the performance of the converters in the hybrid configuration, during a load disturbance of approximately ± 1000 W [50]. The top trace shows the DC-link voltage, which is effectively regulated by the battery converter at 400 V. The externally triggered load change can be seen when i_L , the load current, steps up and down. The current injected into the DC-link by the PV converter is shown as $i_{\text{pv}o}$, which was 3.2 A for this experiment. The i_{LB} traces show the inductor current in the battery converter, which has an average negative value during the low-load condition, thus charging the battery, and an average positive value during the high-load condition to support the PV source.

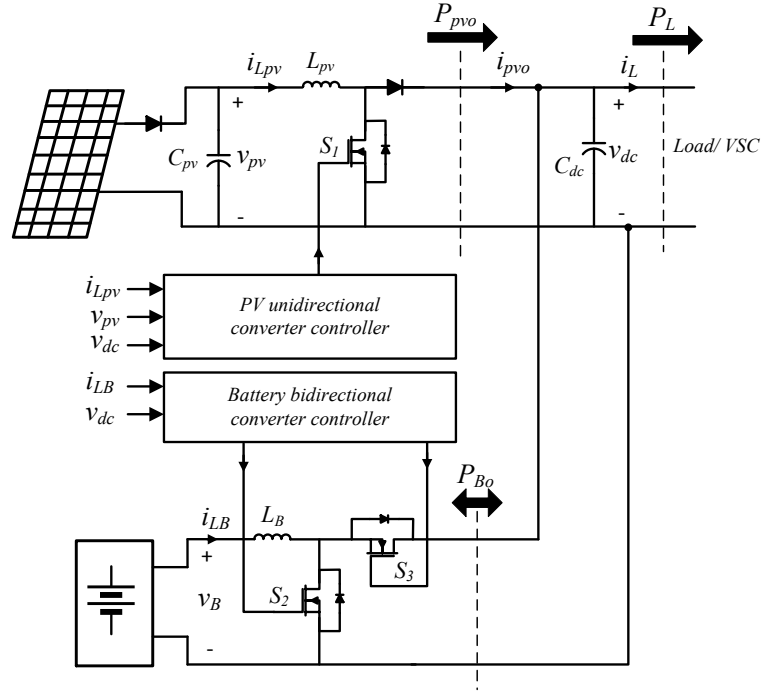


Figure A.1: Schematic diagram of the PV and the battery DC-DC converters.

Table A.1: Key Parameters of the DC-DC Converters

Description	Parameter	Value
PV Input Capacitor	C_{pv}	1500 μF
PV Converter Inductor	L_{pv}	550 μH
Output Capacitors	C_{dc}	1200 μF
Battery Converter Inductor	L_B	880 μH
Nominal DC-link Voltage	V_{dc-ref}	400 V

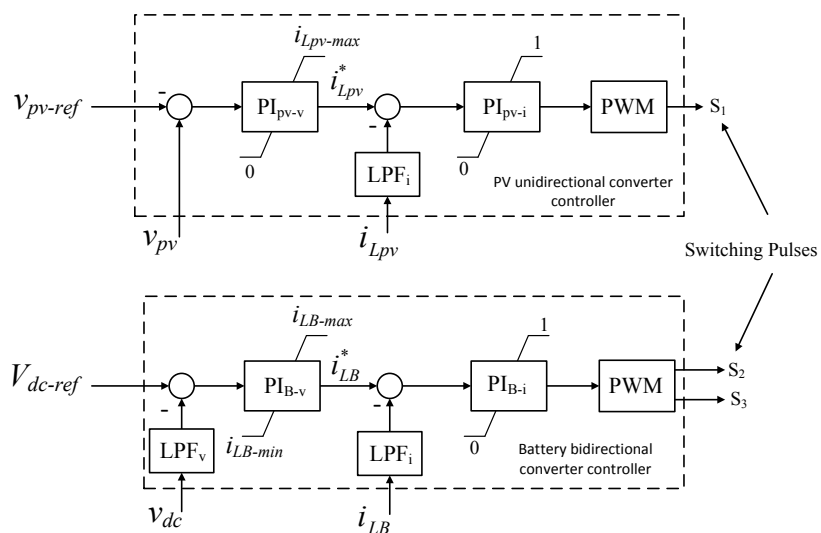


Figure A.2: Controllers of the PV and the battery DC-DC converters.

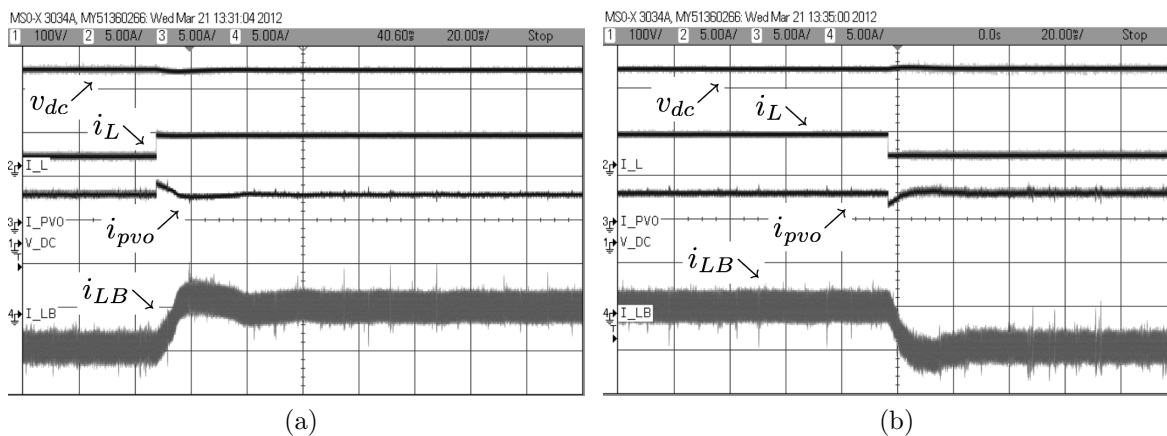


Figure A.3: Experimental performance of the DC-DC converters in response to a load disturbance. (a) Step-up load disturbance. (b) Step-down load disturbance.

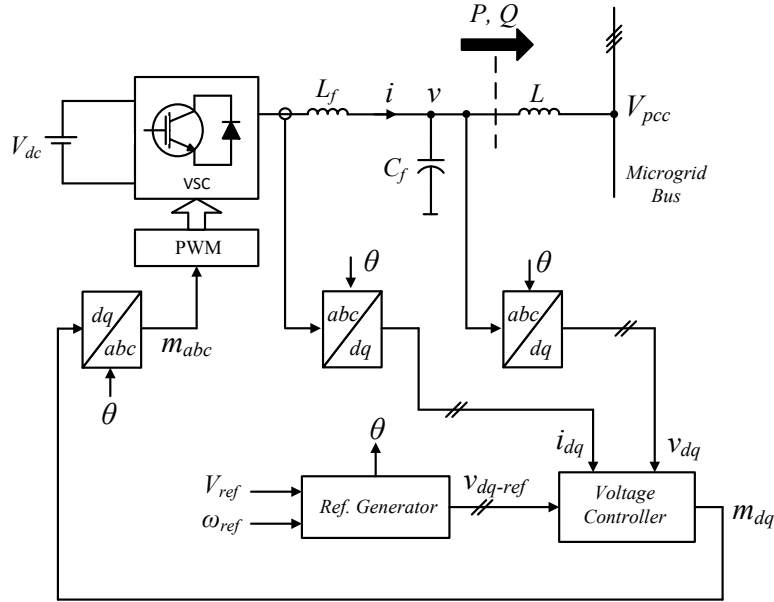


Figure A.4: Simplified diagram of a voltage regulation strategy for a 3-phase Grid-Forming DG unit (voltage controlled source).

A.2 Voltage Control System of the VSC

A simplified schematic diagram of the VSC controller is shown in Fig. A.4. The internal control loops of the voltage controller are implemented in the synchronous frame (dq-frame) as shown in Fig. A.5 [13,14], where L_f (5.1 mH) and C_f (75 μ F) are the inductance and the capacitance of the output filter. The PI controllers are designed as in [13,14], and summarized as below

$$G_{PI-i}(s) = 4800 \left(\frac{5.1 \times 10^{-3}s + 0.3}{s} \right) \quad (\text{A.5})$$

$$G_{PI-v}(s) = 0.138 \left(\frac{s + 707.3}{s} \right) \quad (\text{A.6})$$

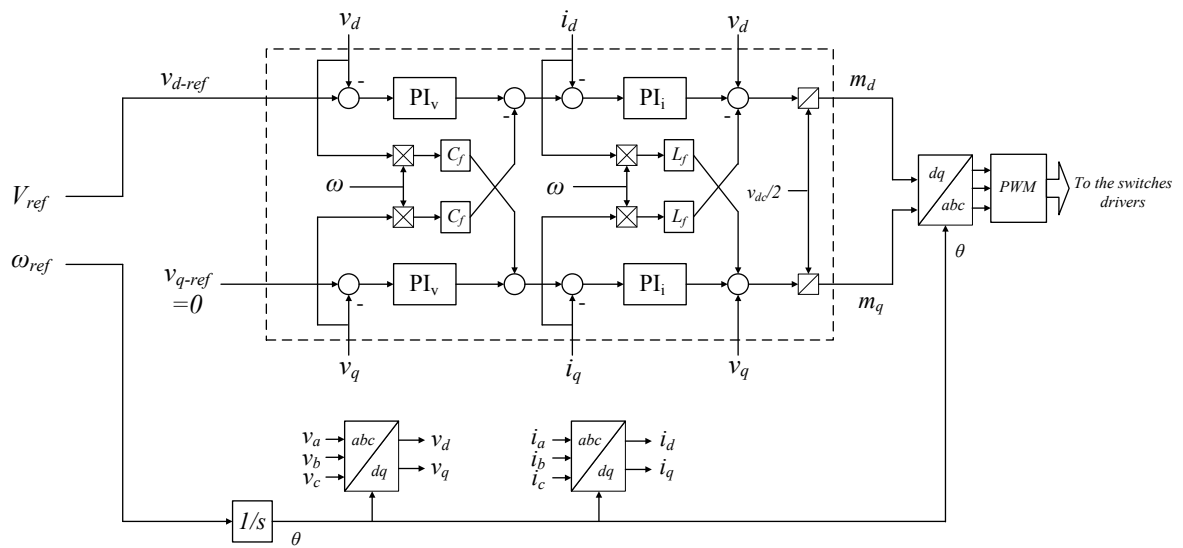


Figure A.5: Voltage tracking loops of the of the VSC.

Parameters Definitions for Chapter 4

B.1 Parameters of the Transfer Function $G_P(s)$

$$a_5 = T^2 \tag{B.1}$$

$$a_4 = 2T + TK_{qv}K_{p-q} \tag{B.2}$$

$$a_3 = 1 + TK_{qv}K_{i-q} + K_{qv}K_{p-q} + TK_{p\delta}K_{p-p} \tag{B.3}$$

$$a_2 = K_{qv}K_{i-q} + K_{p\delta}K_{p-p} + K_{p\delta}K_{p-p}K_{qv}K_{p-q} + TK_{p\delta}K_{i-p} - K_{pv}K_{p-p}K_{q\delta}K_{p-q} \tag{B.4}$$

$$a_1 = K_{p\delta}K_{p-p}K_{qv}K_{i-q} + K_{p\delta}K_{i-p} + K_{p\delta}K_{i-p}K_{qv}K_{p-q} - K_{pv}K_{p-p}K_{q\delta}K_{i-q} - K_{pv}K_{i-p}K_{q\delta}K_{p-q} \tag{B.5}$$

$$a_0 = K_{p\delta}K_{i-p}K_{qv}K_{i-q} - K_{pv}K_{i-p}K_{q\delta}K_{i-q} \tag{B.6}$$

$$\tag{B.7}$$

$$b_4 = T^2K_{p-p}K_{p\delta} \tag{B.8}$$

$$b_3 = 2TK_{p-p}K_{p\delta} - TK_{p-p}K_{pv}K_{q\delta}K_{p-q} + K_{i-p}K_{p\delta}T^2 + TK_{p-p}K_{p\delta}K_{qv}K_{p-q} \tag{B.9}$$

$$b_2 = TK_{p-p}K_{p\delta}K_{qv}K_{i-q} - TK_{p-p}K_{pv}K_{q\delta}K_{i-q} + 2TK_{i-p}K_{p\delta} - TK_{i-p}K_{pv}K_{q\delta}K_{p-q} + K_{p-p}K_{p\delta} + K_{p-p}K_{p\delta}K_{qv}K_{p-q} - K_{p-p}K_{pv}K_{q\delta}K_{p-q} + TK_{i-p}K_{p\delta}K_{qv}K_{p-q} \tag{B.10}$$

$$b_1 = TK_{i-p}K_{p\delta}K_{qv}K_{i-q} - TK_{i-p}K_{pv}K_{q\delta}K_{i-q} + K_{p-q}K_{p\delta}K_{qv}K_{i-q} - K_{p-p}K_{pv}K_{q\delta}K_{i-q} + K_{i-p}K_{p\delta} + K_{i-p}K_{p\delta}K_{qv}K_{p-q} - K_{i-p}K_{pv}K_{q\delta}K_{p-q} \tag{B.11}$$

$$b_0 = -K_{i-p}K_{pv}K_{q\delta}K_{i-q} + K_{i-p}K_{p\delta}K_{qv}K_{i-q} \tag{B.12}$$

B.2 Parameters of the Characteristic Equation of the DC-link Voltage Control Loop

$$\bar{a}_7 = C_{dc}V_{dc-ref}a_5 \quad (\text{B.13})$$

$$\bar{a}_6 = C_{dc}V_{dc-ref}a_4 \quad (\text{B.14})$$

$$\bar{a}_5 = C_{dc}V_{dc-ref}a_3 - K_{pdc}b_4 \quad (\text{B.15})$$

$$\bar{a}_4 = C_{dc}V_{dc-ref}a_2 - K_{pdc}b_3 - K_{idc}b_4 \quad (\text{B.16})$$

$$\bar{a}_3 = C_{dc}V_{dc-ref}a_1 - K_{pdc}b_2 - K_{idc}b_3 \quad (\text{B.17})$$

$$\bar{a}_2 = C_{dc}V_{dc-ref}a_0 - K_{pdc}b_1 - K_{idc}b_2 \quad (\text{B.18})$$

$$\bar{a}_1 = -K_{pdc}b_0 - K_{idc}b_1 \quad (\text{B.19})$$

$$\bar{a}_0 = -K_{idc}b_0 \quad (\text{B.20})$$

where a_5 to a_0 , and b_4 to b_0 are defined in Section B.1, and K_{pdc} and K_{idc} are the proportional and integral gains of the controller PI_{dc} , respectively.

Curriculum Vitae

Name: Hisham Mahmood

Post-Secondary Education and Degrees: University of Western Ontario
London, ON
2014 Ph.D. in Electrical Engineering

Lakehead University
Thunder Bay, ON
2008 M.E.Sc. in Control Engineering

University of Basrah
Basrah, Iraq
1998 B.Sc. in Electrical Engineering

Related Work Experience:

Teaching Assistant at University of Western Ontario (2008-2012)

Teaching Assistant at Lakehead University (2006-2008)

Department Chair and Lecturer (2003-2005)
Department of Electrical Engineering
HIGH INSTITUTE OF TECHNOLOGY – Libya

Lecturer (2001-2002)
Department of Electrical Engineering
HIGH INSTITUTE OF TECHNOLOGY – Libya

Lecturer (part time)(2001-2003)
Department of Electrical Engineering
GREAT MARCH UNIVERSITY – Libya

Publications:**IEEE Journals**

- [1] **Hisham Mahmood**, D. Michaelson, J. Jiang, "Accurate reactive power sharing in an islanded microgrid using adaptive virtual impedances," *IEEE Transactions on Power Electronics*, vol. 30, no. 3, pp. 1605–1617, Mar. 2015.
- [2] **Hisham Mahmood**, D. Michaelson, J. Jiang, "A power management strategy for PV/battery hybrid systems in islanded microgrids," *IEEE Journal of Emerging and Selected Topics in Power Electronics*, vol. 2, no. 4, pp. 870–882, Dec. 2014.
- [3] **Hisham Mahmood**, J. Jiang, "Modeling and control system design of a grid connected VSC considering the effect of the interface transformer type," *IEEE Transactions on Smart Grid*, vol. 3, no. 1, pp. 122–134, Mar. 2012.
- [4] **Hisham Mahmood**, D. Michaelson, J. Jiang, "Reactive power sharing in islanded microgrids using adaptive voltage droop control," *IEEE Transactions on Smart Grid*, Passed the first review round, 2014
- [5] **Hisham Mahmood**, D. Michaelson, J. Jiang, "Decentralized Power Management of a PV/Battery Hybrid Unit in a Droop Controlled Islanded Microgrid," *IEEE Transactions on Power Electronics*, Submitted Sept. 2014, Preliminary Decision: Recommend publication with minor revisions.
- [6] **Hisham Mahmood**, D. Michaelson, J. Jiang, "Strategies for Independent Deployment and Autonomous Control of PV and Battery Units in Islanded Microgrids," *IEEE Journal of Emerging and Selected Topics in Power Electronics*, Under review, 2014.

Referred Conferences

- [1] **Hisham Mahmood** , J. Jiang, "A control strategy of a distributed generation unit for seamless transfer between grid connected and islanded modes," in *Proc. IEEE International Symp. Ind. Electron. (ISIE)*, June. 2014, pp. 2518–2523.
- [2] D. Michaelson, **Hisham Mahmood**, J. Jiang, "A predictive energy management strategy with pre-emptive load shedding for an islanded PV-battery microgrid," in *Proc. IEEE Ind. Electron. Conf.*, Nov. 2013, pp. 1501–1506.
- [3] **Hisham Mahmood** , D. Michaelson, J. Jiang, "Control strategy for a standalone PV/battery hybrid system," in *Proc. IEEE Ind. Electron. Conf.*, Oct 2012, pp. 3412–3418.
- [4] **Hisham Mahmood** , K. Natarajan, "Parasitics and voltage collapse of the DC-DC boost converter," in *Proc. of IEEE Canadian Conference on Electrical and Computer Engineering*, May. 2008, pp. 273–278.